



This is a repository copy of *Measurement of the production of a W boson in association with a charmed hadron in pp collisions at $\sqrt{s}=13$ TeV with the ATLAS detector.*

White Rose Research Online URL for this paper:

<https://eprints.whiterose.ac.uk/205893/>

Version: Published Version

Article:

Aad, G. orcid.org/0000-0002-6665-4934, Abbott, B. orcid.org/0000-0002-5888-2734, Abeling, K. orcid.org/0000-0002-1002-1652 et al. (2896 more authors) (2023)

Measurement of the production of a W boson in association with a charmed hadron in pp collisions at $\sqrt{s}=13$ TeV with the ATLAS detector. *Physical Review D*, 108. 032012. ISSN 2470-0010

<https://doi.org/10.1103/physrevd.108.032012>

Reuse

This article is distributed under the terms of the Creative Commons Attribution (CC BY) licence. This licence allows you to distribute, remix, tweak, and build upon the work, even commercially, as long as you credit the authors for the original work. More information and the full terms of the licence here:

<https://creativecommons.org/licenses/>

Takedown


If you consider content in White Rose Research Online to be in breach of UK law, please notify us by emailing eprints@whiterose.ac.uk including the URL of the record and the reason for the withdrawal request.



eprints@whiterose.ac.uk
<https://eprints.whiterose.ac.uk/>

Measurement of the production of a W boson in association with a charmed hadron in pp collisions at $\sqrt{s} = 13$ TeV with the ATLAS detector

G. Aad *et al.**
(ATLAS Collaboration)

 (Received 2 February 2023; accepted 1 May 2023; published 14 August 2023)

The production of a W boson in association with a single charm quark is studied using 140 fb^{-1} of $\sqrt{s} = 13$ TeV proton-proton collision data collected with the ATLAS detector at the Large Hadron Collider. The charm quark is tagged by the presence of a charmed hadron reconstructed with a secondary-vertex fit. The W boson is reconstructed from the decay to either an electron or a muon and the missing transverse momentum present in the event. The charmed mesons reconstructed are $D^+ \rightarrow K^- \pi^+ \pi^+$ and $D^{*+} \rightarrow D^0 \pi^+ \rightarrow (K^- \pi^+) \pi^+$ and the charge conjugate decays in the fiducial regions where $p_T(e, \mu) > 30$ GeV, $|\eta(e, \mu)| < 2.5$, $p_T(D^{(*)}) > 8$ GeV, and $|\eta(D^{(*)})| < 2.2$. The integrated and normalized differential cross sections as a function of the pseudorapidity of the lepton from the W boson decay, and of the transverse momentum of the charmed hadron, are extracted from the data using a profile likelihood fit. The measured total fiducial cross sections are $\sigma_{\text{fid}}^{\text{OS-SS}}(W^- + D^+) = 50.2 \pm 0.2(\text{stat})_{-2.3}^{+2.4}(\text{syst})$ pb, $\sigma_{\text{fid}}^{\text{OS-SS}}(W^+ + D^-) = 48.5 \pm 0.2(\text{stat})_{-2.2}^{+2.3}(\text{syst})$ pb, $\sigma_{\text{fid}}^{\text{OS-SS}}(W^- + D^{*+}) = 51.1 \pm 0.4(\text{stat})_{-1.8}^{+1.9}(\text{syst})$ pb, and $\sigma_{\text{fid}}^{\text{OS-SS}}(W^+ + D^{*-}) = 50.0 \pm 0.4(\text{stat})_{-1.8}^{+1.9}(\text{syst})$ pb. Results are compared with the predictions of next-to-leading-order quantum chromodynamics calculations performed using state-of-the-art parton distribution functions. Additionally, the ratio of charm to anticharm production cross sections is studied to probe the s - \bar{s} quark asymmetry. The ratio is found to be $R_c^\pm = 0.971 \pm 0.006(\text{stat}) \pm 0.011(\text{syst})$. The ratio and cross-section measurements are consistent with the predictions obtained with parton distribution function sets that have a symmetric s - \bar{s} sea, indicating that any s - \bar{s} asymmetry in the Bjorken- x region relevant for this measurement is small.

DOI: [10.1103/PhysRevD.108.032012](https://doi.org/10.1103/PhysRevD.108.032012)

I. INTRODUCTION

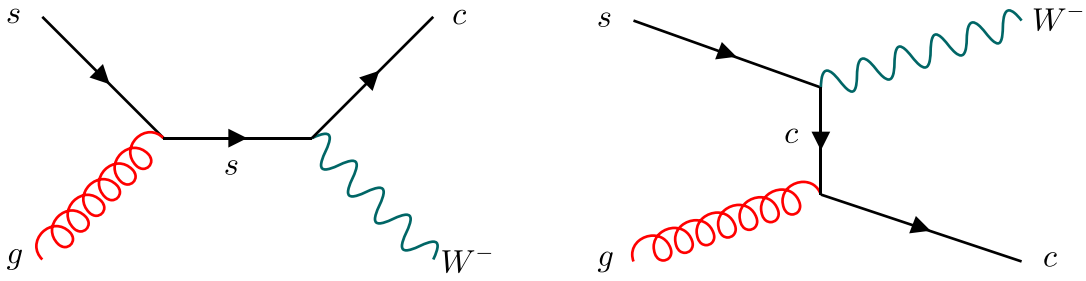
Parton distribution functions (PDFs) describe the momentum distributions of quarks and gluons inside nucleons. Currently, only limited information is available about the PDF of strange quarks in the proton. The sea distributions for the three light quarks, up, down, and strange, might be equal due to flavor SU(3) symmetry; alternatively the strange quark distribution might be suppressed due to its larger mass. Current knowledge of the strange PDF comes largely from measurements of deep-inelastic lepton-proton scattering [1,2] and charged-current neutrino scattering [3–7], and from vector-boson measurements at the Large Hadron Collider (LHC) [8–11]. However, constraints on the strange quark and antiquark PDFs are much weaker than those on the up and down sea quarks and antiquarks [12].

In perturbative quantum chromodynamics (QCD), the production of a W boson in association with a single charm quark occurs through the scattering of a gluon and a down-type quark, i.e. down, strange, or bottom, at leading order (LO), as shown in Fig. 1. The relative contributions to the cross section of $W + c$ production from each of the three different quarks depends on their PDFs and on the values of the three relevant terms from the Cabibbo-Kobayashi-Maskawa (CKM) mixing matrix [13,14]: V_{cd} , V_{cs} , and V_{cb} . At the LHC, the process $gs \rightarrow W^- c$ and its charge conjugate are dominant, while the process $gd \rightarrow W^- c$ ($g\bar{d} \rightarrow W^+ \bar{c}$) contributes only $\sim 10\%$ ($\sim 5\%$) to the $W^- c$ ($W^+ \bar{c}$) rate. The difference between the d and \bar{d} contributions can be attributed to the presence of valence d -quarks [15]. The contribution from b -quark-initiated processes is negligible. The largest next-to-leading-order (NLO) contributions are the one-gluon-loop corrections to $gs \rightarrow W^- c$ ($gs \rightarrow W^+ \bar{c}$); however, various other partonic initial states such as qq' , gg , and sq or $\bar{s}q$ are also present.

The idea of using $W + c$ events to measure the strange PDF was first proposed in Refs. [16,17] and their production was first observed at the Tevatron [18]. At the LHC, it has been measured both by ATLAS and CMS using data

*Full author list given at the end of the article.

Published by the American Physical Society under the terms of the [Creative Commons Attribution 4.0 International license](https://creativecommons.org/licenses/by/4.0/). Further distribution of this work must maintain attribution to the author(s) and the published article's title, journal citation, and DOI. Funded by SCOAP³.

FIG. 1. The leading-order diagrams for $W^- + c$ production.

taken at $\sqrt{s} = 7$ TeV [19–21] and by CMS using data taken at $\sqrt{s} = 8$ and 13 TeV [22,23]. Measurements of $W + c$ production in the forward region at $\sqrt{s} = 7$ and 8 TeV have also been performed by the LHCb Collaboration [24]. In these measurements, the charm quark or antiquark is tagged either by the presence of a jet of particles containing a secondary vertex or a semileptonic decay to a muon, or by explicit reconstruction of a D^+ or D^{*+} meson or its charge conjugate, collectively written as $D^{(*)}$.

This paper presents a measurement of W boson production in association with a $D^{(*)}$ meson using 140 fb^{-1} of $\sqrt{s} = 13$ TeV proton-proton (pp) collision data recorded by the ATLAS detector at the LHC. Events in which the W boson decays to an electron or a muon (and the associated neutrino) are studied and the presence of the charm quark is detected through explicit charmed hadron reconstruction. The measurement does not require the presence of a reconstructed jet. The production of charmed hadrons is studied using the following decay modes (and their charge conjugates):

- (i) $D^+ \rightarrow K^- \pi^+ \pi^+$ and
- (ii) $D^{*+} \rightarrow D^0 \pi^+ \rightarrow (K^- \pi^+) \pi^+$.

The signal $W + D^{(*)}$ events are extracted through a profile likelihood [25] fit to the reconstructed secondary-vertex mass distribution for the D^+ and the mass difference $m(D^{*+} - D^0)$ for the D^{*+} . The main backgrounds are single- W -boson events that do not contain the requisite $D^{(*)}$ decays and $t\bar{t}$ events.

In $W + c$ production, at LO the W boson and charm quark always have opposite-sign electric charges, i.e., either $W^+ + \bar{c}$ or $W^- + c$. For those processes where one of the initial-state partons is a strange or antistrange quark, this charge correlation remains at NLO and next-to-next-to-leading order (NNLO) [15].¹ However, many of the backgrounds (e.g. heavy-flavor pair production or b -hadron production from $t\bar{t}$ events) have equal rates for the production of leptons and $D^{(*)}$ with opposite-sign (OS)

or same-sign (SS) charges. This is exploited in the analysis by extracting the signal as the difference of the numbers of OS and SS candidates denoted by OS–SS, and extrapolating the background estimate from SS candidates. The $t\bar{t}$ background with events containing $W \rightarrow cs$ decays is not charge symmetric and is measured *in situ* by categorizing the events according to whether b -tagged jets separated in phase space from the $D^{(*)}$ candidate are present.

The $W + D^{(*)}$ cross sections, $\sigma_{\text{fid}}^{\text{OS-SS}}(W + D^{(*)})$, are measured in a fiducial region defined by requirements for W boson and $D^{(*)}$ meson selection. The requirements for W boson selection are a charged lepton, ℓ (e or μ), of transverse momentum $p_{\text{T}}^{\ell} > 30$ GeV and pseudorapidity $|\eta^{\ell}| < 2.5$. The requirements for $D^{(*)}$ meson selection are $p_{\text{T}}(D^{(*)}) > 8$ GeV and $|\eta(D^{(*)})| < 2.2$. The total fiducial cross section is presented along with two differential cross sections, in $p_{\text{T}}(D^{(*)})$ and $|\eta(\ell)|$. The measurements are performed separately for events with positively and negatively charged W bosons and the ratio $R_c^{\pm} \equiv \sigma_{\text{fid}}^{\text{OS-SS}}(W^+ + D^-) / \sigma_{\text{fid}}^{\text{OS-SS}}(W^- + D^+)$ is also presented. These measurements are compared with QCD predictions obtained using state-of-the-art PDF sets [9,12,26–31].

An important development in the theoretical study of $W + c$ production is the recent publication of the first NNLO calculation [32] of the process. This calculation includes an off-shell treatment of the W boson and is performed in a five-flavor scheme using the infrared- and collinear-safe flavored k_t algorithm [33] and neglecting c -quark finite-mass effects. Nondiagonal CKM matrix elements and the dominant NLO electroweak (EW) corrections are included. Scale uncertainties obtained using this calculation are below 2%, significantly smaller than PDF uncertainties for most PDF set choices. Such NNLO calculations will ultimately allow the incorporation of $W + c$ measurements into NNLO PDF fits. For $W + c$ -jet measurements, comparisons with NNLO predictions require that cross sections be unfolded to jet observables calculated in the flavored k_t scheme; such unfolded results are not currently available. Alternatively, in the case of $W + D^{(*)}$ measurements, the charm fragmentation function could in the future be incorporated into theory predictions using methods pioneered in Ref. [34].

¹If there is a significant asymmetry between the charm and anticharm PDFs, there would be a contribution from processes with charm quarks in the initial state, i.e. $dc \rightarrow W^- uc$ and $d\bar{c} \rightarrow W^- u\bar{c}$, but this is expected to be small [15].

The measurements presented here are compared with QCD calculations with NLO plus parton-shower accuracy. The baseline framework for these calculations and the QCD scale uncertainties associated with them is MadGraph5_aMC@NLO [35]. Theoretical uncertainties associated with the choice of matching scheme are assessed using the difference between predictions obtained with MadGraph5_aMC@NLO and those obtained with recent calculations [36] implemented in the PowheL event generator [37].

This paper is structured as follows. Section II introduces the ATLAS detector. The data and Monte Carlo simulation samples used in the analysis are discussed in Sec. III. Section IV describes the physics objects used in the analysis and their selection criteria. The reconstruction and selection of charmed mesons are discussed in Sec. V. The event selection is summarized in Sec. VI. Signal and background modeling are described in Sec. VII. Section VIII presents the method used to extract the $W + D^{(*)}$ differential cross section and Sec. IX summarizes the relevant systematic uncertainties. The cross-section measurements and their comparison with theoretical predictions are presented in Sec. X. Conclusions are provided in Sec. XI.

II. THE ATLAS DETECTOR

The ATLAS detector [38] at the LHC covers nearly the entire solid angle around the collision point.² It consists of an inner tracking detector surrounded by a thin superconducting solenoid, electromagnetic and hadron calorimeters, and a muon spectrometer incorporating three large superconducting air-core toroidal magnets.

The inner-detector system (ID) is immersed in a 2 T axial magnetic field and provides charged-particle tracking in the range $|\eta| < 2.5$. The high-granularity silicon pixel detector covers the vertex region and typically provides four measurements per track, the first hit normally being in the insertable B-layer (IBL) installed before Run 2 [39,40]. It is followed by the silicon microstrip tracker, which usually provides eight measurements per track. These silicon detectors are complemented by the transition radiation tracker (TRT), which enables radially extended track reconstruction up to $|\eta| = 2.0$. The TRT also provides electron identification information based on the fraction of hits (typically 30 in total) above a higher energy-deposit threshold corresponding to transition radiation.

²ATLAS uses a right-handed coordinate system with its origin at the nominal interaction point (IP) in the center of the detector and the z -axis along the beam pipe. The x -axis points from the IP to the center of the LHC ring, and the y -axis points upward. Cylindrical coordinates (r, ϕ) are used in the transverse plane, ϕ being the azimuthal angle around the z -axis. The pseudorapidity is defined in terms of the polar angle θ as $\eta = -\ln \tan(\theta/2)$. Angular distance is measured in units of $\Delta R \equiv \sqrt{(\Delta\eta)^2 + (\Delta\phi)^2}$.

The calorimeter system covers the pseudorapidity range $|\eta| < 4.9$. Within the region $|\eta| < 3.2$, electromagnetic calorimetry is provided by barrel and end cap high-granularity lead/liquid-argon (LAr) calorimeters, with an additional thin LAr presampler covering $|\eta| < 1.8$ to correct for energy loss in material upstream of the calorimeters. Hadron calorimetry is provided by the steel/scintillator-tile calorimeter, segmented into three barrel structures within $|\eta| < 1.7$, and two copper/LAr hadron end cap calorimeters. The solid angle coverage is completed with forward copper/LAr and tungsten/LAr calorimeter modules optimized for electromagnetic and hadronic energy measurements, respectively.

The muon spectrometer (MS) comprises separate trigger and high-precision tracking chambers measuring the deflection of muons in a magnetic field generated by the superconducting air-core toroidal magnets. The field integral of the toroids ranges between 2.0 and 6.0 T m across most of the detector. Three layers of precision chambers cover the region $|\eta| < 2.7$. They consist of layers of monitored drift tubes, complemented by cathode-strip chambers in the forward region, where the background is highest. The muon trigger system covers the range $|\eta| < 2.4$ with resistive-plate chambers in the barrel, and thin-gap chambers in the end cap regions.

Interesting events are selected by the first-level trigger system implemented in custom hardware, followed by selections made by algorithms implemented in software in the high-level trigger [41]. The first-level trigger accepts events from the 40 MHz bunch crossings at a rate below 100 kHz, which the high-level trigger further reduces in order to record events to disk at about 1 kHz.

An extensive software suite [42] is used in data simulation, in the reconstruction and analysis of real and simulated data, in detector operations, and in the trigger and data acquisition systems of the experiment.

III. DATA AND MONTE CARLO SAMPLES

A. Dataset description

Events are selected from $\sqrt{s} = 13$ TeV pp collision data collected by ATLAS in the period between 2015 and 2018 (Run 2 of the LHC). After data quality requirements [43] are applied to ensure that all detector components are in good working condition, the dataset amounts to an integrated luminosity of 140 fb^{-1} . The uncertainty in the combined 2015–2018 integrated luminosity is 0.83% [44] obtained using the LUCID-2 detector [45] for the primary luminosity measurements, complemented by measurements using the inner detector and calorimeters. The absolute luminosity scale was determined using van der Meer scans during dedicated running periods in each year and extrapolated to physics data-taking using complementary measurements from several luminosity-sensitive detectors.

Events were recorded by either single-electron or single-muon triggers. The minimum p_T threshold ranged during data-taking from 24 to 26 GeV for electrons and from 20 to 26 GeV for muons. Triggers with low p_T thresholds, below 60 GeV for electrons and below 50 GeV for muons, include isolation requirements. For electrons, the requirement is $p_T^{\text{iso}}(\Delta R_{\text{var}} < 0.2)/p_T < 0.10$, where $p_T^{\text{iso}}(\Delta R_{\text{var}} < 0.2)$ is the scalar sum of transverse momenta of tracks within a variable-size cone, ΔR_{var} , around the electron. The cone size has a maximum value of 0.2 and decreases as a function of the electron's p_T as $10 \text{ GeV}/p_T[\text{GeV}]$ [46]. The muon isolation criterion is constructed by summing the p_T of ID tracks with $p_T^{\text{tk}} > 1 \text{ GeV}$ around the muon candidate satisfying $\Delta z < 6 \text{ mm}$, with Δz being the distance of the track from the primary vertex in the z -direction. This cut was found to be inefficient in events with high pile-up in 2017 and was tightened to $\Delta z < 2 \text{ mm}$, which allowed the loosening of the isolation criterion for data-taking in 2018. The muon isolation cut is then defined as $p_T^{\text{iso}}(\Delta z)/p_T < 0.07$, where $p_T^{\text{iso}}(\Delta z)$ is the scalar sum of transverse momenta of additional nearby tracks [47]. Triggers with higher p_T thresholds of 60 and 140 GeV for electrons and 50 GeV for muons are added to increase the selection efficiency.

B. Simulated event samples for signal and background modeling

Monte Carlo (MC) simulations are used to model the signal and all backgrounds except multijet. Samples

produced with various MC generators are processed using a full detector simulation [48] based on GEANT4 [49] and then reconstructed using the same algorithms as the data. The effect of multiple interactions in the same and neighboring bunch crossings (pile-up) is modeled by overlaying each simulated hard-scattering event with inelastic pp events generated with PYTHIA 8.186 [50] using the NNPDF2.3LO set of PDFs [51] and a set of tuned parameters called the A3 tune [52]. The MC events are weighted to reproduce the distribution of the average number of interactions per bunch crossing ($\langle \mu \rangle$) observed in the data, scaled up by a factor of 1.03 ± 0.04 to improve agreement between data and simulation in the visible inelastic pp cross section [53]. A reweighting procedure is applied to all MC samples to correct the charmed hadron production fractions to the world-average values [54,55]. The change in the individual charmed meson production fractions is as large as 20%, depending on the MC configuration. An overview of all signal and background processes and the generators used to model them is given in Table I, and further information about the relevant generators configurations is provided below. Processes with more than one jet, known as multileg processes, can have different numbers of jets in each event. To improve the accuracy of calculations, samples with different jet multiplicities are often merged. In such multileg samples, the QCD accuracy for each jet multiplicity is specified in the table.

TABLE I. The generator configurations used to simulate the signal and background processes. The acronyms ME, PS, and UE stand for matrix element, parton shower, and underlying event, respectively. The column ‘‘HF decay’’ specifies which software package is used to model the heavy-flavor decays of bottom and charmed hadrons. For multileg samples where different jet multiplicities are merged, the QCD accuracy for each jet multiplicity is specified.

Process	ME generator	QCD accuracy	ME PDF	PS generator	UE tune	HF decay
<i>W</i> + jets (background modeling)						
<i>W</i> + jets	Sherpa 2.2.11	0–2j@NLO + 3–5j@LO	NNPDF3.0NNLO	Sherpa	Default	Sherpa
<i>W</i> + jets	aMC@NLO (CKKW-L)	0–4j@LO	NNPDF3.0NLO	PYTHIA 8	A14	EvtGen
<i>W</i> + jets	aMC@NLO (FxFx)	0–3j@NLO	NNPDF3.1NNLO_LUXQED	PYTHIA 8	A14	EvtGen
<i>W</i> + <i>D</i> ^(*) (signal modeling and theory predictions)						
<i>W</i> + <i>D</i> ^(*)	Sherpa 2.2.11	0–1j@NLO + 2j@LO	NNPDF3.0NNLO	Sherpa	Default	EvtGen
<i>W</i> + <i>D</i> ^(*)	aMC@NLO (NLO)	NLO	NNPDF3.0NNLO	PYTHIA 8	A14	EvtGen
<i>W</i> + <i>D</i> ^(*)	aMC@NLO (FxFx)	0–3j@NLO	NNPDF3.1NNLO_LUXQED	PYTHIA 8	A14	EvtGen
Backgrounds						
<i>Z</i> + jets	Sherpa 2.2.11	0–2j@NLO + 3–5j@LO	NNPDF3.0NNLO	Sherpa	Default	Sherpa
<i>t</i> \bar{t}	POWHEG BOX v2	NLO	NNPDF3.0NLO	PYTHIA 8	A14	EvtGen
Single- <i>t</i> , <i>Wt</i>	POWHEG BOX v2	NLO	NNPDF3.0NLO	PYTHIA 8	A14	EvtGen
Single- <i>t</i> , <i>t</i> -channel	POWHEG BOX v2	NLO	NNPDF3.0NLO	PYTHIA 8	A14	EvtGen
Single- <i>t</i> , <i>s</i> -channel	POWHEG BOX v2	NLO	NNPDF3.0NLO	PYTHIA 8	A14	EvtGen
<i>t</i> $\bar{t}V$	aMC@NLO	NLO	NNPDF3.0NLO	PYTHIA 8	A14	EvtGen
Diboson fully leptonic	Sherpa 2.2.2	0–1j@NLO + 2–3j@LO	NNPDF3.0NNLO	Sherpa	Default	Sherpa
Diboson hadronic	Sherpa 2.2.1	0–1j@NLO + 2–3j@LO	NNPDF3.0NNLO	Sherpa	Default	Sherpa

1. Background $V + \text{jets}$ samples

Three generator configurations are used to model inclusive vector boson (W or Z) plus jet production. These samples are used to estimate the $W + D^{(*)}$ backgrounds and the corresponding experimental and theory systematic uncertainties.

Sherpa: The nominal MC generator used for this analysis is Sherpa 2.2.11 [56]. NLO-accurate matrix elements (ME) for up to two partons, and LO-accurate matrix elements for between three and five partons, are calculated in the five-flavor scheme using the COMIX [57] and OpenLoops [58–60] libraries. The b - and c -quarks are treated as massless at matrix-element level and massive in the parton shower. The Hessian $\text{NNPDF3.0}_{\text{NNLO}}$ PDF set [61] is used. The default Sherpa parton shower [62] based on Catani-Seymour dipole factorization and the cluster hadronization model [63] is used. The samples are generated using a dedicated set of tuned parameters developed by the Sherpa authors and use the $\text{NNPDF3.0}_{\text{NNLO}}$ set. The NLO matrix elements for a given jet multiplicity are matched to the parton shower (PS) using a color-exact variant of the MC@NLO algorithm [64]. Different jet multiplicities are then merged into an inclusive sample using an improved CKKW matching procedure [65,66] which is extended to NLO accuracy using the MEPS@NLO prescription [67]. The merging scale Q_{cut} is set to 20 GeV.

Uncertainties from missing higher orders in Sherpa samples are evaluated [68] using seven variations of the QCD renormalization (μ_r) and factorization (μ_f) scales in the matrix elements by factors of 0.5 and 2, avoiding variations in opposite directions. The strong coupling constant α_s is varied by ± 0.001 to assess the effect of its uncertainty. Additional details of the use of these samples are available in Ref. [69].

MadGraph5_aMC@NLO (CKKW-L): $V + \text{jets}$ production is simulated with LO-accurate matrix elements for up to four partons with MadGraph5_aMC@NLO 2.2.2 [35]. The matrix-element calculation is interfaced with PYTHIA 8.186 for the modeling of the parton shower, hadronization, and underlying event. To remove overlap between the matrix element and the parton shower, the CKKW-L merging procedure [70,71] is applied with a merging scale of $Q_{\text{cut}} = 30$ GeV and a jet-clustering radius parameter of 0.2. In order to better model the region of large jet p_T , the strong coupling α_s is evaluated at the scale of each splitting to determine the weight. The matrix-element calculation is performed with the $\text{NNPDF3.0}_{\text{NNLO}}$ PDF set [61] with $\alpha_s = 0.118$. The calculation is done in the five-flavor scheme with massless b - and c -quarks. Cross sections are calculated using a diagonal CKM matrix. Heavy-quark masses are reinstated in the PYTHIA 8 shower. The values of μ_r and μ_f are set to one half of the transverse mass of all final-state partons and leptons. The A14 tune [72] of PYTHIA 8 is used with the $\text{NNPDF2.3}_{\text{LO}}$ PDF set with $\alpha_s = 0.13$. The decays of bottom and charmed hadrons are performed by EvtGen 1.7.0 [73].

MadGraph5_aMC@NLO (FxFx): The MadGraph5_aMC@NLO 2.6.5 program [35] is used to generate weak bosons with up to three additional partons in the final state at NLO accuracy. The scales μ_r and μ_f are set to one half of the transverse mass of all final-state partons and leptons. Cross sections are calculated using a diagonal CKM matrix. The showering and subsequent hadronization are performed using PYTHIA 8.240 with the A14 tune and the $\text{NNPDF2.3}_{\text{LO}}$ PDF set with $\alpha_s = 0.13$. The different jet multiplicities are merged using the FxFx NLO matrix-element and parton-shower merging prescription [74]. PYTHIA 8.186 is used to model the parton shower, hadronization, and underlying event.

The calculation uses a five-flavor scheme with massless b - and c -quarks at the matrix-element level, and massive quarks in the PYTHIA 8 shower. At the event-generation level, the jet transverse momentum is required to be at least 10 GeV, with no restriction on the absolute value of the jet pseudorapidity. The PDF set used for event generation is $\text{NNPDF3.1}_{\text{NNLO_LUXQED}}$. The merging scale is set to $Q_{\text{cut}} = 20$ GeV. Scale variations where μ_r and μ_f are varied independently by a factor of 2 or 0.5 in the matrix element are included as generator event weights. The decays of bottom and charmed hadrons are performed by EvtGen 1.7.0.

2. Signal $W + D^{(*)}$ signal samples

Only about 2% of the events in the inclusive $W + \text{jets}$ samples pass the $W + D^{(*)}$ fiducial requirements. This, coupled with the branching ratios of 9.2% (2.5%) to the D^+ (D^{*+}) decay mode of interest, means that even very large $W + \text{jets}$ samples provide statistically inadequate measurements of the $W + D^{(*)}$ fiducial efficiency. Filtered signal samples are therefore used to enhance the statistical precision. The generated events are filtered to require the presence of a single lepton with $p_T > 15$ GeV and $|\eta| < 2.7$ and either a D^{*+} or a D^+ meson with $p_T > 7$ GeV and $|\eta| < 2.3$. EvtGen 1.7.0 is used to force all D^0 mesons to decay through the mode $D^0 \rightarrow K^- \pi^+$ and all D^+ mesons to decay through the mode $D^+ \rightarrow K^- \pi^+ \pi^+$ (plus charge conjugates). EvtGen describes this three-body D^+ decay using a Dalitz plot amplitude that includes contributions from the $\bar{K}^{*0}(892)$, $\bar{K}^{*0}(1430)$, $\bar{K}^{*0}(1680)$, and $\kappa(800)$ resonances, as measured by CLEO-c [75].

These samples are used for signal modeling, for calculating the detector response matrix and fiducial efficiencies with small statistical uncertainties, and for determining the $W + D^{(*)}$ signal mass distribution used in the statistical analysis described in Sec. VIII. The aMC@NLO+Py8 (NLO) simulation described below is also used to calculate the theory predictions with the up-to-date PDF sets in Sec. X. Three such filtered samples are used.

Sherpa 2.2.11 $W + D^{(*)}$: To reduce the per-event CPU time for the generation of the $W + D^{(*)}$ signal datasets, Sherpa 2.2.11 is configured to have lower perturbative accuracy than

for the inclusive $V + \text{jets}$ samples described above. Events are generated with NLO-accurate matrix elements for up to one jet, and LO-accurate matrix elements for two partons, in the five-flavor scheme. Other Sherpa parameters are set to the same values as for the baseline inclusive samples and uncertainties are evaluated using the same variations in QCD scale and α_s as for the baseline. The production cross section for this configuration differs from that of the inclusive sample by $\sim 2\%$. The two configurations show no significant differences in kinematic distributions associated with the $D^{(*)}$ meson or W boson.

`aMC@NLO+Py8 (NLO) $W + D^{(*)}$` : MadGraph5_aMC@NLO 2.9.3 is used to generate the $W + c$ -jet process at NLO accuracy. A finite charm quark mass of $m_c = 1.55$ GeV is used to regularize the cross section, and a full CKM matrix is used to calculate the hard-scattering amplitudes. The values of μ_r and μ_f are set to half of the transverse mass of all final-state partons and leptons. The PDF set used for event generation is NNPDF3.0NNLO with $\alpha_s = 0.118$. The matrix-element calculation is interfaced with PYTHIA 8.244 for the modeling of the parton shower, hadronization, and underlying event and the A14 tune is employed. Scale variations where μ_r and μ_f are varied independently by a factor of 2 or 0.5 in the matrix element are included as generator event weights.

`aMC@NLO+Py8 (FxFx) $W + D^{(*)}$` : Events are generated using the same PYTHIA 8 configuration as used for the inclusive `aMC@NLO+Py8 (FxFx)` sample, but with the event-level filtering and configuration described above.

3. Top-quark pair production background samples

The production of $t\bar{t}$ events is modeled using the POWHEG BOX v2 [76–79] generator which provides matrix elements at NLO in the strong coupling constant α_s with the NNPDF3.0NLO PDF and the h_{damp} parameter³ set to $1.5 m_{\text{top}}$ [80]. The functional form of μ_r and μ_f is set to the default scale $\sqrt{m_{\text{top}}^2 + p_T^2}$ where p_T is the transverse momentum of the top quark obtained using the underlying Born kinematics. Top quarks are decayed at LO using MadSpin [81,82] to preserve all spin correlations. The events are interfaced with PYTHIA 8.230 for the parton shower and hadronization, using the A14 tune and the NNPDF2.3LO PDF set. The decays of bottom and charmed hadrons are simulated using EvtGen 1.6.0.

The NLO $t\bar{t}$ inclusive production cross section is corrected to the theory prediction at NNLO in QCD including the resummation of next-to-next-to-leading-logarithmic (NNLL) soft-gluon terms calculated using Top++ 2.0 [83–89].

POWHEG+Herwig 7.04 and MadGraph5_aMC@NLO+PYTHIA 8 $8t\bar{t}$ samples are used to estimate the systematic uncertainty

³The h_{damp} parameter controls the transverse momentum p_T of the first additional emission beyond the leading-order Feynman diagram in the parton shower and therefore regulates the high- p_T emission against which the $t\bar{t}$ system recoils.

due to the choice of MC model as explained in the following and the details of the configurations used are provided below.

$t\bar{t}$ POWHEG+Herwig 7.04: The impact of using a different parton-shower and hadronization model is evaluated by comparing the nominal $t\bar{t}$ sample with another event sample produced with the POWHEG BOX v2 generator using the NNPDF3.0NLO parton distribution function. Events in the latter sample are interfaced with Herwig 7.04 [90,91], using the H7UE set of tuned parameters [91] and the MMHT2014LO PDF set [92]. The decays of bottom and charmed hadrons are simulated using EvtGen 1.6.0 [73].

$t\bar{t}$ MadGraph5_aMC@NLO+PYTHIA 8: The uncertainty in the matching of NLO matrix elements to the parton shower is assessed by comparing the POWHEG sample with events generated with MadGraph5_aMC@NLO 2.6.0 interfaced with PYTHIA 8.230. The MadGraph5_aMC@NLO calculation used the NNPDF3.0NLO set of PDFs and PYTHIA 8 used the A14 tune and the NNPDF2.3LO set of PDFs. The decays of bottom and charmed hadrons are simulated using EvtGen 1.6.0.

4. Wt -channel single-top background samples

Single-top Wt associated production is modeled using the POWHEG BOX v2 generator which provides matrix elements at NLO in the strong coupling constant α_s in the five-flavor scheme with the NNPDF3.0NLO parton distribution function set. The functional form of μ_r and μ_f is set to the default scale $\sqrt{m_{\text{top}}^2 + p_T^2}$. The diagram removal scheme [93] is employed to handle the interference with $t\bar{t}$ production [80]. Top quarks are decayed at LO using MadSpin to preserve all spin correlations. The events are interfaced with PYTHIA 8.230 using the A14 tune and the NNPDF2.3LO PDF set. The decays of bottom and charmed hadrons are simulated using EvtGen 1.6.0. The inclusive cross section is corrected to the theory prediction calculated at NLO in QCD with NNLL soft gluon corrections [94,95].

5. t -channel and s -channel single-top background samples

Single-top t -channel (s -channel) production is modeled using the POWHEG BOX v2 generator at NLO in QCD using the four-flavor (five-flavor) scheme and the corresponding NNPDF3.0NLO set of PDFs. The events are interfaced with PYTHIA 8.230 using the A14 tune and the NNPDF2.3LO set of PDFs.

The uncertainty due to initial-state radiation (ISR) is estimated by simultaneously varying the h_{damp} parameter and μ_r and μ_f , and choosing the Var3c up and down variants of the A14 tune as described in Ref. [96]. The impact of final-state radiation is evaluated by halving and doubling the renormalization scale for emissions from the parton shower.

6. $t\bar{t} + V$ background samples

The production of $t\bar{t}V$ events, where V denotes either W , Z , or e^+e^- produced through Z/γ interference, is modeled using the MadGraph5_aMC@NLO 2.3.3 [35] generator at NLO with the NNPDF3.0NLO parton distribution function. The events are interfaced with PYTHIA 8.210 using the A14 tune and the NNPDF2.3LO PDF set. The uncertainty due to ISR is estimated by comparing the nominal $t\bar{t}V$ sample with two additional samples, which have the same settings as the nominal one, but with the var3 up or down variation of the A14 tune.

7. Diboson background samples

Samples of diboson final states (VV) are simulated with the Sherpa 2.2.1 or 2.2.2 [56] generator depending on the process (see Table I), including off-shell effects and Higgs boson contributions, where appropriate. Fully leptonic final states and semileptonic final states, where one boson decays leptonically and the other hadronically, are generated using matrix elements at NLO accuracy in QCD for up to one additional parton and at LO accuracy for up to three additional parton emissions. Samples for the gluon-loop-induced processes $gg \rightarrow VV$ are generated using LO-accurate matrix elements for up to one additional parton emission for both the cases of fully leptonic and semileptonic final states. The matrix-element calculations are matched and merged with the Sherpa parton shower based on Catani-Seymour dipole factorization using the MEPS@NLO prescription. The virtual QCD corrections are provided by the OpenLoops library. The NNPDF3.0NLO set of PDFs is used along with the dedicated set of tuned parton-shower parameters developed by the Sherpa authors.

Matrix element to parton-shower matching [64] is employed for different jet multiplicities, which are then merged into an inclusive sample using an improved CKKW matching procedure which is extended to NLO accuracy using the MEPS@NLO prescription. These simulations are NLO accurate for up to one additional parton and LO accurate for up to three additional partons. The virtual QCD correction for matrix elements at NLO accuracy is provided by the OpenLoops library. The calculation is performed in the

G_μ scheme [97], ensuring an optimal description of pure electroweak interactions at the electroweak scale.

IV. OBJECT SELECTION

The selection and categorization of $W + D^{(*)}$ candidate events depend on the reconstruction and identification of electrons, muons, tracks, and jets. Proton-proton interaction vertices are reconstructed from charged-particle tracks with $p_T > 500$ MeV in the ID. The presence of at least one such vertex with a minimum of two associated tracks is required, and the vertex with the largest sum of p_T^2 of associated tracks is chosen as the primary vertex (PV).

Three different categories of leptons are used in the analysis: `baseline`, `loose`, and `tight`. Here, “leptons” include electrons and muons, but exclude τ -leptons. `Baseline` leptons are required to have $p_T > 20$ GeV, while `loose` and `tight` leptons are required to have $p_T > 30$ GeV. `Tight` leptons are required to meet isolation requirements. `Antitight` leptons are required to pass the `loose` requirements, but fail the `tight` requirements. They are used in the data-driven multijet production estimation described in Sec. VII C. Full electron and muon selection criteria are given in the text below and summarized in Table II.

Tracks used in the electron and muon reconstruction are required to be associated with the PV, using constraints on the transverse impact-parameter significance ($|d_0^{\text{BL}}/\sigma(d_0^{\text{BL}})|$) and on the longitudinal impact parameter (z_0^{BL}). The transverse impact-parameter significance is calculated with respect to the measured beamline position and must satisfy $|d_0^{\text{BL}}/\sigma(d_0^{\text{BL}})| < 3.0$ for muons and $|d_0^{\text{BL}}/\sigma(d_0^{\text{BL}})| < 5.0$ for electrons. The longitudinal impact parameter of the track is the longitudinal distance along the beamline between the point where $|d_0^{\text{BL}}/\sigma(d_0^{\text{BL}})|$ is measured and the primary vertex. Tracks are required to have $|z_0^{\text{BL}} \sin \theta| < 0.5$ mm, where θ is the polar angle of the track.

Electron candidates are reconstructed from an isolated energy deposit in the electromagnetic calorimeter matched to a track in the ID and must pass the tight likelihood-based working point [98]. Electrons must be in the fiducial pseudorapidity region of $|\eta| < 2.47$, excluding the

TABLE II. Lepton categories used in this analysis.

Features	Electrons			Muons		
	baseline	loose	tight	baseline	loose	tight
p_T	> 20 GeV		> 30 GeV	> 20 GeV		> 30 GeV
$ \Delta z_0^{\text{BL}} \sin(\theta) $		< 0.5 mm			< 0.5 mm	
$ d_0^{\text{BL}}/\sigma(d_0^{\text{BL}}) $		< 5			< 3	
Pseudorapidity	$(\eta < 1.37) \cup (1.52 < \eta < 2.47)$				$ \eta < 2.5$	
Identification		Tight			Tight	
Isolation	No		Yes	No		Yes

transition region $1.37 < |\eta| < 1.52$ between the calorimeter barrel and end caps. The `tight` electrons are required to meet the “tight” isolation criteria [98] based on a combination of the track-based and calorimeter-based isolation. The track-based isolation is $p_T^{\text{iso}}(\Delta R_{\text{var}} < 0.2)/p_T < 0.06$, with a variable cone size as defined in Sec. III A. The tracks are required to have $p_T^{\text{trk}} > 1$ GeV and are required to be associated with the primary vertex. The calorimeter-based isolation is $E_T^{\text{cone20}}/p_T < 0.06$, where E_T^{cone20} is the sum of the transverse energy of positive-energy topological clusters whose barycenter falls within a $\Delta R < 0.2$ cone centered around the electron, corrected for the energy leakage, pile-up, and underlying event, as described in Ref. [98]. Electron energy scale is calibrated following the procedure given in Ref. [98].

Muon candidates are reconstructed in the region $|\eta| < 2.5$ by matching tracks in the MS with those in the ID. The global refitting algorithm [99] is used to combine the information from the ID and MS subdetectors. Muons are identified using the tight quality criteria [100] characterized by the numbers of hits in the ID and MS subsystems. The `tight` muons are required to pass the tight isolation working point, based on a combination of the track-based and particle-flow-based [101] isolation. The requirement is $(p_T^{\text{iso}}(\Delta R_{\text{var}} < 0.3) + 0.4 \times E_T^{\text{neflow20}})/p_T < 0.045$, where the track-based isolation uses a variable cone size as defined in Sec. III A, with a maximum size of $\Delta R = 0.3$. The tracks are required to have $p_T^{\text{trk}} > 500$ MeV and are required to be associated with the primary vertex. The E_T^{neflow20} is the sum of the transverse energy of neutral particle-flow objects in a cone of size $\Delta R < 0.2$ around the muon [100]. Muon momentum calibration is performed using the prescription in Ref. [99].

Jets are reconstructed from particle-flow objects [101] using the anti- k_r [102,103] jet-reconstruction algorithm with a distance parameter $R = 0.4$. Candidate jets are required to have $p_T > 20$ GeV and $|\eta| < 5.0$. The jet energy scale calibration restores the jet energy to that of jets reconstructed at the particle level, as described in Ref. [104]. The jets from pile-up interactions are suppressed using the Jet Vertex Tagger algorithm (JVT) [105].

Jets with $|\eta| < 2.5$ and $p_T > 20$ GeV containing b -hadrons are identified by a deep neural network tagger, DL1r [106–108], that uses displaced tracks, secondary vertices, and decay topologies. The chosen working point has 70% efficiency for identifying b -jets in a simulated $t\bar{t}$ sample and the measured rejection factor (the inverse misidentification efficiency) for c -jets (light jets) is about 11 (600) [108]. The b -jets are defined according to the presence of b -hadrons with $p_T > 5$ GeV within a cone of size $\Delta R = 0.3$ around the jet axis. If a b -hadron is not found and a c -hadron is found, then the jet is labeled a c -jet. Light jets are all the rest.

The missing transverse momentum (E_T^{miss}) in the events is calculated as the negative vector sum of the selected

high- p_T calibrated objects (jets and baseline electrons and muons), plus a “soft term” reconstructed from tracks not associated with any of the calibrated objects [109,110].

To avoid cases where the detector response to a single physical object is reconstructed as two different final-state objects, e.g., an electron reconstructed as both an electron and a jet, an overlap removal strategy is used. If the two calorimeter energy clusters from two electron candidates overlap, the electron with the highest E_T is retained. If a reconstructed electron and muon share the same ID track, the muon is rejected if it is calorimeter tagged, meaning the muon is identified as a reconstructed ID track that extrapolates to the calorimeter energy deposit of a minimum-ionizing particle without a MS signal [100]; otherwise the electron is rejected. Next, jets within $\Delta R = 0.2$ of electrons are removed. In the last step, electrons and muons within $\Delta R = 0.4$ of any remaining jet are removed. This overlap removal procedure is performed using the baseline leptons.

V. CHARMED MESON RECONSTRUCTION

Events containing c -quarks are identified by explicitly reconstructing charmed mesons in charged, hadronic decay channels. Two charmed hadron decay channels are used: $D^+ \rightarrow K^- \pi^+ \pi^+$ and $D^{*+} \rightarrow D^0 \pi \rightarrow (K^- \pi^+) \pi^+$ (and charge conjugates). The invariant mass distribution $m(D^+)$ [mass difference $m(D^{*+} - D^0)$] used in the fit for the D^+ (D^{*+}) channel is described in Sec. VIII.

ID tracks satisfying $|\eta| < 2.5$ and $|z_0 \sin \theta| < 5$ mm are used for $D^{(*)}$ meson reconstruction. The loose track quality requirement is applied [111]. The D^+ (D^0) candidate is reconstructed using ID tracks with $p_T > 800$ MeV (600 MeV). A geometric separation of $\Delta R < 0.6$ among the tracks is required. Tracks corresponding to the baseline leptons used for the W boson candidates are excluded. The D^+ candidates are required to have three tracks with total charge $= \pm 1$. The two tracks with the same charge are assigned the charged pion mass and the remaining track is assigned the kaon mass. The D^0 candidates are required to have two tracks with total charge $= 0$. One track is assigned the charged pion mass and the other is assigned the charged kaon mass. Both possible choices for the mass assignment are retained until matching to the prompt pion from the D^{*+} decay is performed. Tracks from the D^+ (D^0) candidate are fitted to a common secondary vertex (SV), with a fit χ^2 required to be $\chi^2 < 8.0(10.0)$. To reduce the contribution from pile-up and from b -hadron decays, the transverse impact parameter of the $D^{(*)}$ candidate’s flight path with respect to the PV is required to satisfy $|d_0| < 1.0$ mm and the candidate is required to have a 3D impact-parameter significance $\sigma_{3D} < 4.0$, where σ_{3D} is the distance of closest approach of the candidate’s flight path to the PV divided by the uncertainty in that distance. These selection criteria and

those described below were determined by optimizing the OS–SS signal significance, using MC predictions to estimate the signal, and mass sidebands to estimate the background.

Several requirements are placed on the D^+ candidates to reduce combinatorial background. The angle between the kaon track in the rest frame of the D^+ candidate and the line of flight of the D^+ candidate in the center-of-mass frame is required to satisfy $\cos\theta^*(K) > -0.8$. The distance between the SV and the PV in the transverse plane is required to satisfy $L_{xy} > 1.1$ mm for D^+ candidates with $p_T < 40$ GeV and $L_{xy} > 2.5$ mm for D^+ candidates with $p_T > 40$ GeV. Kinematic requirements are applied to ensure orthogonality to other $D^{(*)}$ decays with similar final states. The contamination from $D^{*+} \rightarrow D^0\pi^+ \rightarrow (K^-\pi^+)\pi^+$, which has the same final-state content as the $D^+ \rightarrow K^-\pi^+\pi^+$ channel, is reduced by requiring $m(K\pi\pi) - m(K\pi) > 160$ MeV. Background from the $D_s^\pm \rightarrow \phi\pi^\pm \rightarrow (K^+K^-)\pi^\pm$ channel, with one of the kaons misidentified as a pion, is removed by requiring the mass of each pair of oppositely charged particles, assuming the kaon mass hypothesis, to be $m(K^+K^-) > |m_\phi - 8|$ MeV. The world-average mass of the ϕ meson from the Particle Data Group (PDG) database [112], $m_\phi = 1019.455$ MeV, is used. Finally, a requirement is placed on the invariant mass of the D^+ candidates, 1.7 GeV $< m(D^+) < 2.2$ GeV.

The D^{*+} candidates are reconstructed by combining D^0 candidates with prompt tracks that are assigned the charged pion mass. Only combinations where the pion in the D^0 candidate has the same charge as the prompt pion are considered. The small mass difference between the D^{*+} and D^0 mesons restricts the phase space of this associated prompt pion, which has low momentum in the D^0 rest frame and hence is referred to as the slow pion. Slow pion tracks are required to have $p_T > 500$ MeV and a transverse impact parameter of $|d_0| < 1.0$ mm with respect to the primary vertex. An $L_{xy} > 0$ mm requirement is applied to D^0 candidates. The mass of the D^0 candidate must be within 40 MeV of the PDG world-average value of the D^0 mass, $m_{D^0} = 1864.83$ MeV [112]. Additionally, the angular separation between the slow pion and the D^0 meson must be small, $\Delta R(\pi_{\text{slow}}, D^0) < 0.3$, and the invariant mass cut of 140 MeV $< m(D^{*+} - D^0) < 180$ MeV is imposed.

Combinatorial background from light jets is reduced by requiring $D^{(*)}$ candidates to be isolated. The transverse momenta of tracks in a cone of size $\Delta R = 0.4$ around the $D^{(*)}$ candidate are summed, and the sum is required to be less than the p_T of the $D^{(*)}$. Background from semileptonic B meson decays is reduced by requiring $\Delta R(D^{(*)}, \ell) > 0.3$. Finally, the $D^{(*)}$ candidates are required to have 8 GeV $< p_T < 150$ GeV and $|\eta| < 2.2$. The η cut is applied to avoid the edge of the ID, where the amount of the detector material

TABLE III. $D^{(*)}$ object selection criteria. For D^{*+} candidates the cuts related to SV reconstruction are applied to the corresponding D^0 candidate.

$D^{(*)}$ cut	D^+ cut value	D^{*+} cut value [$D^0\pi \rightarrow (K\pi)\pi$]
N_{tracks} at SV	3	2
SV charge	± 1	0
SV fit quality	$\chi^2 < 8$	$\chi^2 < 10$
Track p_T	$p_T > 800$ MeV	$p_T > 600$ MeV
Track angular separation	$\Delta R < 0.6$	$\Delta R < 0.6$
Flight length	$L_{xy} > 1.1$ mm [$p_T(D^+) < 40$ GeV] $L_{xy} > 2.5$ mm [$p_T(D^+) \geq 40$ GeV]	$L_{xy} > 0$ mm
SV impact parameter	$ d_0 < 1$ mm	$ d_0 < 1$ mm
SV 3D impact significance	$\sigma_{3D} < 4.0$	$\sigma_{3D} < 4.0$
Combinatorial background rejection	$\cos\theta^*(K) > -0.8$...
Isolation	$\Sigma p_{T\text{tracks}}^{\Delta R < 0.4} / p_T(D^+) < 1.0$	$\Sigma p_{T\text{tracks}}^{\Delta R < 0.4} / p_T(D^{*+}) < 1.0$
$D_s^\pm \rightarrow \phi\pi^\pm$ rejection	$m(K^+K^-) > m_\phi - 8 $ MeV	...
D^{*+} background rejection	$m(K\pi\pi) - m(K\pi) > 160$ MeV	...
D^0 mass	...	$ m_{K\pi} - m_{D^0} < 40$ MeV
π_{slow} p_T	...	$p_T > 500$ MeV
π_{slow} angular separation	...	$\Delta R(\pi_{\text{slow}}, D^0) < 0.3$
π_{slow} d_0	...	$ d_0 < 1$ mm
QCD background rejection	$\Delta R(D^+, \ell) > 0.3$	$\Delta R(D^{*+}, \ell) > 0.3$
$D^{(*)}$ p_T	8 GeV $< p_T(D^+) < 150$ GeV	8 GeV $< p_T(D^{*+}) < 150$ GeV
$D^{(*)}$ η	$ \eta(D^+) < 2.2$	$ \eta(D^{*+}) < 2.2$
Invariant mass	1.7 GeV $< m(D^+) < 2.2$ GeV	140 MeV $< m(D^{*+} - D^0) < 180$ MeV

TABLE IV. Tables summarizing the event selection in the analysis: (a) fit regions used in the statistical analysis, (b) the “truth” fiducial selection. The $W + D^{(*)}$ signal is defined by performing the OS–SS subtraction as described in the text.

(a)		
Detector-level selection		
Requirement	$W + D^{(*)}$ SR	Top CR
$N(b\text{-jet})$	0	≥ 1
E_T^{miss}	> 30 GeV	
m_T	> 60 GeV	
Lepton p_T	> 30 GeV	
Lepton $ \eta $	< 2.5	
$N(D^{(*)})$	≥ 1	
$D^{(*)} p_T$	> 8 GeV and < 150 GeV	
$D^{(*)} \eta $	< 2.2	
(b)		
Truth fiducial selection		
Requirement	$W + D^{(*)}$	
$N(b\text{-jet})$...	
E_T^{miss}	...	
m_T	...	
Lepton p_T	> 30 GeV	
Lepton $ \eta $	< 2.5	
$N(D^{(*)})$	≥ 1	
$D^{(*)} p_T$	> 8 GeV	
$D^{(*)} \eta $	< 2.2	

increases rapidly and thus reduces the reconstruction efficiency and degrades the resolution. The upper p_T cut is applied to reject the background from fake $D^{(*)}$ mesons at high momentum and, because the predicted fraction of $D^{(*)}$ mesons with $p_T(D^{(*)}) > 150$ GeV is small, it has no significant impact on the signal reconstruction efficiency. The full set of selection requirements for the $D^{(*)}$ candidates is summarized in Table III.

VI. EVENT SELECTION

Events for the analysis are selected through requirements on leptons, E_T^{miss} , jets, and $D^{(*)}$ mesons satisfying the criteria defined in Secs. IV and V and passing the single-lepton triggers as discussed in Sec. III. Reconstruction of W bosons is based on their leptonic decays to either an electron ($W \rightarrow e\nu_e$) or a muon ($W \rightarrow \mu\nu_\mu$). The lepton is measured in the detector and the presence of a neutrino is inferred from E_T^{miss} . Events are required to have exactly one tight lepton with $p_T > 30$ GeV and $|\eta| < 2.5$. Events with additional loose leptons are rejected. To reduce the multijet background and enhance the W boson signal

purity, additional requirements are imposed: $E_T^{\text{miss}} > 30$ GeV and $m_T > 60$ GeV, where the W boson transverse mass (m_T) is defined as $\sqrt{2p_T(\text{lep})E_T^{\text{miss}}(1 - \cos(\Delta\phi))}$ and $\Delta\phi$ is the azimuthal separation between the lepton and the missing transverse momentum. Candidate $D^{(*)}$ mesons are reconstructed using a secondary-vertex fit as described in Sec. V. Any number of $D^{(*)}$ meson candidates satisfying these criteria are selected, which accounts for the production of multiple mesons in a single event. Only events with one or more $D^{(*)}$ candidates are selected.

Events selected in this way are used to extract the $W + D^{(*)}$ observables with a profile likelihood fit defined in Sec. VIII. Furthermore, the selected events are categorized according to the b -jet multiplicity to separate the $W + D^{(*)}$ signal process from the $t\bar{t}$ background with events containing $W \rightarrow c\bar{s}$ decays. The ID tracks associated with the reconstructed $D^{(*)}$ candidates are often also associated with a jet mistagged as a b -jet. To avoid categorizing these $W + D^{(*)}$ signal events as events with one or more b -jets, the b -jets are required to be geometrically separated from reconstructed $D^{(*)}$ mesons by satisfying $\Delta R(b\text{-jet}, D^{(*)}) > 0.4$. Events with exactly zero such b -tagged jets are classified as the $W + D^{(*)}$ signal region (SR) and events with one or more b -tagged jets comprise the Top control region (CR). In this way about 80% of the $t\bar{t}$ background events are in the Top CR and about 99% of $W + D^{(*)}$ signal events remain in the $W + D^{(*)}$ SR, effectively reducing the amount of $t\bar{t}$ background. Collectively, the $W + D^{(*)}$ SR and Top CR are called the “fit regions.” These requirements are summarized in Table IV(a). The measured signal and background yields in the $W + D^{(*)}$ SR are given in Sec. X. The yield of $W + D^{(*)}$ signal events is about 5% of the $t\bar{t}$ background yield in the Top CR.

The analysis exploits the charge correlation of the W boson and the charm quark to enhance the signal and reduce the backgrounds. The signal has a W boson and a $D^{(*)}$ meson of opposite charge, while most backgrounds are symmetric in charge. Therefore, the signal is extracted by measuring the difference between the numbers of OS and SS $W + D^{(*)}$ candidates, which is referred to as OS–SS. While the signal-to-background ratio is about unity in the OS region, the OS–SS $W + D^{(*)}$ signal is an order of magnitude larger than the remaining background after the subtraction.

The $W + D^{(*)}$ measurement is unfolded to a “truth” fiducial region defined at MC particle level to have exactly one truth lepton with $p_T(\ell) > 30$ GeV and $|\eta(\ell)| < 2.5$. The lepton must originate from a W boson decay, with τ decays excluded from the fiducial region. Lepton momenta are calculated using “dressed” leptons, where the four-momenta of photons radiated from the final-state leptons within a cone of $\Delta R = 0.1$ around the lepton are

added to the four-momenta of leptons. Truth $D^{(*)}$ mesons are selected by requiring $p_T(D^{(*)}) > 8$ GeV and $|\eta(D^{(*)})| < 2.2$. The OS–SS subtraction is also applied to the truth fiducial events. This removes any charge-symmetric processes, which are expected to originate mostly from gluon splitting in the final state. The E_T^{miss} and m_T requirements and b -jet veto are not applied in the fiducial selection. The truth fiducial selection is summarized in Table IV(b). The fiducial efficiency is defined as the fraction of $W + D^{(*)}$ signal events from the truth fiducial region that pass the detector-level reconstruction and requirements in Table IV(a). In the unfolding, events where the reconstructed objects pass the event selection but the truth objects fail the truth fiducial requirements are treated as fakes; cases where the reconstructed objects fail the reconstruction fiducial selection but the truth objects pass the truth selection are treated as inefficiencies.

VII. SIGNAL AND BACKGROUND MODELING

MC samples are used to construct signal and background mass templates, except for the multijet background, which is determined using a data-driven method (Sec. VII C). Generally, Sherpa 2.2.11 MC samples are used to model events containing a single W boson and one or more reconstructed $D^{(*)}$ meson candidates because they provide the highest precision when simulating QCD processes and the highest statistical power among the available samples. For specific purposes, MG+Py8 (CKKW-L) and aMC@NLO+Py8 (NLO) MC samples are used in conjunction with Sherpa to account for shortcomings in Sherpa modeling of $D^{(*)}$ meson decays as described in Secs. VII A and VII B. MC truth information is used to categorize the MC $W + D^{(*)}$ events according to the origin of the tracks used to reconstruct the $D^{(*)}$ meson candidate:

- (i) $W + D^{(*)}$ signal: If all tracks originate from the signal charmed hadron species (D^+ or D^*) and are assigned in the reconstruction to the correct particle species ($K^\mp \pi^\pm \pi^\pm$), then that reconstructed $D^{(*)}$ candidate is labeled as $W + D^{(*)}$ signal.
- (ii) $W + c^{\text{match}}$: If all tracks originate either from a different charmed hadron species (D^0 , D_s , or c -baryon) or from a different decay mode of a signal charmed meson [e.g. $D^+ \rightarrow \phi \pi^+ \rightarrow (K^+ K^-) \pi^+$], the reconstructed $D^{(*)}$ candidate is labeled as $W + c^{\text{match}}$.
- (iii) $W + c^{\text{mismatch}}$: If at least one but not all tracks belong to a single charmed hadron, the reconstructed $D^{(*)}$ candidate is labeled as $W + c^{\text{mismatch}}$.
- (iv) $W + \text{jets}$: If none of the tracks are matched to a particle originating from a charmed particle, the $D^{(*)}$ candidate is labeled $W + \text{jets}$. This is the combinatorial background from the underlying event and pile-up.

Additional background categories modeled using MC simulation are the following:

- (i) Top: Processes containing top quarks ($t\bar{t}$, single- t , $t\bar{t}X$) are jointly represented by the “Top” category, which is dominated by the $t\bar{t}$ process.
- (ii) Other: Events from diboson and $Z + \text{jets}$ processes are combined into the “Other” category.

The signal and background samples used in the $W + D^+$ and $W + D^{*+}$ fits are given in Table V. The rates at which c -quarks hadronize into different species of weakly decaying charmed hadrons in the MC samples are reweighted to the world-average values [55]. The weights improve agreement between data and MC simulation by modifying the signal and background normalizations and the shapes of the $W + D^{(*)}$ background templates by changing the relative contribution of each species. The normalization of the background templates changes by up to 3%, depending on the $D^{(*)}$ species.

TABLE V. Single- W -boson MC samples employed to create mass templates used in the $W + D^{(*)}$ fits. The “Normalization” and “shape” columns indicate the source used to calculate the corresponding property. “LIS” refers to the loose inclusive selection explained in the text, and $m(D^{(*)})$ stands for $m(D^+)$ in the D^+ channel and $m(D^{*+} - D^0)$ in the D^* channel. The MC configurations used to model these backgrounds are described in Sec. III B. Preferentially, Sherpa samples are used for signal and background modeling. There are some exceptions to account for the shortcomings as explained in the text (e.g. incorrect D^{*+} decay with in Sherpa).

Category	Normalization	$m(D^{(*)})$ shape
$W + D^{(*)}$ (D^+ channel)	Sherpa 2.2.11	Sherpa 2.2.11
$W + D^{(*)}$ (D^* channel)	Sherpa 2.2.11	aMC@NLO+Py8 (NLO)
$W + c^{\text{match}}$ (D^+ channel)	MG+Py8 (CKKW-L)	MG+Py8 (CKKW-L)
$W + c^{\text{match}}$ (D^* channel)	Sherpa 2.2.11	Sherpa 2.2.11
$W + c^{\text{mismatch}}$	Sherpa 2.2.11	LIS Sherpa 2.2.11
$W + \text{jets}$ (D^+ channel)	Sherpa 2.2.11	LIS Sherpa 2.2.11
$W + \text{jets}$ (D^* channel)	MG+Py8 (CKKW-L)	LIS MG+Py8 (CKKW-L)

A. Signal modeling

The Sherpa 2.2.11 $W + D^+$ signal sample with EvtGen decays is used for the modeling of the mass template in the D^+ channel. However, because the width of the D^{*+} meson is set incorrectly in Sherpa 2.2.11, the mass shape in the D^{*+} channel is taken from the `amc@NLO+Py8` (NLO) $W + D^{*+}$ signal sample instead. In both channels the normalization is taken from Sherpa 2.2.11 because it provides the best available statistical power for calculating the fiducial efficiency.

B. Modeling backgrounds with a single W boson

The $W + c^{\text{match}}$ background in the D^+ channel is modeled using MG+Py8 (CKKW-L) because the EvtGen decay tables and models used with MG+Py8 (CKKW-L) provide a better description of the D meson decay rates and kinematics than those implemented in Sherpa 2.2.11. Corrections to account for LO \rightarrow NLO effects in $W + D^{(*)}$ production are applied by reweighting the MG+Py8 (CKKW-L) MC truth distribution of $p_T(D^+)$ to the corresponding Sherpa 2.2.11 distribution. Sherpa 2.2.11 is also used in the D^{*+} channel.

The $W + c^{\text{mismatch}}$ backgrounds are modeled using Sherpa 2.2.11 in both the D^+ and D^{*+} channels. The $W + \text{jets}$ background is modeled using Sherpa 2.2.11 in the D^+ channel and MG+Py8 (CKKW-L) in the D^{*+} channel because their descriptions of this background yield and invariant mass shape are closer to the data before the fit. These background MC samples suffer from large statistical uncertainties. A loose inclusive selection (LIS) method was developed to reduce these uncertainties. The LIS method is based on the observation that, for these backgrounds, the $D^{(*)}$ meson mass shapes are the same for both W boson charges and do not depend on the E_T^{miss} and m_T cuts. Therefore, the LIS can be used to construct mass templates inclusively and without E_T^{miss} and m_T cuts. These inclusive mass distributions are then used for both W boson charges. In the D^{*+} channel, the LIS $W + \text{jets}$ background is fitted with a parametric function. This parametric function is then used to generate the template histogram which is used in the $W + D^{*+}$ fit.

C. Data-driven multijet background estimation

Multijet backgrounds arise if one or more constituents of a jet are misidentified as a prompt lepton. In the electron channel, multijet events pass the electron selection due to having misidentified hadrons, converted photons, or semi-leptonic heavy-flavor decays. In the muon channel, muons from heavy-flavor hadron decays are the dominant source. Collectively, these backgrounds are called “fake and non-prompt leptons.” MC-based predictions for the normalization and composition of these backgrounds suffer from large uncertainties. The background rate is therefore determined using the data-driven matrix method [113].

The matrix method takes advantage of the fact that fake and nonprompt leptons (F) are less well isolated than real leptons (R). Leptons can be split independently in two ways: by origin, R and F, or by the `tight` (T) and `loose` reconstruction criteria defined in Table II. Leptons satisfying the `loose` but not the `tight` criteria are labeled as `antitight` (!T). While the abundances of R and F leptons (N_R and N_F) are not directly measurable in data, they can be related to the measurable numbers of `tight` and `antitight` leptons (N_T and $N_{!T}$) via the efficiency r (f) for a `loose` real (fake) lepton to also be `tight`:

$$\begin{pmatrix} N_T \\ N_{!T} \end{pmatrix} = \begin{pmatrix} r & f \\ 1-r & 1-f \end{pmatrix} \begin{pmatrix} N_R \\ N_F \end{pmatrix}.$$

This expression is inverted to give an expression for the number of fake and nonprompt leptons in the $W + D^{(*)}$ SR, dependent on measurable quantities,

$$N_T^{\text{fake}} = \frac{f}{r-f} ((r-1)N_T + rN_{!T}).$$

This matrix method relation is applied bin by bin to estimate the multijet background yield in the variable of interest.

The real-lepton efficiency r is determined from the data in auxiliary measurements [98,99] and extrapolated to the $W + D^{(*)}$ SR using MC samples. The real-lepton efficiency is estimated in three (four) bins in η for electrons (muons) and in p_T bins of 6 GeV width.

The fake-lepton efficiency f is computed from the data in a dedicated region enriched in fake and nonprompt leptons, called the Fake CR. This region, orthogonal to the $W + D^{(*)}$ SR, is selected by inverting the E_T^{miss} and m_T requirements to $E_T^{\text{miss}} < 30$ GeV and $m_T < 40$ GeV. These requirements reduce the contribution of real leptons originating from W boson decays. To further increase the Fake CR’s purity in fake and nonprompt leptons, processes with real leptons are estimated from MC simulation and subtracted from both `tight` and `antitight` subsets of Fake CR. The OS–SS subtraction is not performed for the calculation of the fake-lepton efficiencies because the multijet background is largely symmetric in OS and SS events. The number of `tight` leptons divided by the sum of `tight` and `antitight` gives the fake-lepton efficiency. The efficiency is estimated in three (four) bins in η for electrons (muons) and in p_T bins of 5 to 20 GeV width, depending on the available sample size. The fake-lepton efficiency, in the Fake CR, is in the range 50%–90% or 10%–70% for electrons and muons respectively.

Systematic uncertainties in the multijet estimation arise from several sources. Statistical uncertainties in the determination of the real- and fake-lepton efficiencies lead to systematic uncertainties of approximately 10% to 20% in the overall multijet yield. Uncertainties in the size of the

real-lepton contamination in the Fake CR are assessed using two methods. First, the change in rate due to varying the QCD renormalization and factorization scales in MC samples is obtained. Second, the difference between the prompt rates determined using MG+Py8 (CKKW-L) or Sherpa 2.2.11 W + jets MC samples is evaluated. These two variations together result in relative uncertainties on the multijet yield of $\sim 20\%$ for the D^+ channel and $\sim 30\%$ for the D^{*+} channel.

An additional systematic uncertainty is derived to account for the dependence of fake-lepton efficiencies on E_T^{miss} , which may arise from the different composition of fake background processes depending on the E_T^{miss} (e.g. misidentified hadrons or semileptonic heavy-flavor decays), the correlation between the lepton isolation variables and E_T^{miss} , and the tendency of misidentified objects (e.g. jets misidentified as electrons) to give rise to E_T^{miss} due to an incorrect assumption about the object type in their energy calibration. To estimate this, the Fake CR's E_T^{miss} cut is inverted to require $E_T^{\text{miss}} > 30$ GeV while its m_T cut is retained to ensure orthogonality with the $W + D^{(*)}$ SR. This process provides an independent estimate of the multijet background. Differences between the multijet background yields in the $W + D^{(*)}$ SR obtained with these two choices of Fake CR cuts are $\sim 50\%$ for D^+ and $\sim 60\%$ for D^{*+} . While this multijet background estimate has large systematic uncertainties, the multijet yield in the $W + D^{(*)}$ SR is only up to 1% of the signal yield in the electron channel and negligible in the muon channel. Thus the multijet background uncertainties are subdominant when estimating the overall background yield.

Figure 2 demonstrates the extrapolation of the multijet background from the Fake CR to the $W + D^{(*)}$ SR. Without the OS–SS subtraction, most of the D mesons in the Top background originate from B meson decays. This background is larger in the D^+ channel than in the D^* channel because the slow pion in the D^* reconstruction chain is required to be associated with the PV and charmed mesons produced in B meson decays often fail this requirement due to the sizable average lifetime of the B mesons. The central values of the fake-lepton efficiencies are calculated in the $m_T < 40$ GeV region, but with the E_T^{miss} requirement inverted ($E_T^{\text{miss}} < 30$ GeV). The figure instead shows the events with the $E_T^{\text{miss}} > 30$ GeV requirement corresponding to the $W + D^{(*)}$ SR selection. The prediction disagrees with the data at low m_T due to an E_T^{miss} dependence in the fake-lepton efficiencies that is not directly accounted for in the parametrization. A systematic uncertainty is introduced, as described above, by calculating the fake-lepton efficiencies with the $E_T^{\text{miss}} > 30$ GeV requirement and taking the full difference between the two multijet predictions as the uncertainty. Since this is the largest systematic uncertainty in the multijet background, the data are almost exactly covered by the one-standard-deviation variation in this

region. Furthermore, the multijet prediction and the uncertainties are extrapolated into the $W + D^{(*)}$ SR with the $m_T > 60$ GeV requirement. To validate the extrapolation, the prediction is evaluated in a validation region (VR) with an m_T requirement of $40 \text{ GeV} < m_T < 60 \text{ GeV}$. Figure 2 shows that the prediction in the VR is in agreement with the data within the systematic uncertainties, indicating that the multijet background is modeled well enough.

VIII. CROSS-SECTION DETERMINATION

A statistical fitting procedure based on the standard profile-likelihood formalism used in LHC experiments [114,115] is used to extract the observables from the data with corresponding uncertainties:

- (i) absolute fiducial cross sections: $\sigma_{\text{fid}}^{\text{OS-SS}}(W^- + D^{(*)})$ and $\sigma_{\text{fid}}^{\text{OS-SS}}(W^+ + D^{(*)})$,
- (ii) the cross-section ratio: $R_c^\pm = \sigma_{\text{fid}}^{\text{OS-SS}}(W^+ + D^{(*)}) / \sigma_{\text{fid}}^{\text{OS-SS}}(W^- + D^{(*)})$, and
- (iii) differential cross sections for OS–SS $W^- + D^{(*)}$ and $W^+ + D^{(*)}$.

The likelihood fit enables the estimation of background normalization and constraining of systematic uncertainties *in situ* by extracting the information from the data in mass-peak sidebands and control regions. It is a crucial ingredient in achieving percent-level precision in the $W + D^{(*)}$ cross-section measurement. The formalism of the profile likelihood fit is given in Sec. VIII A, Sec. VIII B explains how the “OS–SS” subtraction is incorporated, Sec. VIII C introduces the measurement of normalized differential cross sections, and Sec. VIII D defines the bin edges of the measured differential variables.

A. The profile likelihood fit

A binned likelihood function, $\mathcal{L}(\vec{\sigma}, \vec{\theta})$, is constructed as the product of Poisson probability terms for each bin of the input mass distributions, based on the number of data events and the expected signal and background yields. The product over the mass bins is performed for each differential bin, in bins of either $p_T(D^{(*)})$ or $|\eta(\ell)|$. The reconstructed invariant mass of the D^+ meson, $m(D^+)$, is used as input in the D^+ channel and the mass difference $m(D^{*+} - D^0)$ is used in the D^* channel because it has better resolution than the D^* invariant mass. The invariant mass bins in the $W + D^{(*)}$ SR are narrower in the peak region (with about eight bins) and wider in the tails, where the shape is more uniform (up to four bins). Only a single bin is fitted in each Top CR. The integrated $W + D^{(*)}$ SR invariant mass distributions are shown in Fig. 5 in Sec. X. The impact of systematic uncertainties is included via nuisance parameters, $\vec{\theta}$. Separate likelihood fits are performed for the D^+ and D^{*+} channels and for $p_T(D^{(*)})$ and $|\eta(\ell)|$ distributions. A likelihood equation describing this fitting procedure is given in Eqs. (1)–(4):

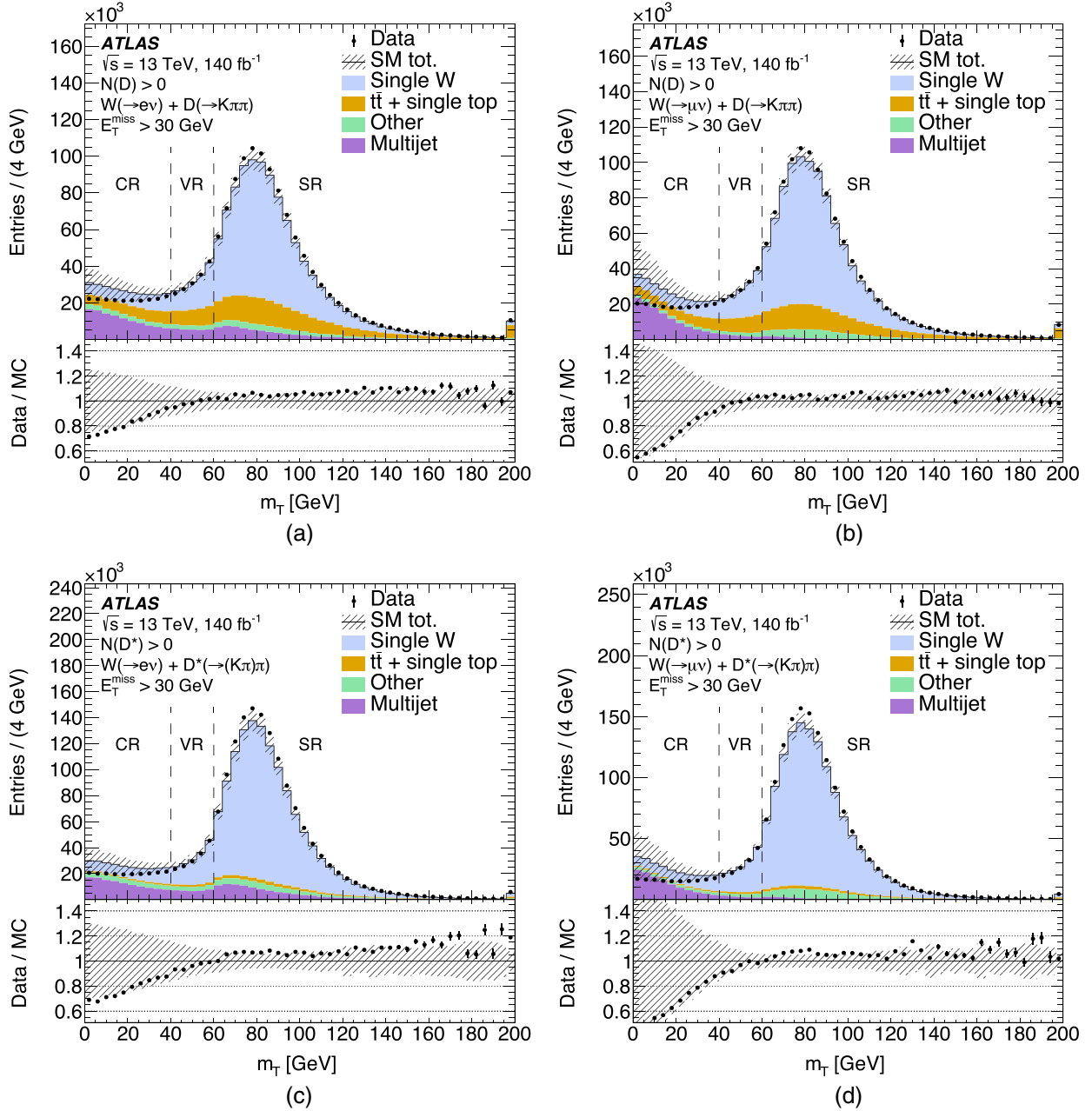


FIG. 2. Modeling distributions of the m_T variable using the matrix method to estimate the multijet background. The distributions are (a) m_T in the D^+ electron channel, (b) m_T in the D^+ muon channel, (c) m_T in the D^{*+} electron channel, (d) m_T in the D^{*+} muon channel. The “SM Tot.” line represents the sum of all signal and background samples and the corresponding hatched uncertainty band includes all matrix method systematic uncertainties, E_T^{miss} systematic uncertainties, and QCD scale variations. The “Single W” component includes all contributions from Table V. The D and D^* stand for D^+ and D^{*+} mesons respectively and pion and kaon charges are omitted for brevity. Dashed vertical lines indicate the m_T values defining the control, validation, and signal regions (CR, VR, and SR) as explained in the text. The last bin also includes the events with $m_T > 200$ GeV. The prompt processes estimated with MC samples are normalized to the expected SM cross sections given in Sec. III B.

$$\mathcal{L}(\vec{\sigma}, \vec{\theta}) = \prod_{\alpha} \left(\prod_i^{W^- \text{OS}} \mathcal{L}(\vec{\sigma}, \vec{\theta})_i^{\alpha \text{OS}} \times \prod_i^{W^- \text{SS}} \mathcal{L}(\vec{\theta})_i^{\alpha \text{SS}} \times \prod_i^{W^+ \text{OS}} \mathcal{L}(\vec{\sigma}, \vec{\theta})_i^{\alpha \text{OS}} \times \prod_i^{W^+ \text{SS}} \mathcal{L}(\vec{\theta})_i^{\alpha \text{SS}} \right) \times \mathcal{L}^{\text{constr}}, \quad (1)$$

$$\mathcal{L}(\vec{\sigma}, \vec{\theta})_i^{\alpha \text{OS}} = f \left(N_i^{\alpha} |\gamma_i^{\alpha}| \cdot \left(\sum_{\beta} [\sigma_{\text{fid}}^{\beta} \cdot r^{\alpha\beta}(\vec{\theta}) \cdot \mathcal{P}_i^{\alpha\beta}(\vec{\theta})] \cdot \mathcal{L}(\theta_{\text{lumi}}) \cdot B_{D^{(*)}} + \mathcal{B}_i^{\alpha}(\vec{\theta}, \mu_{\text{Top}}) \right) + C_i^{\alpha} \right), \quad (2)$$

$$\mathcal{L}(\vec{\theta})^{\text{aSS}} = f(N_i^\alpha | \gamma_i^\alpha \cdot \mathcal{B}_i^\alpha(\vec{\theta}, \mu_{\text{Top}}) + c_i^\alpha), \quad (3)$$

$$\mathcal{L}^{\text{constr}} = \prod_t g(\theta_t) \times \prod_{\alpha,i} f(\gamma_i^\alpha), \quad (4)$$

where the index i represents the bins of the $D^{(*)}$ mass distribution (either OS or SS) both in the $n_{\text{bjet}} = 0$ $W + D^{(*)}$ SR, as well as the single bin used in the $n_{\text{bjet}} > 0$ Top CR. Indices α and β represent the detector-level and truth differential bins respectively, and the index t represents the nuisance parameters $\vec{\theta}$. The expression $f(k|\lambda) = \lambda^k e^{-\lambda}/k!$ is the Poisson probability density function. Furthermore,

- (i) N_i^α is the number of observed events in mass bin i and reconstructed differential bin α ,
- (ii) $\sigma_{\text{fid}}^\beta$ is the fiducial cross section in differential bin β (one parameter per differential bin and W boson charge),
- (iii) $r^{\alpha\beta}(\vec{\theta})$ is the detector response matrix defined as the fraction of $W + D^{(*)}$ events produced in truth fiducial bin β that also satisfy the $W + D^{(*)}$ SR reconstruction criteria in bin α ,
- (iv) $\mathcal{P}_i^{\alpha\beta}(\vec{\theta})$ is the i th bin of the mass shape distribution of the signal sample corresponding to truth differential bin β in reconstructed differential bin α (a separate invariant mass distribution for every non-zero bin in Fig. 3),
- (v) $\mathcal{L}(\theta_{\text{lumi}})$ is the integrated luminosity,
- (vi) $B_{D^{(*)}}$ is the branching ratio of either the D^+ or D^{*+} decaying into $K\pi\pi$ (Ref. [112]),
- (vii) $\mathcal{B}_i^\alpha(\theta, \mu_{\text{Top}})$ is the total number of background events in mass bin i and reconstructed differential bin α , including the $W + D^{(*)}$ signal events failing the truth fiducial selection [Table IV(b)],
- (viii) μ_{Top} is the normalization factor for the top-quark background,
- (ix) c_i^α is the ‘‘common floating component’’ in mass bin i and reconstructed differential bin α (mathematical construct to enable likelihood minimization in OS–SS described further in Sec. VIII B),
- (x) $\vec{\theta}$ represents all nuisance parameters that are profiled in the likelihood fit, and
- (xi) γ_i^α parameters are the Poisson-constrained parameters accounting for the MC statistical uncertainties in the combined signal-plus-background mass templates, following the simplified Beeston-Barlow technique [116].

The nuisance parameters $\vec{\theta}$ have Gaussian constraints $g(\theta)$ in the likelihood with a mean of 0 and a standard deviation that corresponds to the one-standard-deviation variations of the associated systematic uncertainties determined from auxiliary measurements (e.g. lepton calibration described in Sec. IV). The γ_i^α parameters are centered around 1 and may deviate from unity within

the corresponding Poisson constraints reflecting the combined signal-plus-background statistical uncertainty in the invariant mass templates.

Response matrices for the D^+ and D^{*+} channels are shown in Fig. 3 for differential $p_T(D^{(*)})$ and $|\eta(\ell)|$ bins for nominal values of the nuisance parameters. Differential cross sections extracted in this way correspond to unfolding with matrix inversion. No regularization techniques were used because the detector response matrices are nearly diagonal and because the statistical uncertainties are sufficiently low.

B. The OS–SS subtraction

A fitting procedure exploiting the charge correlation between the W boson and the $D^{(*)}$ meson was developed to perform the OS–SS subtraction within the likelihood fit. Instead of using OS–SS distributions in the fit, both the OS and SS regions enter the likelihood function and a common floating component is added in both regions. The additional component has one free parameter per invariant mass bin, and this parameter is correlated between the corresponding OS and SS regions. The common floating component is configured to absorb all charge-symmetric processes, which effectively translates the maximization of separate OS and SS likelihoods into a maximization of the OS–SS likelihood. This is done because the OS–SS event yields do not follow the Poisson distributions, which is a requirement for the data yields in the profile likelihood fit. Furthermore, this fitting procedure ensures that the yields of the individual signal and background components remain positive in the fit even though their OS–SS difference could be negative.

The method used to extract the OS–SS $\sigma_{\text{fid}}^{\text{OS-SS}}(W + D^{(*)})$ cross section from a simultaneous fit to OS and SS regions with the common floating component is demonstrated in Fig. 4 for the second bin of the $p_T(D^{(*)})$ distribution in the D^+ channel. The prefit OS, SS, and OS–SS distributions are shown on the left-hand side of Fig. 4 and the corresponding postfit distributions are on the right-hand side. The $W + D^+$ signal sample is split into three components (labeled bin 1, bin 2, and bin 3), which correspond to the diagonal and two off-diagonal elements immediately above and beneath the diagonal in Fig. 3(a). Since all other nondiagonal elements are zero, signal samples corresponding to truth fiducial bins 4 and 5 are not included. The common floating component is shown with the gray histograms named ‘‘Ch. Symm.’’ in the legend. The initial prefit values of the common floating component are arbitrary because every bin has a corresponding free parameter in the fit. This component is merely a mathematical construct to translate the minimization of separate OS and SS negative log-likelihoods into a minimization in OS–SS. The initial values in both the OS and SS regions are set to the difference between the data and the MC prediction in the SS region (different results

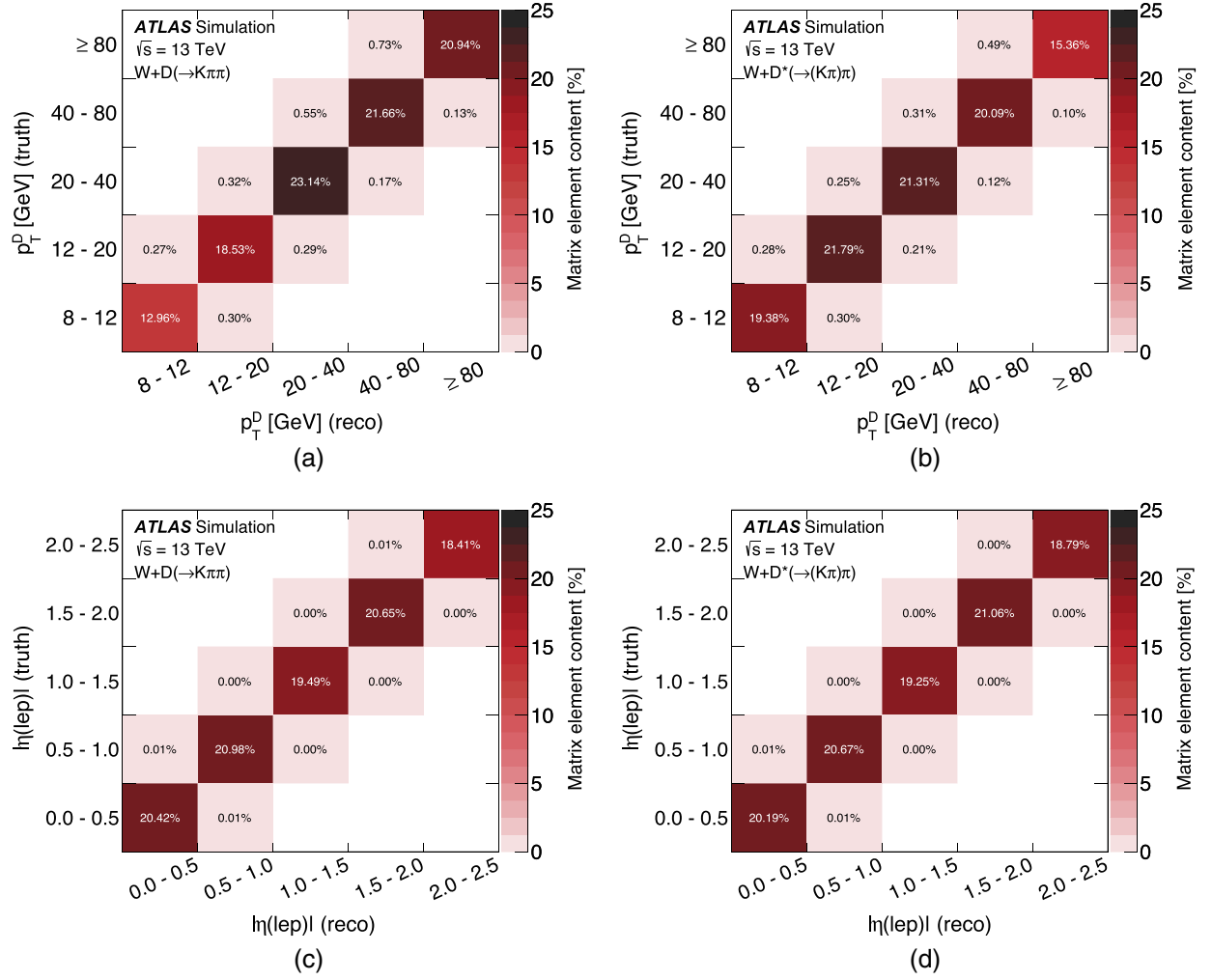


FIG. 3. The $W + D^{(*)}$ detector response matrix in differential $p_T(D^{(*)})$ bins (a) $W + D^+$, (b) $W + D^{*+}$, and in differential $|\eta(\ell)|$ bins (c) $W + D^+$, (d) $W + D^{*+}$. The detector response matrix is calculated with Sherpa 2.2.11 $W + D^{(*)}$ samples. The detector response matrices are normalized to unity such that the sum of all elements is 100%. The last $p_T(D^{(*)})$ bin has an upper cut of 150 GeV at the detector level, while there is no upper cut at the truth level.

were not observed with other initial values). This ensures that the initial signal-plus-background predictions are positive and not too far away from the minimum. The plots illustrate the effectiveness of the OS–SS subtraction; the backgrounds are almost symmetric in OS and SS regions, so the resulting OS–SS distributions are largely dominated by the $W + D^{(*)}$ signal.

C. Normalized differential cross section

Normalized differential cross sections are generally more powerful than absolute differential cross sections in distinguishing between the observed data and the theory predictions since overall systematic uncertainties such as those in the integrated luminosity and branching ratio cancel out in the normalized differential cross sections. To extract the normalized differential cross sections and the corresponding uncertainties, the fit is performed to extract the four

normalized cross sections and the total fiducial cross section, $\sigma_{\text{fid}}^{\text{tot}}$, instead of extracting the five absolute differential cross sections. By default, a substitution of the free parameters in the likelihood fit is made as shown in Eq. (5):

$$\begin{aligned}
 \sigma_{\text{fid}}^1 &\rightarrow \sigma_{\text{fid}}^{\text{tot}} \times \sigma_{\text{rel}}^1, \\
 \sigma_{\text{fid}}^2 &\rightarrow \sigma_{\text{fid}}^{\text{tot}} \times \sigma_{\text{rel}}^2, \\
 &\dots \\
 \sigma_{\text{fid}}^N &\rightarrow \sigma_{\text{fid}}^{\text{tot}} \times \left[1 - \sum_{i=1}^{N-1} \sigma_{\text{rel}}^i \right], \quad (5)
 \end{aligned}$$

where σ_{fid}^i is the absolute fiducial cross section in truth differential bin i and σ_{rel}^i is the corresponding normalized differential cross section. The value of N is 5 in all cases. By definition, the sum of all normalized differential cross sections is 1. This substitution is performed separately for

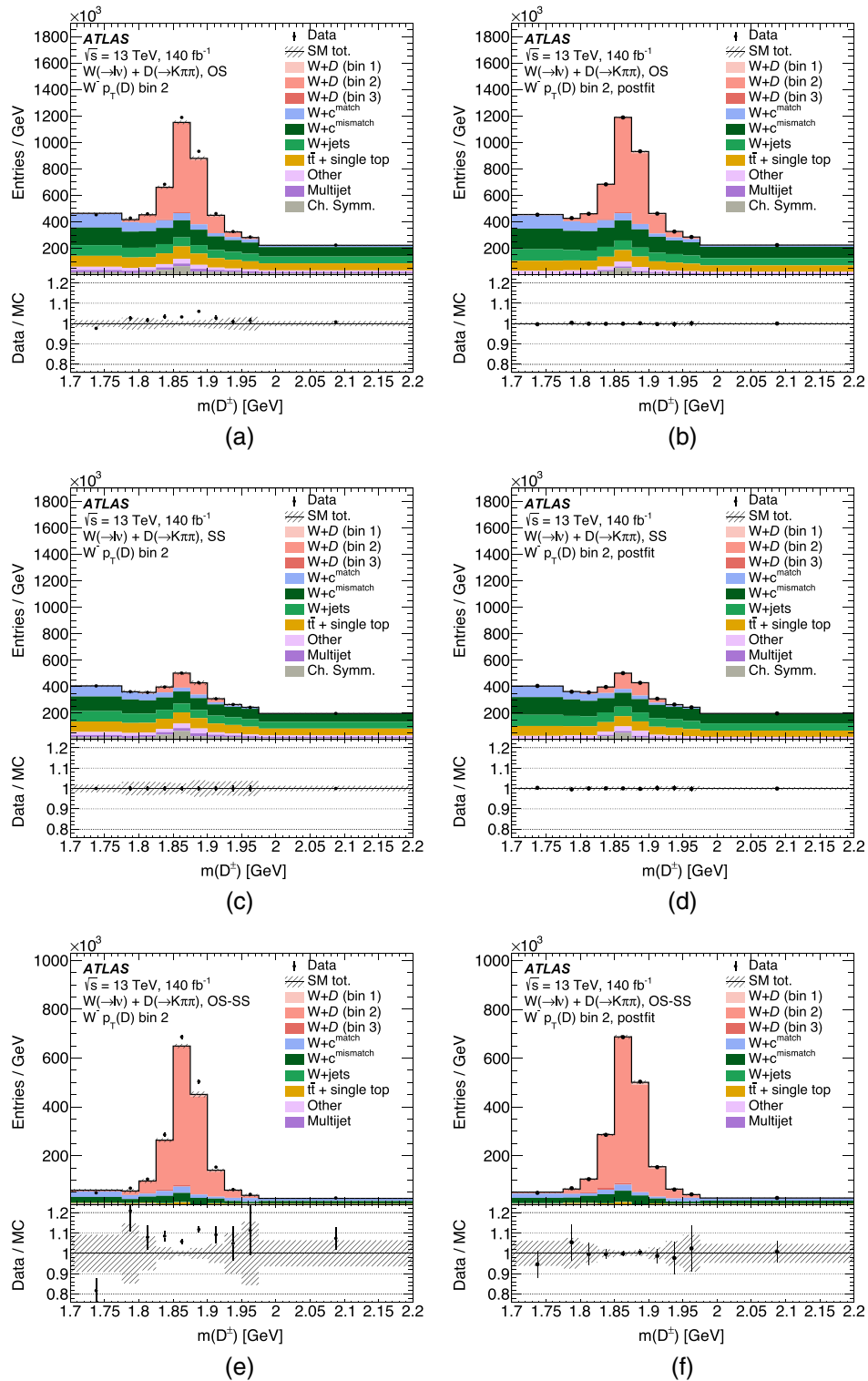


FIG. 4. A demonstration of the OS–SS $W + D^{(*)}$ cross-section fit. Prefit $m(D^+)$ distributions for the $W^- + D^+ p_T(D^+)$ bin 2: (a) OS, (b) SS, and (c) OS–SS. The corresponding postfit distributions: (d) OS, (e) SS, and (f) OS–SS. The SM Tot. line represents the sum of all signal and background samples. The corresponding prefit uncertainty bands include MC statistical uncertainties only and the postfit uncertainty bands include the total uncertainty extracted from the fit. The gray histograms represent the charge-symmetric common floating component and the three histograms associated with the signal samples are the truth bins of the $p_T(D^{(*)})$ differential distribution.

TABLE VI. The differential $p_T(D^{(*)})$ and $|\eta(\ell)|$ bins used in the measurement. The last $p_T(D^{(*)})$ bin has no upper limit.

Bin number	1	2	3	4	5
$p_T(D^{(*)})$ bin edges (GeV)	[8, 12]	[12, 20]	[20, 40]	[40, 80]	[80, ∞)
$ \eta(\ell) $ bin edges	[0.0, 0.5]	[0.5, 1.0]	[1.0, 1.5]	[1.5, 2.0]	[2.0, 2.5]

each charge, $W^+ + D^{(*)}$ and $W^- + D^{(*)}$. Furthermore, a similar substitution is made for the R_c^\pm parameter. The normalization factor for the $\sigma_{\text{fid}}^{\text{OS-SS}}(W^+ + D^{(*)})$ total fiducial cross section is replaced by the expression shown in Eq. (6):

$$\sigma_{\text{fid}}^{\text{tot}}(W^+ + D^{(*)}) \rightarrow R_c^\pm \times \sigma_{\text{fid}}^{\text{tot}}(W^- + D^{(*)}). \quad (6)$$

The free parameters in the fit after these substitutions are $\sigma_{\text{rel}}^1, \dots, \sigma_{\text{rel}}^{N-1}$ for each charge (eight parameters in total), R_c^\pm , and $\sigma_{\text{fid}}^{\text{tot}}(W^- + D^{(*)})$. The central values of all additional observables can be deduced from these free parameters; however, systematic uncertainties can only be calculated for the parameters directly included in the fit (with a likelihood scan explained in Sec. IX A). To achieve this, several fits with different substitutions of parameters are performed:

- (1) $\sigma^1(W^- + D^{(*)}), \dots, \sigma^N(W^- + D^{(*)}), \sigma^1(W^+ + D^{(*)}), \dots, \sigma^N(W^+ + D^{(*)})$,
- (2) $\sigma_{\text{rel}}^1(W^- + D^{(*)}), \dots, \sigma_{\text{rel}}^{N-1}(W^- + D^{(*)}), \sigma_{\text{rel}}^1(W^+ + D^{(*)}), \dots, \sigma_{\text{rel}}^{N-1}(W^+ + D^{(*)})$, $R_c^\pm, \sigma_{\text{fid}}^{\text{tot}}(W^- + D^{(*)})$, and
- (3) $\sigma_{\text{rel}}^2(W^- + D^{(*)}), \dots, \sigma_{\text{rel}}^N(W^- + D^{(*)}), \sigma_{\text{rel}}^2(W^+ + D^{(*)}), \dots, \sigma_{\text{rel}}^N(W^+ + D^{(*)})$, $\sigma_{\text{fid}}^{\text{tot}}(W^+ + D^{(*)}), R_c^\pm$.

These three fits allow a precise determination of the central values and systematic uncertainties of all observables, including absolute and normalized differential cross sections. In all cases the number of free parameters is the same and the minimization procedure reaches the same minimum, yielding identical results.

D. Differential cross-section bins

The bin edges of the five differential $p_T(D^{(*)})$ bins are given in Table VI. The last bin starts at 80 GeV and has no upper limit. The number of bins and the bin edges were chosen such that the expected data statistical uncertainty is about 1%–2% in the first four bins. The available MC sample sizes also play an important role in determining the bin size; up to a 1% statistical uncertainty is present in the diagonal elements of the detector response matrix. Similar to the $p_T(D^{(*)})$ fits, five bins are chosen in $|\eta(\ell)|$ to provide percent-level precision. Furthermore, the absolute value of the pseudorapidity is used to further reduce the statistical uncertainty because there is no additional discriminating power in measuring the sign of the pseudorapidity. The $|\eta(\ell)|$ bin edges are also given in Table VI.

With five differential bins per W boson charge there are ten differential cross sections in total represented with the free parameters $\vec{\sigma}$ in the likelihood fit. Regions with both charges of the W boson are included in the fit at the same time in order to extract the cross-section ratio R_c^\pm . SRs in the $n_{\text{bjet}} = 0$ category are split between the two W charges, into OS and SS events, and into the five differential bins: $[W^-, W^+] \times [\text{OS}, \text{SS}] \times 5 = 20$ regions. The $n_{\text{bjet}} > 0$ CRs are split in the same way with the exception of differential bins since the normalization of the backgrounds from top-quark production is extracted from the data only inclusively. The relative contribution of the top-quark background in the $W + D^{(*)}$ SR is small (about 5% of the signal yield for D^+ and negligible for D^*), so the modeling of the differential spectrum in the top-quark background simulation has a negligible impact on the result. The regions used in the fit are summarized in Table VII.

TABLE VII. A schematic of the signal and control regions (SR and CR) used in the fit. The bin numbers correspond to either the $p_T(D^{(*)})$ or $|\eta(\ell)|$ differential bins listed in Table VI. The table indicates that the invariant mass distribution is fitted in each $W + D^{(*)}$ SR, with $m(D^{(*)})$ standing for $m(D^+)$ in the D^+ channel and $m(D^{*+} - D^0)$ in the D^* channel, while only a single bin is fitted in the Top CR.

W charge	$W + D^{(*)}$ SR ($n_{\text{bjet}} = 0$)				Top CR ($n_{\text{bjet}} > 0$)			
	W^-		W^+		W^-		W^+	
$D^{(*)}$ charge	OS	SS	OS	SS	OS	SS	OS	SS
Bin 1								
Bin 2								
Bin 3	Fit the $m(D^{(*)})$ distribution				Fit total yield			
Bin 4								
Bin 5								

IX. SYSTEMATIC UNCERTAINTIES

The measurements in this analysis are affected by several sources of systematic uncertainty. The first category related to detector-interaction and reconstruction processes, includes uncertainties in lepton and jet reconstruction, energy resolution, and energy scale, in lepton identification, isolation, and trigger efficiencies, in b -jet tagging efficiencies, and in the total integrated luminosity and pileup reweighting. These uncertainties affect the $W + D^{(*)}$ signal efficiency by altering the detector response matrix, yields of the background processes estimated with MC simulation, and the signal and background invariant mass templates used in the profile likelihood. These uncertainties are correlated between all samples and regions in the likelihood fit and are generally derived from auxiliary measurements:

Charged leptons: Electron and muon reconstruction, isolation, identification, and trigger efficiencies, and the energy/momentum scale and resolution are derived from data using large samples of $J/\psi \rightarrow \ell\ell$ and $Z \rightarrow \ell\ell$ events [98,99]. Systematic variations of the MC efficiency corrections and energy/momentum calibrations applied to MC samples are used to estimate the signal selection uncertainties.

Jets and missing transverse momentum: Jet energy scale and energy resolution uncertainties affect the signal efficiency and background yields indirectly by altering the reconstructed E_T^{miss} in the event and hence the selection efficiency of the E_T^{miss} and m_T cuts. Systematic variations of the jet energy calibration are applied to MC samples to estimate signal section uncertainties using the methodology described in Ref. [104]. In total, there are 20 independent jet energy scale variations and eight independent jet energy resolution variations. None of the single variations have an impact of more than 1% on the signal selection efficiency. Similarly, variations in E_T^{miss} reconstruction are derived specifically for the soft-term estimation following the methodology in Ref. [110]. Furthermore, a single nuisance parameter is included to model the uncertainty in the JVT selection efficiency.

Flavor tagging: The uncertainty in the calibration of the b -tagging efficiencies and mistag rates is derived from data using samples of dileptonic $t\bar{t}$ events for b -jets and c -jets [106,117] and a data sample enriched in light-flavor jets for light jets [118]. Since the majority (>99%) of $W + D^{(*)}$ signal events have no additional b -tagged jets, these variations have a negligible impact on the signal efficiency. Nevertheless, the variations in b -tagging efficiency have an impact of up to 10% on the relative yields of the top-quark backgrounds in the $W + D^{(*)}$ SR and Top CR.

Pileup and luminosity: The uncertainty in the integrated luminosity is 0.83% [44], which is obtained using the LUCID-2 detector [45] for the primary luminosity measurements. MC samples are reweighted to have the number

of pile-up vertices match the pile-up distribution measured in the Run 2 data. To account for the uncertainty in the pile-up estimation, variations of the reweighting are applied to the MC samples. In addition to affecting the background yields, it also has a small impact on the resolution of the reconstructed D^+ meson mass peak and the $m(D^{*+} - D^0)$ mass difference.

SV reconstruction: Uncertainties in the secondary-vertex reconstruction efficiency arise from potential mismodeling of the amount and location of ID material, from the modeling of hadronic interactions in GEANT4, and from possible differences between the impact-parameter resolutions in data and MC events. These uncertainties are evaluated by generating large single-particle samples of D^+ and D^{*+} decays with the same p_T and η distributions as the baseline $W + D^{(*)}$ MC samples. These “single-particle gun” (SPG) samples are simulated multiple times with different simulation parameters, mirroring the procedure in Ref. [111]: passive material in the whole ID scaled up by 5%, passive material in the IBL scaled up by 10%, and passive material in the Pixel detector services scaled by 25%. In addition to the variations in the amount of detector material, a SPG sample where the physics model in the GEANT4 toolkit was changed to QGSP_BIC from FTFP_BERT [49] was generated.

The impact of the uncertainty in the ID material distribution is evaluated by comparing the efficiency obtained using the baseline simulation and that obtained using altered material distributions. For each variation the relative change in the $D^{(*)}$ reconstruction efficiency is parametrized as a function of $p_T(D^{(*)})$ and $\eta(D^{(*)})$ separately for positive and negative charges of the mesons and separately for D^+ and D^{*+} mesons. The impact of changing the physics model was found to be negligible. The relative change in the reconstruction efficiency due to the increased amount of the ID material was found to vary by 1%–4%. The uncertainty is largest for low $p_T(D^{(*)})$ and high $\eta(D^{(*)})$. Because $D^{(*)}$ candidates in the signal and in the $t\bar{t}$ background do not necessarily have the same $p_T(D^{(*)})$ spectrum, their tracking efficiency NPs are treated as separate parameters to minimize the correlation between them. The $t\bar{t}$ background has large yields in the Top CR and could affect the shape of the $p_T(D^{(*)})$ signal distribution via pulls in the tracking efficiency uncertainties. The measured cross sections would change by up to 1.0% if the parameters were correlated, but this difference is covered by the associated systematic uncertainties.

Furthermore, the effect of the ID material variations on the shape of the D^+ invariant mass peak and the $m(D^{*+} - D^0)$ mass difference is evaluated by fitting the mass distributions with a double-sided Crystal Ball function, with yield modeling decoupled from the peak position. The width and position of the peak are characterized with the width and mean of the central Gaussian distribution respectively. The shift in the position of the D^+ (D^{*+}) peak was found to be up

to 0.2 MeV (0.05 MeV). The impact on the resolution of the peak was evaluated from the difference between the squares of the nominal width and the width obtained from each variation. The resolution was found to be smeared by up to 4.0 MeV (0.2 MeV) for the D^+ (D^{*+}) peak. The variations in the peak position and resolution are implemented in the likelihood fit as shape uncertainties with no impact on the signal yield, but this additional freedom in the fit is necessary to achieve good agreement between the data and the fit model.

An additional systematic uncertainty is applied to cover ID track impact-parameter resolution differences between simulation and data after the ID alignment is performed [119]. The difference is evaluated using minimum-bias data and the resulting uncertainty is extrapolated to higher p_T with muon tracks from Z boson decays [111]. The uncertainty is propagated to the $W + D^{(*)}$ measurement by generating D^+ and D^{*+} SPG samples where the impact parameters of the ID tracks are smeared before performing the SV fit for the $D^{(*)}$ reconstruction. The relative change in the $D^{(*)}$ reconstruction efficiency was found to be up to 5% for high- p_T $D^{(*)}$ mesons and about 1.5% at low p_T (i.e. $p_T < 40$ GeV). The systematic uncertainties in the $D^{(*)}$ meson reconstruction efficiency related to ID track impact-parameter resolution and ID material variations are among the largest systematic uncertainties in the analysis.

Signal modeling: The signal modeling uncertainty is derived by comparing the fiducial region efficiencies for the signal Sherpa 2.2.11, aMC@NLO+Py8 (FxFx), and aMC@NLO+Py8 (NLO) $W + D^{(*)}$ simulations. In each differential bin, the maximum difference between the nominal MC simulation (Sherpa) and either of the MadGraph5_aMC@NLO simulations is taken and a symmetric systematic uncertainty is applied in the two directions. The uncertainty is correlated between the differential bins and W boson charges. It accounts for the fact that the choice of MC simulation for unfolding affects the measured values of the observables because of differences in the ME calculation, PS simulation, and heavy-flavor quark fragmentation and hadronization. The uncertainty ranges from 1% to 4%, depending on the bin, and is generally one of the largest uncertainties in the analysis. The relatively large difference in fiducial efficiency between Sherpa and MadGraph5_aMC@NLO simulations arises from the modeling of the correlation between W boson and $D^{(*)}$ meson kinematics when the E_T^{miss} and m_T cuts are applied at the detector level. Including the same E_T^{miss} and m_T cuts in the truth fiducial definition would reduce the uncertainty; however, it would give rise to a large background from signal $W + D^{(*)}$ events that fail the truth E_T^{miss} and m_T selection, but pass the detector-level selection due to the poor E_T^{miss} resolution, ultimately increasing the total uncertainty.

Additional uncertainties are considered by varying the QCD scales, the PDFs, α_s , and the virtual EW corrections

in Sherpa 2.2.11. The PDF variations, α_s uncertainty, and EW corrections were found to have a negligible effect on the fiducial efficiency. The effect of QCD scale uncertainties is defined by the envelope of variations resulting from changing the renormalization and factorization scales by factors of 2 with an additional constraint of $0.5 \leq \mu_r/\mu_f \leq 2$. In most differential bins the effect was found to be smaller than the corresponding difference between Sherpa and MadGraph5_aMC@NLO. Lastly, the uncertainties in the $D^+ \rightarrow K^- \pi^+ \pi^+$ and $D^{*+} \rightarrow D^0 \pi^+ \rightarrow (K^- \pi^+) \pi^+$ branching ratios [112] are applied as uncertainties of 1.7% and 1.1%, respectively, in the signal yield in the likelihood fit.

Background MC modeling: The implementation of the background modeling uncertainties varies between the backgrounds. For $W + c^{\text{match}}$, $W + c^{\text{mismatch}}$, and $W + \text{jets}$ backgrounds, Sherpa 2.2.11 QCD scale, PDF, and α_s variations are used. Among the three, the QCD scale uncertainty generally has the largest effect and leads to a 10%–30% uncertainty in the yield of the corresponding background process, depending on the differential bin. The uncertainty is constrained in the likelihood fit by the small statistical uncertainties in the tails of the invariant mass distributions in the D^+ and D^{*+} channels, reducing its impact on the observables. As in the case of the signal process, these uncertainties are correlated between the differential bins. An additional modeling uncertainty is included by taking the full difference between Sherpa and MadGraph5_aMC@NLO predicted background yields. To be conservative, this uncertainty is taken to be uncorrelated between the differential bins. This avoids the assumption that either of the simulations have an *a priori* perfect description of the shape of the differential variable [i.e. $p_T(D^{(*)})$ or $|\eta(\ell)|$], and provides more flexibility in the likelihood fit.

Internal event weight variations in the MadGraph5_aMC@NLO 2.3.3 $t\bar{t}$ simulation are used to determine the effect of the PDF uncertainty on the top-quark background. The uncertainty due to initial-state radiation is estimated by simultaneously varying the h_{damp} parameter and the μ_r and μ_f scales, and choosing the Var3c up and down variants of the A14 tune as described in Ref. [96]. The impact of final-state radiation is evaluated by halving and doubling the renormalization scale for emissions from the parton shower. Uncertainties in the $t\bar{t}$ ME calculation and PS are estimated by replacing the nominal $t\bar{t}$ prediction with two alternative simulations: POWHEG+Herwig 7.04 and MadGraph5_aMC@NLO+PYTHIA 8 and taking the full difference as a systematic uncertainty. For other small backgrounds ($Z + \text{jets}$ and diboson events) a conservative 20% uncertainty in their yields is used. Due to the high purity of the $W + D^{(*)}$ signal process in the $W + D^{(*)}$ SR selection, background modeling uncertainties are subdominant in the statistical analysis.

Charm hadronization: The $W + c^{\text{match}}$ and $W + c^{\text{mismatch}}$ backgrounds in the D^+ channel have large contributions from weakly decaying charmed mesons incorrectly

reconstructed as $D^+ \rightarrow K^- \pi^+ \pi^+$ [e.g. $D_s^\pm \rightarrow \phi \pi^\pm \rightarrow (K^+ K^-) \pi^\pm$ reconstructed as $D^+ \rightarrow K^- \pi^+ \pi^+$]. Two sources of associated systematic uncertainty are included: uncertainties in the charmed hadron production fractions and uncertainties in the charmed hadron branching ratios. Charmed hadron production fractions in the MC samples are reweighted to the world-average values as described in Sec. VII B. Following the procedure in Ref. [55], three eigenvector variations of the event weights are derived to describe the correlated experimental systematic uncertainties associated with the measurements of the charmed hadron production fractions. The uncertainty affects the relative background yield by up to 3% and also the shape of the background invariant mass distribution because the different charmed hadron species populate different ranges of the reconstructed D^+ invariant mass. The impact of the uncertainties in the charmed hadron branching ratios is estimated in a conservative way by generating SPG D^+ samples with all branching ratios shifted simultaneously in a correlated manner to cover the systematic uncertainties in charmed hadron decays reported in Ref. [112]. The relative change in the background yield and shape of the $W + c^{\text{match}}$ background with respect to the nominal SPG configuration is propagated to the Sherpa MC sample and implemented in the statistical analysis. The size of the uncertainty is up to 5%. Both sources of charmed hadronization uncertainty related to background processes were found to have a negligible impact on all observables.

Multijet estimation: The multijet background and its uncertainties are estimated in the Fake CR, as described in Sec. VII C and the corresponding systematic uncertainties are implemented as nuisance parameters in the likelihood fit. Due to the difficulty of estimating the multijet background in the $W + D^{(*)}$ SR selection, the relative uncertainties are large ($>50\%$). However, the multijet background is largely symmetric between OS and SS

regions and its relative size is reduced in the OS–SS subtraction. Despite the large relative uncertainty in the multijet yield, the impact on the measured observables is therefore negligible.

Finite size of MC samples: MC statistical uncertainties affect the measurement in several ways. The binomial uncertainties in the $W + D^{(*)}$ fiducial efficiencies calculated with the Sherpa MC samples are propagated into the likelihood fit via nuisance parameters affecting the yield of the signal sample. There is one parameter per nonzero element of the detector response matrix. The statistical uncertainty in the diagonal elements is less than 1%, while the uncertainty in the off-diagonal elements exceeds 10%. However, because the off-diagonal elements have small values compared to diagonal ones, the corresponding statistical uncertainty has a negligible impact on the results. Furthermore, statistical uncertainties associated with the bins of the invariant mass distributions are implemented as constrained “ γ ” parameters in the likelihood fit as explained in Sec. VIII. There is one such parameter per invariant mass bin and their impact on the observables is of the order of 1%.

A. Evaluation of the overall systematic uncertainty

The impact of each individual systematic uncertainty on the observables is calculated by performing two likelihood fits with the corresponding nuisance parameter (θ) fixed to its postfit one-standard-deviation bounds. The changes in the values of the normalization factors associated with the observables, relative to the unconditional likelihood fit, are then taken as the impact of the given systematic uncertainty on the observables. Several nuisance parameters are grouped together by summing their impact on the observables in quadrature. A summary of the dominant systematic uncertainties is given in Table VIII for inclusive cross

TABLE VIII. Summary of the main systematic uncertainties as percentages of the measured observable for $\sigma_{\text{fid}}^{\text{OS-SS}}(W^- + D^{(*)})$, $\sigma_{\text{fid}}^{\text{OS-SS}}(W^+ + D^{(*)})$, and R_c^\pm in the D^+ and D^{*+} channels. The individual groups of uncertainties are defined in the text.

Uncertainty (%)	D^+ channel			D^{*+} channel		
	$\sigma_{\text{fid}}^{\text{OS-SS}}(W^- + D^+)$	$\sigma_{\text{fid}}^{\text{OS-SS}}(W^+ + D^-)$	$R_c^\pm(D^+)$	$\sigma_{\text{fid}}^{\text{OS-SS}}(W^- + D^{*+})$	$\sigma_{\text{fid}}^{\text{OS-SS}}(W^+ + D^{*-})$	$R_c^\pm(D^{*+})$
SV reconstruction	3.0	2.9	0.5	2.3	2.3	0.4
Jets and E_T^{miss}	1.7	1.9	0.2	1.5	.5	0.4
Luminosity	0.8	0.8	0.0	0.8	0.8	0.0
Muon reconstruction	0.6	0.7	0.3	0.7	0.7	0.3
Electron reconstruction	0.2	0.2	0.0	0.2	0.2	0.0
Multijet background	0.2	0.2	0.1	0.1	0.1	0.1
Signal modeling	2.1	2.1	0.1	1.2	1.2	0.0
Signal branching ratio	1.6	1.6	0.0	1.1	1.1	0.0
Background modeling	1.1	1.2	0.3	1.3	1.3	0.5
Finite size of MC samples	1.2	1.2	1.1	1.4	1.4	1.3
Data statistical uncertainty	0.5	0.5	0.7	0.7	0.7	1.0
Total	4.6	4.6	1.4	3.7	3.7	1.7

sections and the cross-section ratio R_c^\pm . The table demonstrates that most of the systematic uncertainties are correlated between the positive and negative charge channels and therefore cancel out in the R_c^\pm calculation. The dominant uncertainties in R_c^\pm are the data and MC statistical uncertainties. Uncertainties in differential bins are summarized in Appendix A. Similar to the R_c^\pm calculation, uncertainties with no dependence on the differential variable cancel out in the normalized cross section. For example, the SV reconstruction efficiency uncertainties almost completely cancel out in normalized $|\eta(\ell)|$ cross sections because the $D^{(*)}$ SV reconstruction has no dependence on the lepton pseudorapidity. However, the

same uncertainties do not cancel out in the $p_T(D^{(*)})$ measurement because there is a strong dependence on $p_T(D^{(*)})$.

X. RESULTS AND COMPARISON WITH THEORETICAL PREDICTIONS

Postfit comparisons between the data and MC distributions for the D^+ and D^{*+} channels are shown in Fig. 5 separately for the W^- and W^+ channels. Most of the data points are within the resulting 1σ systematic uncertainty band. The $W + D^{(*)}$ SR postfit yields obtained with the likelihood fit are given in Tables IX and X. Yields are

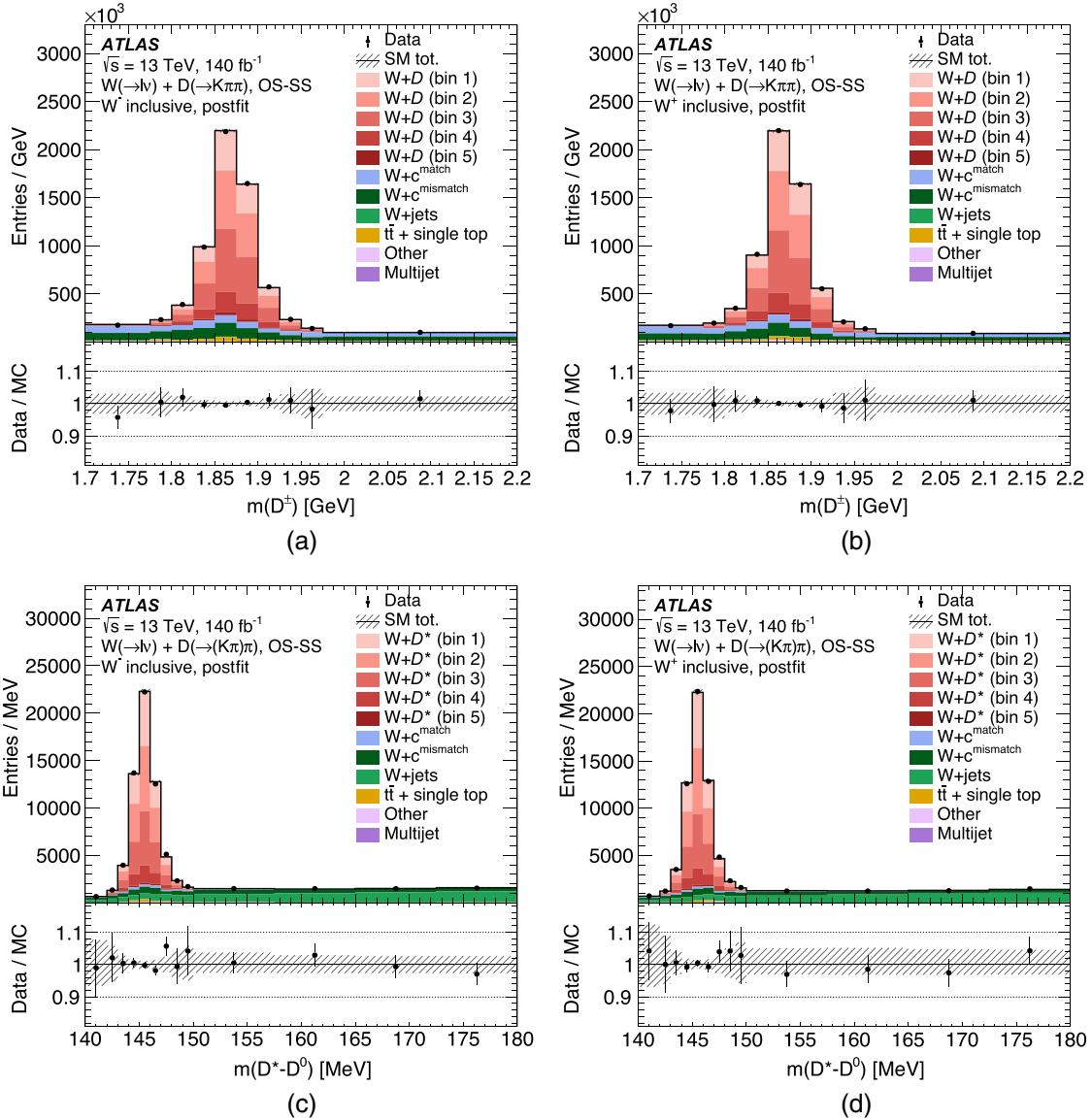


FIG. 5. Postfit OS-SS $W + D^{(*)}$ signal and background predictions compared with data: (a) $W^- + D^+$ channel, (b) $W^+ + D^-$ channel, (c) $W^- + D^{*+}$ channel, and (d) $W^+ + D^{*-}$ channel. The SM Tot. line represents the sum of all signal and background samples and the corresponding hatched band shows the full postfit systematic uncertainty. The five bins associated with the signal samples are the truth bins of the $p_T(D^{(*)})$ differential distribution.

TABLE IX. Postfit yields in the OS–SS $W + D^+$ SR from the $p_T(D^+)$ differential fit. The data statistical uncertainty is calculated as $\sqrt{N_{OS} + N_{SS}}$. Uncertainties in individual SM components are the full postfit systematic uncertainties.

Sample	OS–SS $W + D^+$ SR [$p_T(D^+)$ fit]		OS–SS $W + D^+$ SR ($ \eta(\ell) $ fit)	
	$W^- + D^+$	$W^+ + D^-$	$W^- + D^+$	$W^+ + D^-$
$W^\pm + D^\mp$ (bin 1)	$26\,430 \pm 510$	$26\,180 \pm 550$	$31\,530 \pm 530$	$30\,920 \pm 560$
$W^\pm + D^\mp$ (bin 2)	$39\,090 \pm 660$	$38\,610 \pm 660$	$30\,560 \pm 650$	$30\,790 \pm 620$
$W^\pm + D^\mp$ (bin 3)	$43\,520 \pm 660$	$41\,510 \pm 670$	$25\,640 \pm 470$	$24\,940 \pm 450$
$W^\pm + D^\mp$ (bin 4)	$15\,330 \pm 350$	$14\,520 \pm 350$	$23\,890 \pm 450$	$22\,380 \pm 500$
$W^\pm + D^\mp$ (bin 5)	$2\,740 \pm 120$	$2\,346 \pm 93$	$15\,860 \pm 480$	$14\,630 \pm 470$
$W + c^{\text{match}}$	$24\,800 \pm 2400$	$24\,300 \pm 2400$	$23\,500 \pm 2600$	$22\,800 \pm 2700$
$W + c^{\text{mismatch}}$	$34\,300 \pm 2500$	$29\,700 \pm 2400$	$33\,900 \pm 2500$	$29\,200 \pm 2500$
$W + \text{jets}$	$1\,300 \pm 1400$	$1\,900 \pm 1500$	$2\,200 \pm 1500$	$2\,500 \pm 1800$
$\bar{t}\bar{t} + \text{single top}$	$6\,500 \pm 550$	$6\,220 \pm 590$	$6\,520 \pm 540$	$6\,160 \pm 590$
Other	$1\,030 \pm 430$	$1\,830 \pm 460$	$1\,060 \pm 450$	$1\,940 \pm 470$
Multijet	730 ± 410	$1\,070 \pm 450$	$1\,180 \pm 640$	$1\,600 \pm 690$
Total SM	$195\,800 \pm 1200$	$188\,200 \pm 1300$	$195\,800 \pm 1300$	$187\,900 \pm 1400$
Data	$195\,800 \pm 1100$	$188\,200 \pm 1100$	$195\,800 \pm 1100$	$188\,200 \pm 1100$

TABLE X. Postfit yields in the OS–SS $W + D^{*+}$ SR from the $p_T(D^{*+})$ differential fit. The data statistical uncertainty is calculated as $\sqrt{N_{OS} + N_{SS}}$. Uncertainties in individual SM components are the full postfit systematic uncertainties.

Sample	OS–SS $W + D^{*+}$ SR [$p_T(D^{*+})$ fit]		OS–SS $W + D^{*+}$ SR ($ \eta(\ell) $ fit)	
	$W^- + D^{*+}$	$W^+ + D^{*-}$	$W^- + D^{*+}$	$W^+ + D^{*-}$
$W^\pm + D^{*\mp}$ (bin 1)	$13\,670 \pm 280$	$13\,880 \pm 260$	$12\,640 \pm 260$	$12\,980 \pm 230$
$W^\pm + D^{*\mp}$ (bin 2)	$17\,210 \pm 250$	$16\,950 \pm 280$	$12\,470 \pm 260$	$12\,910 \pm 280$
$W^\pm + D^{*\mp}$ (bin 3)	$15\,000 \pm 200$	$14\,890 \pm 200$	$10\,370 \pm 220$	$10\,250 \pm 200$
$W^\pm + D^{*\mp}$ (bin 4)	$5\,402 \pm 89$	$5\,139 \pm 95$	$9\,500 \pm 230$	$9\,120 \pm 240$
$W^\pm + D^{*\mp}$ (bin 5)	822 ± 45	744 ± 41	$6\,900 \pm 290$	$6\,390 \pm 290$
$W + c^{\text{match}}$	$2\,800 \pm 530$	$2\,730 \pm 530$	$3\,060 \pm 450$	$2\,690 \pm 480$
$W + c^{\text{mismatch}}$	$15\,900 \pm 1700$	$14\,000 \pm 1600$	$16\,400 \pm 1400$	$14\,200 \pm 1400$
$W + \text{jets}$	$35\,600 \pm 1800$	$32\,000 \pm 1700$	$35\,600 \pm 1800$	$31\,900 \pm 1700$
$\bar{t}\bar{t} + \text{single top}$	$1\,580 \pm 200$	$1\,320 \pm 180$	$1\,480 \pm 180$	$1\,350 \pm 160$
Other	$1\,710 \pm 540$	650 ± 480	$1\,480 \pm 480$	510 ± 420
Multijet	-90 ± 190	-20 ± 200	-160 ± 220	-120 ± 240
Total SM	$109\,600 \pm 1100$	$102\,200 \pm 1500$	$109\,700 \pm 1000$	$102\,200 \pm 1000$
Data	$109\,690 \pm 900$	$102\,320 \pm 970$	$109\,690 \pm 900$	$102\,320 \pm 970$

TABLE XI. Measured fiducial cross sections times the single-lepton-flavor W boson branching ratio and the cross-section ratios. $R_c^\pm(D^{(*)})$ is obtained by combining the individual measurements of $R_c^\pm(D^+)$ and $R_c^\pm(D^{*+})$ as explained in the text.

Channel	$\sigma_{\text{fid}}^{\text{OS-SS}}(W + D^{(*)}) \times B(W \rightarrow \ell\nu)$ (pb)
$W^- + D^+$	$50.2 \pm 0.2(\text{stat})^{+2.4}_{-2.3}(\text{syst})$
$W^+ + D^-$	$48.5 \pm 0.2(\text{stat})^{+2.3}_{-2.2}(\text{syst})$
$W^- + D^{*+}$	$51.1 \pm 0.4(\text{stat})^{+1.9}_{-1.8}(\text{syst})$
$W^+ + D^{*-}$	$50.0 \pm 0.4(\text{stat})^{+1.9}_{-1.8}(\text{syst})$
	$R_c^\pm = \sigma_{\text{fid}}^{\text{OS-SS}}(W^+ + D^{(*)}) / \sigma_{\text{fid}}^{\text{OS-SS}}(W^- + D^{(*)})$
$R_c^\pm(D^+)$	$0.965 \pm 0.007(\text{stat}) \pm 0.012(\text{syst})$
$R_c^\pm(D^{*+})$	$0.980 \pm 0.010(\text{stat}) \pm 0.013(\text{syst})$
$R_c^\pm(D^{(*)})$	$0.971 \pm 0.006(\text{stat}) \pm 0.011(\text{syst})$

shown for both the $p_T(D^{(*)})$ and $|\eta(\ell)|$ fits. Background yields and the integrated signal yields are consistent between the two fits in both the D^+ and D^{*+} channels. The systematic uncertainties in the integrated yields are slightly lower in the $p_T(D^{(*)})$ fits than in the $|\eta(\ell)|$ fits because the dominant systematic uncertainties depend more strongly on $p_T(D^{(*)})$ and are therefore more constrained in the fit.

The resulting cross sections $\sigma_{\text{fid}}^{\text{OS-SS}}(W + D^{(*)}) \times B(W \rightarrow \ell\nu)$ and R_c^\pm are presented in Table XI. The results presented here are obtained using the $p_T(D^{(*)})$ fit; results from the differential $|\eta(\ell)|$ fit are compatible. Ratios of cross sections obtained in the D^+ and D^{*+} channels are consistent with predictions obtained using the world-average production fractions, $\sigma(W + D^{*+}) / \sigma(W + D^+) = 1.01 \pm 0.034$, where

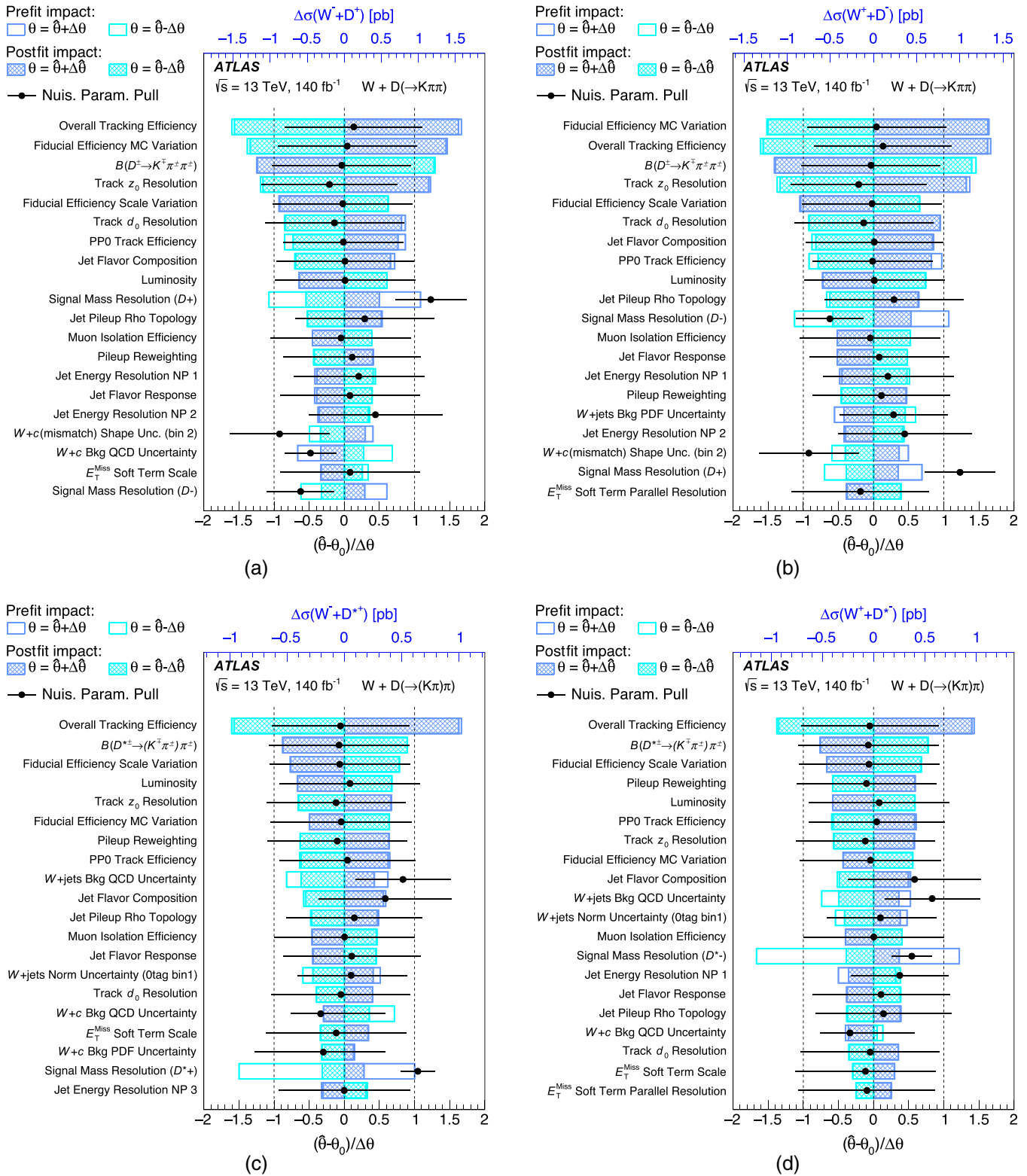


FIG. 6. Impact of systematic uncertainties, for the 20 largest contributions, on the fitted cross section from the $p_T(D^{(*)})$ fits, sorted in decreasing order. Impact on (a) $\sigma_{\text{fid}}^{\text{OS-SS}}(W^- + D^+)$, (b) $\sigma_{\text{fid}}^{\text{OS-SS}}(W^+ + D^-)$, (c) $\sigma_{\text{fid}}^{\text{OS-SS}}(W^- + D^{*+})$, and (d) $\sigma_{\text{fid}}^{\text{OS-SS}}(W^+ + D^{*-})$. The impact of prefit (postfit) nuisance parameters $\vec{\theta}$ on the signal strength are shown with empty (colored) boxes. The postfit central value ($\hat{\theta}$) and uncertainty are shown for each parameter with black dots.

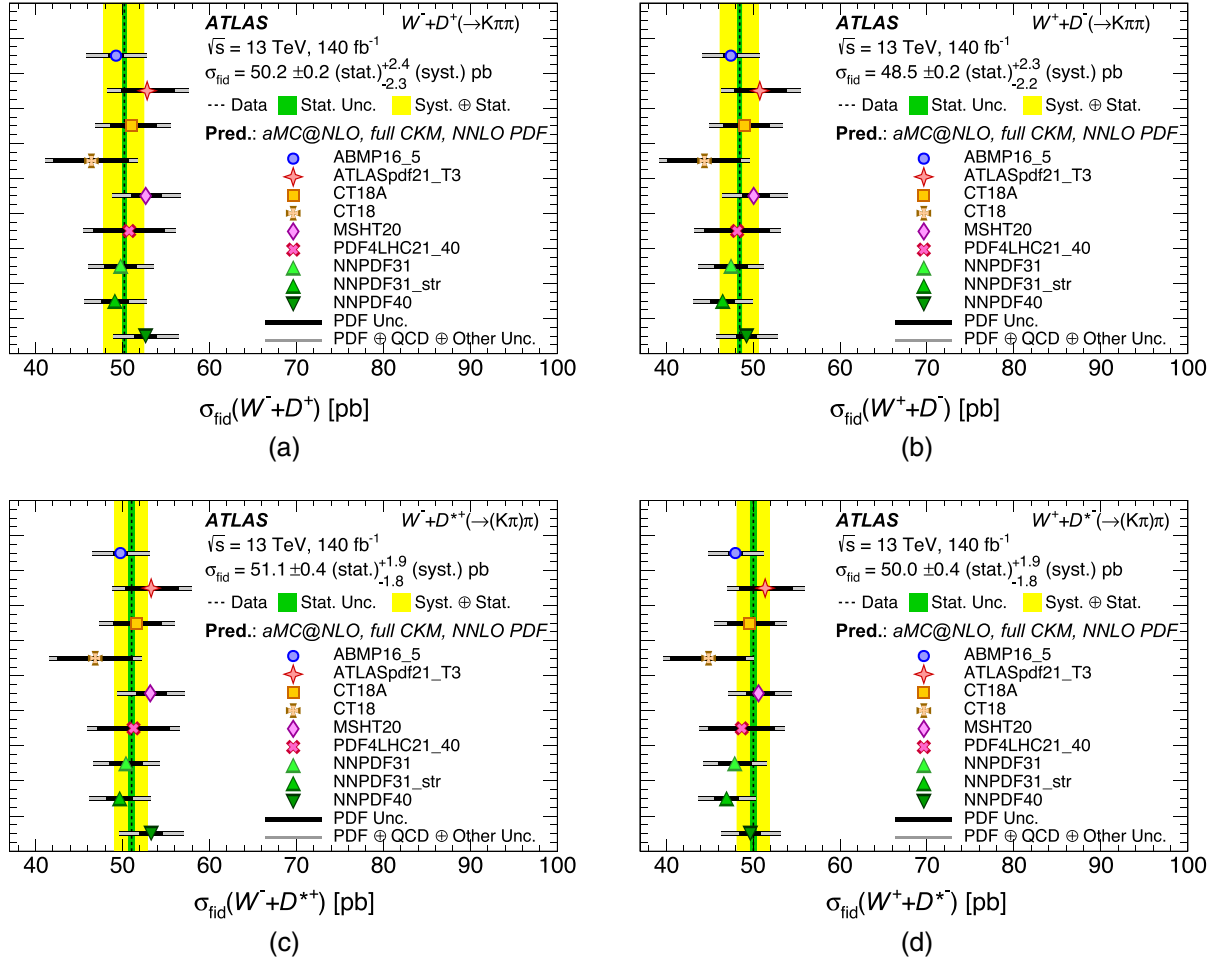


FIG. 7. Measured fiducial cross section times the single-lepton-flavor W branching ratio compared with different NNLO PDF predictions for (a) $W^- + D^+$, (b) $W^+ + D^-$, (c) $W^- + D^{*+}$, and (d) $W^+ + D^{*-}$. The dotted vertical line shows the central value of the measurement, the green band shows the statistical uncertainty, and the yellow band shows the combined statistical and systematic uncertainty. The PDF predictions are designated by markers. The inner error bars on the theoretical predictions show the 68% CL uncertainties obtained from the error sets provided with each PDF set, while the outer error bar represents the quadrature sum of the 68% CL PDF, scale, hadronization, and matching uncertainties. The PDF predictions are based on NLO calculations performed using $a\text{MC@NLO}$ and a full CKM matrix: ABMP16_5 [26], ATLASpdf21_T3 [9], CT18A, CT18 [27], MSHT20 [28], PDF4LHC21_40 [29], NNPDF31 [30], NNPDF31_str [12], NNPDF40 [31]. ABMP16_5, ATLASpdf21_T3, CT18A, and CT18 impose symmetric strange-sea PDFs.

the 3.4% uncertainty is obtained using the (correlated) uncertainties in the D^* and D^+ production fractions [54]. The measured differential cross sections in bins of $p_T(D^{(*)})$ and $|\eta(\ell)|$ are given in Appendix B. The statistical uncertainty is larger in the D^{*+} channel because the branching ratio for that mode is smaller than the one for D^+ ; the relative sizes of the systematic uncertainties are similar because they are largely independent of the channel. A combined value of $R_c^\pm(D^{(*)})$ is derived from the individual measurements of $R_c^\pm(D^+)$ and $R_c^\pm(D^{*+})$. Systematic uncertainties are largely uncorrelated between the channels. As shown in Table VIII, they are dominated by the uncorrelated MC statistical uncertainties. After correcting for differences between the chosen fiducial regions, these measurements are

consistent with, but more precise than, the CMS $W + D^{*+}$ results presented in Ref. [23], performed with 35.7 fb^{-1} of data.

The impact of the nuisance parameters on the fitted values of the absolute fiducial cross section in the differential $p_T(D^{(*)})$ fits is shown as a “ranking plot” in Fig. 6. The 20 nuisance parameters with the largest contribution are ordered by decreasing impact on the corresponding observable. The postfit central values and uncertainties of the corresponding parameters are given in the same plots. The ranking plots demonstrate that most nuisance parameters with large impact on the integrated fiducial cross section do not deviate significantly from the initial values in the likelihood fit. The parameters associated with the signal

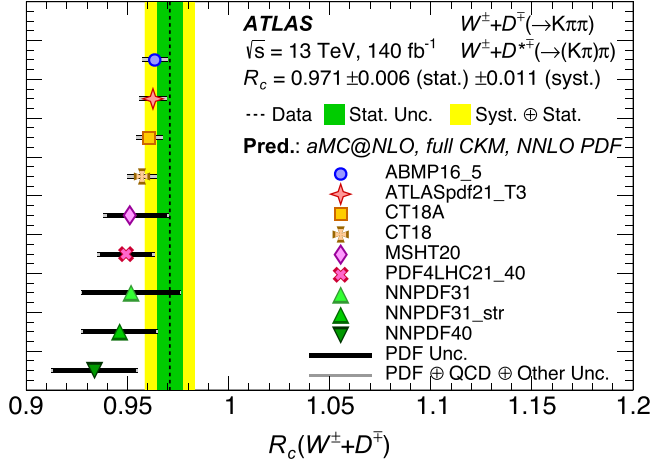


FIG. 8. Measured fiducial cross-section ratio, R_c^\pm , compared with different PDF predictions. The data are a combination of the separate $W + D^+$ and $W + D^{*+}$ channel measurements. The dotted vertical line shows the central value of the measurement, the green band shows the statistical uncertainty, and the yellow band shows the combined statistical and systematic uncertainty. The PDF predictions are designated by markers. The inner error bars on the theoretical predictions show the 68% CL uncertainties obtained from the error sets provided with each PDF set, while the outer error bar represents the quadrature sum of the 68% CL PDF, scale, hadronization, and matching uncertainties. The PDF predictions are based on NLO calculations performed using $a_{MC@NLO}$ and a full CKM matrix: ABMP16_5 [26], ATLASpdf21_T3 [9], CT18A, CT18 [27], MSHT20 [28], PDF4LHC21_40 [29], NNPDF31 [30], NNPDF31_str [12], NNPDF40 [31]. ABMP16_5, ATLASpdf21_T3, CT18A, and CT18 impose symmetric strange-sea PDFs.

mass-peak shape uncertainties have the most significant pulls in the fit; however, the impact of the corresponding systematic uncertainties on the observables is small (up to 1% for cross sections and negligible for R_c^\pm). These parameters are constrained by the observed width of the $D^{(*)}$ peaks in the data. The NP shifts depend on the charge of the $D^{(*)}$ meson and are therefore treated with independent parameters for each charge. They account for the small residual resolution degradation that is not accounted for in the MC simulation.

Theoretical predictions of the $W + D^{(*)}$ cross section for a variety of state-of-the-art PDF sets are obtained using the signal $a_{MC@NLO+Py8}$ (NLO) samples with the configuration described in Sec. III B 1. A finite charm quark mass of $m_c = 1.55$ GeV is used to regularize the cross section and a full CKM matrix is used to calculate the hard-scattering amplitudes. For each PDF set, the uncertainty is obtained from the alternative generator weights using the LHAPDF prescription [120]. Uncertainties due to the choice of PYTHIA 8 tune are assessed by replacing the A14 tune with the Monash tune [121]. Uncertainties associated with the choice of parton-shower model are estimated from a comparison of events generated with the baseline

configuration and events generated with Herwig 7.2 [122] using its default tune. Differences between predictions associated with the choice of NLO matching algorithm are assessed by comparing the $a_{MC@NLO+Py8}$ (NLO) cross sections with those obtained using the calculation described in Ref. [36]. This calculation is based on the Powheg event generator, which uses the POWHEG BOX v2 interface to implement POWHEG NLO matching. A charm quark mass $m_c = 1.5$ GeV is used to regularize the cross section. Effects of nondiagonal CKM matrix elements and off-shell W boson decays including spin correlations are taken into account in both the $a_{MC@NLO+Py8}$ (NLO) and Powheg calculations. For these comparisons, the renormalization and factorization scales are set to one half of the transverse mass calculated using all final-state partons and leptons, and the ABMP16_3_NLO PDF set with $\alpha_s = 0.118$ and Monash PYTHIA 8.2 tune are used for both samples. The uncertainty in the direct charm production fractions is assessed using the results from Ref. [54].

Figure 7 shows the measured fiducial cross sections for each of the four channels compared with the theoretical predictions obtained using different NNLO PDF sets, including a PDF set tailored to describe the strangeness of the proton—NNPDF3.1_strange [12]. Results for all four channels show a consistent pattern. The experimental precision is comparable to the PDF uncertainties and smaller than the total NLO theory uncertainty. All PDF sets are consistent with the measured cross sections once the combined theory and PDF set uncertainties are considered.

The cross-section ratio, R_c^\pm , is shown for the combined D^+ and D^{*+} channel measurements in Fig. 8. This combined result is consistent with theoretical predictions for all PDF sets, although the prediction obtained using NNPDF4.0NNLO shows some tension with the measurement. Unlike the cross-section measurements, which are dominated by systematic uncertainties, the measurements of R_c^\pm have comparable statistical and systematic uncertainties. PDF set uncertainties for R_c^\pm fall into two categories. Those sets that impose the restriction that the strange-sea be symmetric ($s = \bar{s}$), such as CT18 and AMBP16, predict R_c^\pm with high precision while PDF fits that allow the s and \bar{s} distributions to differ, such as NNPDF or MSHT, have larger uncertainties. These measurements are consistent with the predictions obtained with PDF sets that impose a symmetric s - \bar{s} sea, suggesting that any s - \bar{s} asymmetry is small in the Bjorken- x region probed by this measurement. Reference [15] presents a detailed study of the NLO and NNLO fiducial cross sections for different charm-jet selections. That study uses the same lepton fiducial definition as this paper. While $W + c$ -jet cross-section calculations cannot be compared with $\sigma_{fid}^{OS-SS}(W + D^{(*)})$ measurements, they provide insight into the behavior of R_c^\pm . The $W + c$ -jet R_c^\pm value calculated at NLO using an OS-SS selection is consistent within statistical uncertainties with that obtained

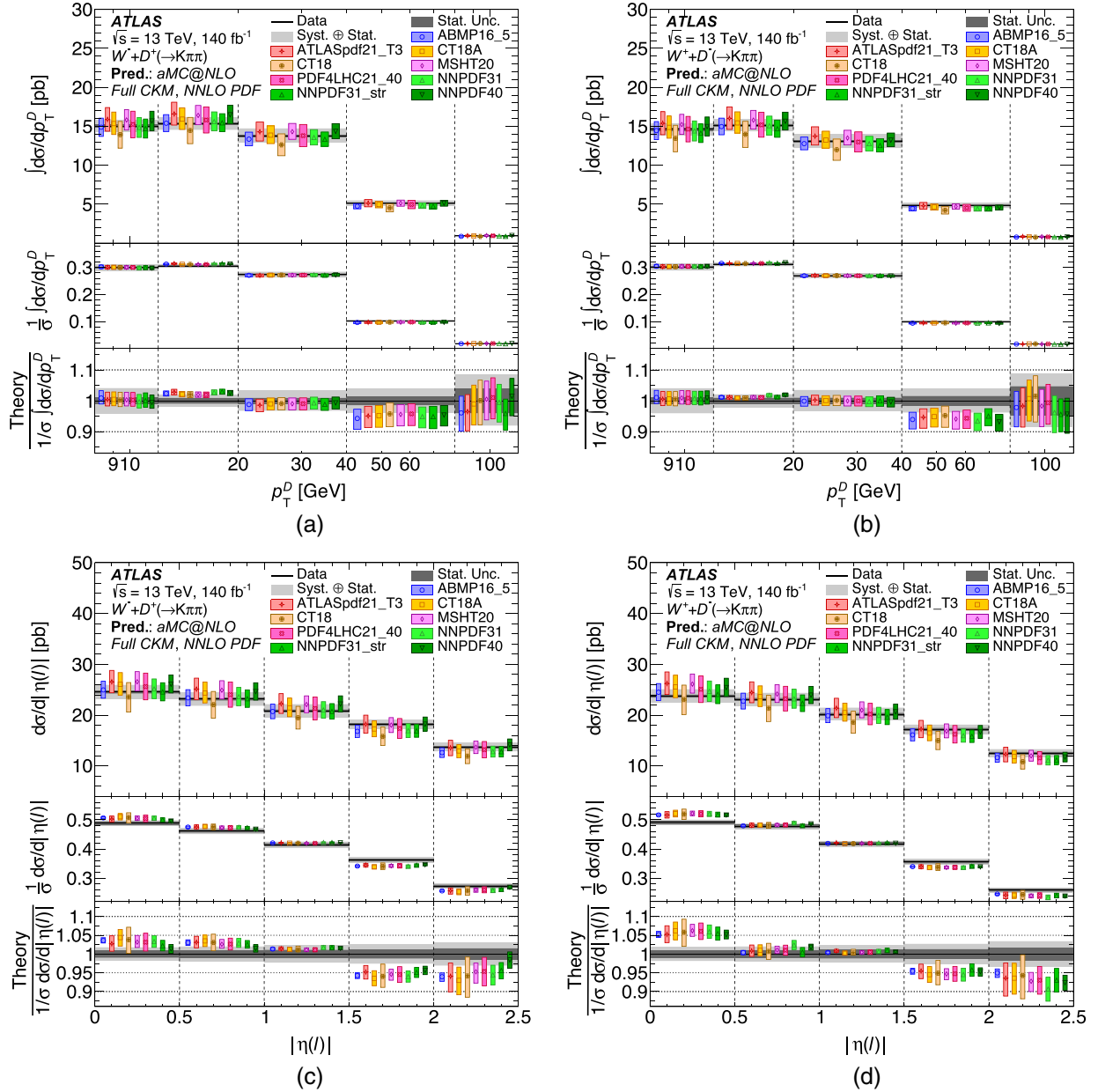


FIG. 9. Measured differential fiducial cross section times the single-lepton-flavor W branching ratio compared with different NNLO PDF predictions in the D^+ channel: (a) $W^- + D^+$ $p_T(D^+)$, (b) $W^+ + D^-$ $p_T(D^+)$, (c) $W^- + D^+$ $|\eta(\ell)|$, and (d) $W^+ + D^-$ $|\eta(\ell)|$. The displayed cross sections in $p_T(D^+)$ plots are integrated over each differential bin. Error bars on the MC predictions are the quadrature sum of the QCD scale uncertainty, PDF uncertainties, hadronization uncertainties, and matching uncertainty. The PDF predictions are based on NLO calculations performed using aMC@NLO and a full CKM matrix: ABMP16_5 [26], ATLASpdf21_T3 [9], CT18A, CT18 [27], MSHT20 [28], PDF4LHC21_40 [29], NNPDF31 [30], NNPDF31_str [12], NNPDF40 [31]. ABMP16_5, ATLASpdf21_T3, CT18A, and CT18 impose symmetric strange-sea PDFs.

for $W + D^{(*)}$ using MadGraph5_aMC@NLO and the same PDF set (NNPDF3.1). The NNLO+EW(NLO) value of the $W + c$ -jet R_c^\pm is smaller than the NLO value by $\sim 1\%$, but the two are consistent within the quoted 1% statistical uncertainty. The effects of NNLO scale uncertainties on R_c^\pm are below 0.3%. These results suggest that the PDF comparisons presented in Fig. 8 are likely to look similar for a NNLO+EW(NLO) calculation.

The differential cross sections are shown in Figs. 9 and 10, together with the predicted cross sections obtained with different choices of NNLO PDF set. The patterns observed in the D^+ and D^{*+} channels are consistent for both the differential $D^{(*)}$ p_T and $|\eta(\ell)|$ distributions. For each $D^{(*)}$ species and charge, the differential distributions are plotted in three separate panels. The top panel compares the measured differential cross section with theoretical

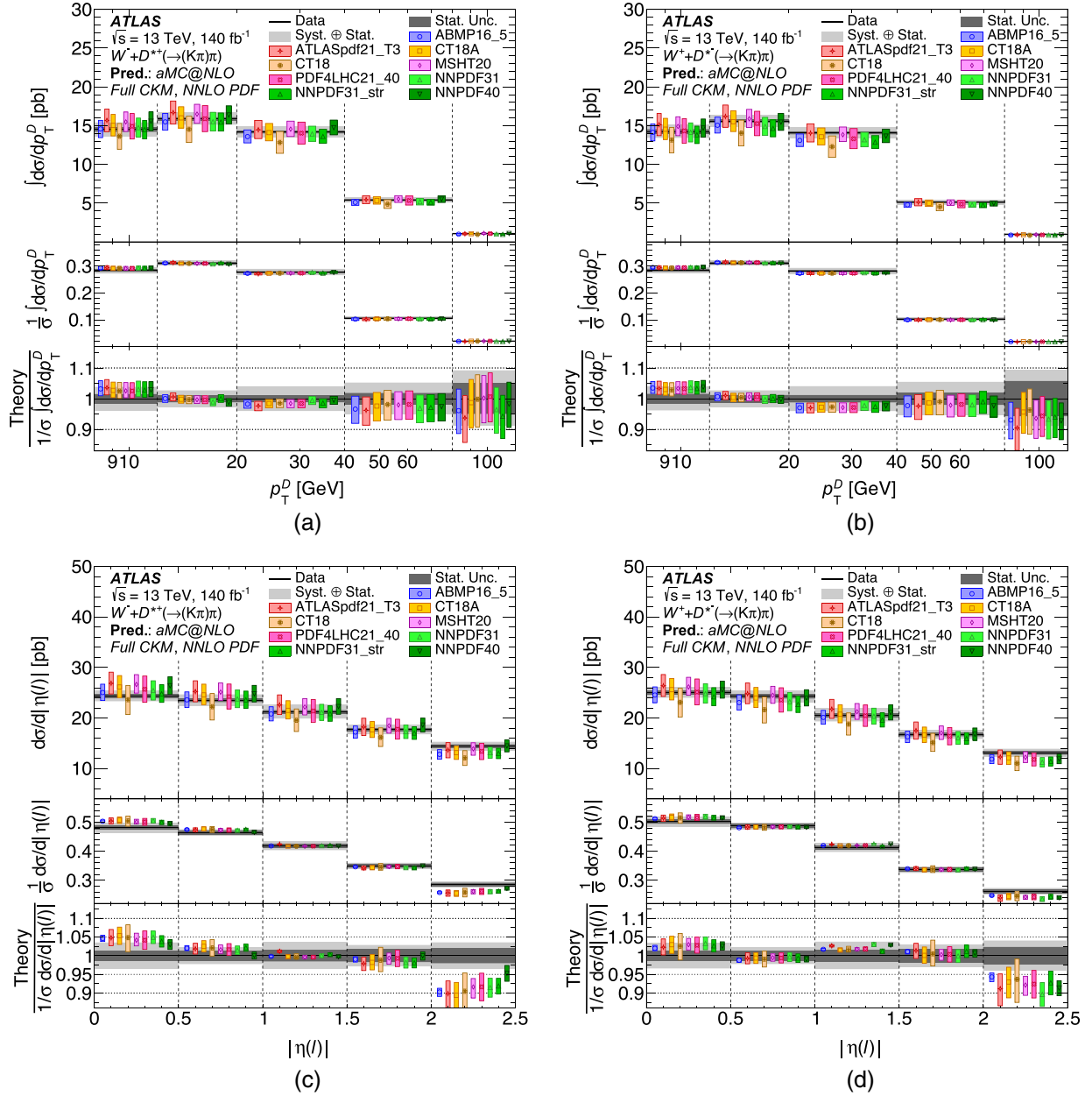


FIG. 10. Measured differential fiducial cross section times the single-lepton-flavor W branching ratio compared with different PDF predictions in the D^{*+} channel: (a) $W^- + D^{*+} p_T(D^{*+})$, (b) $W^+ + D^{*-} p_T(D^{*+})$, (c) $W^- + D^{*+} |\eta(\ell)|$, and (d) $W^+ + D^{*-} |\eta(\ell)|$. The displayed cross sections in $p_T(D^+)$ plots are integrated over each differential bin. Error bars on the MC predictions are the quadrature sum of the QCD scale uncertainty, PDF uncertainties, hadronization uncertainties, and matching uncertainty. The PDF predictions are based on NLO calculations performed using aMC@NLO and a full CKM matrix: ABMP16_5 [26], ATLASpdf21_T3 [9], CT18A, CT18 [27], MSHT20 [28], PDF4LHC21_40 [29], NNPDF31 [30], NNPDF31_str [12], NNPDF40 [31]. ABMP16_5, ATLASpdf21_T3, CT18A, and CT18 impose symmetric strange-sea PDFs.

predictions obtained using the same PDF sets as in Fig. 7. Systematic uncertainties in the predictions are correlated between bins and are dominated by uncertainties in the normalization. Differences between PDF sets can be seen more clearly in the middle and lower panels, which show the normalized differential cross sections and the ratio of the predictions to the normalized cross sections, respectively. Because the integral of the normalized cross section across

all bins is constrained to be unity, the measurements are highly correlated between bins: If the normalized cross section in one bin increases, that in another bin must decrease.

Variations in the shape of the $p_T(D^{*})$ distribution depend only weakly on the choice of PDF. Experimental sensitivity to this dependence is reduced by the presence of p_T -dependent systematic uncertainties in the $D^{(*)}$ fiducial

TABLE XII. The p -values for compatibility of the measurement and the predictions, calculated with the χ^2 formula using experimental and theory covariance matrices. The first column shows the p -values for the $|\eta(\ell)|$ (D^+) differential cross section using only experimental uncertainties. The next columns show p -values when progressively more theory systematic uncertainties are included. The PDF predictions are based on NLO calculations performed using `amc@NLO` and a full CKM matrix: ABMP16_5 [26], ATLASpdf21_T3 [9], CT18A, CT18 [27], MSHT20 [28], PDF4LHC21_40 [29], NNPDF31 [30], NNPDF31_str [12], NNPDF40 [31]. ABMP16_5, ATLASpdf21_T3, CT18A, and CT18 impose symmetric strange-sea PDFs.

Channel	$D^+ \eta(\ell) $				
	p -value for PDF (%)	Experimental only	\oplus QCD scale	\oplus Hadronization and matching	\oplus PDF
ABMP16_5_nnlo		7.1	11.8	12.9	19.8
ATLASpdf21_T3		9.0	9.7	11.5	84.7
CT18ANNLO		0.7	1.0	1.1	76.0
CT18NNLO		1.4	6.1	6.3	87.6
MSHT20nnlo_as118		2.7	2.9	3.3	45.6
PDF4LHC21_40		3.9	5.3	5.6	75.8
NNPDF31_nnlo_as_0118_hessian		1.5	2.6	2.8	50.7
NNPDF31_nnlo_as_0118_strange		9.1	14.7	15.2	59.9
NNPDF40_nnlo_as_01180_hessian		9.9	10.2	10.2	43.7

efficiency. Thus, while measurements of the cross section as a function of $p_T(D^{(*)})$ are an important test of the quality of MC modeling, they do not provide incisive constraints on PDFs. Systematic uncertainties for $|\eta(\ell)|$ are small and highly correlated among bins, providing good sensitivity to PDF variations. Measured differential cross sections have a broader $|\eta(\ell)|$ distribution than the central values of the predictions obtained with any of the PDF sets. The significance of the discrepancy is reduced if the PDF uncertainties are considered.

The compatibility of the measurements and predictions is tested with a χ^2 formula using experimental and theory covariance matrices,

$$\chi^2 = \sum_{i,j} (x_i - \mu_i)(C^{-1})_{ij}(x_j - \mu_j),$$

where \vec{x} are the measured differential cross sections in the ten $|\eta(\ell)|$ bins, and $\vec{\mu}$ are the predicted cross sections in the same bin and depend on the choice of PDF set. The total covariance matrix C is the sum of the experimental covariance matrix, encoding the measurement error, and the theory covariance matrix describing the uncertainties in the theory predictions as described below. The χ^2 is then converted to a p -value assuming 10 degrees of freedom. Experimental covariance matrices are given in Appendix C. The theory covariance matrix corresponding to the PDF uncertainty is calculated following the LHAPDF prescription [120]. Other theory uncertainties are assumed to be 100% correlated across differential bins.

The resulting p -values for the `amc@NLO` predictions of the $|\eta(\ell)|$ differential cross sections with different PDF sets are given in Table XII for the D^+ channel and in Table XIII

TABLE XIII. The p -values for compatibility of the measurement and the predictions, calculated with the χ^2 formula using experimental and theory covariance matrices. The first column shows the p -values for the $|\eta(\ell)|$ (D^{*+}) differential cross section using only experimental uncertainties. The next columns show p -values when progressively more theory systematic uncertainties are included. The PDF predictions are based on NLO calculations performed using `amc@NLO` and a full CKM matrix: ABMP16_5 [26], ATLASpdf21_T3 [9], CT18A, CT18 [27], MSHT20 [28], PDF4LHC21_40 [29], NNPDF31 [30], NNPDF31_str [12], NNPDF40 [31]. ABMP16_5, ATLASpdf21_T3, CT18A, and CT18 impose symmetric strange-sea PDFs.

Channel	$D^{*+} \eta(\ell) $				
	p -value for PDF (%)	Experimental only	\oplus QCD scale	\oplus Hadronization and matching	\oplus PDF
ABMP16_5_nnlo		22.8	23.7	25.0	28.8
ATLASpdf21_T3		1.9	2.9	3.4	33.7
CT18ANNLO		6.5	6.9	7.8	47.3
CT18NNLO		9.4	19.2	19.7	52.8
MSHT20nnlo_as118		7.0	9.4	10.4	31.3
PDF4LHC21_40		14.2	14.2	15.2	51.4
NNPDF31_nnlo_as_0118_hessian		5.0	5.1	5.5	34.9
NNPDF31_nnlo_as_0118_strange		11.4	12.4	13.2	46.0
NNPDF40_nnlo_as_01180_hessian		4.5	6.1	6.4	36.0

for the D^{*+} channel. The p -values are calculated with progressively more systematic uncertainties included in the theory covariance matrix, ranging from an “Exp. Only” calculation, where no systematic uncertainties related to the theory predictions are included, to a calculation including all theory uncertainties: QCD scale, “hadronization and matching,” and PDF uncertainties. The hadronization and matching uncertainty is defined to be the quadrature sum of the uncertainty in the charm production fractions, two-point uncertainties associated with the choice of showering program (PYTHIA vs Herwig), the tune (A14 vs Monash), and the matching algorithm (amc@NLO vs POWHEG). These uncertainties are treated as fully correlated between the $W^+ + D^-$ and $W^- + D^+$ channels. Without considering the theory uncertainties (i.e. just comparing the PDF central values with the experimental measurements) the p -values are below 10% for all PDFs in the D^+ channel and most of the PDFs in the D^{*+} channel. Adding hadronization and QCD scale uncertainties increases the probabilities to at most 15% in the D^+ channel and 25% in the D^{*+} channel. Although the QCD scale uncertainty is a large uncertainty in the absolute cross section, it does not change the p -values significantly because the uncertainty is 100% correlated between the $|\eta(\ell)|$ bins, and it does not have a large impact on the shape of the differential distribution. Adding the PDF uncertainties greatly increases the p -values; the PDF uncertainty has a significant effect on the shape of the differential $|\eta(\ell)|$ distribution. This suggests that including these measurements in a global PDF fit would provide useful constraints on the allowed PDF variations.

XI. CONCLUSIONS

Fiducial cross sections for W boson production in association with a $D^{(*)}$ meson are measured as a function of $p_T(D^{(*)})$ and $|\eta(\ell)|$ using 140.1 fb^{-1} of $\sqrt{s} = 13 \text{ TeV}$ pp collision data at collected with the ATLAS detector at the Large Hadron Collider. A secondary-vertex fit is used to tag events containing a D^+ or a D^{*+} meson and a profile likelihood fit is used to extract the $W + D^{(*)}$ observables. The single-lepton-species integrated cross sections and cross-section ratios for the fiducial region $p_T(\ell) > 30 \text{ GeV}$, $|\eta(\ell)| < 2.5$, $p_T(D^{(*)}) > 8 \text{ GeV}$, and $|\eta(D^{(*)})| < 2.2$ are measured to be

$$\begin{aligned}\sigma_{\text{fid}}^{\text{OS-SS}}(W^- + D^+) &= 50.2 \pm 0.2(\text{stat})_{-2.3}^{+2.4}(\text{syst}) \text{ pb}, \\ \sigma_{\text{fid}}^{\text{OS-SS}}(W^+ + D^-) &= 48.5 \pm 0.2(\text{stat})_{-2.2}^{+2.3}(\text{syst}) \text{ pb}, \\ \sigma_{\text{fid}}^{\text{OS-SS}}(W^- + D^{*+}) &= 51.1 \pm 0.4(\text{stat})_{-1.8}^{+1.9}(\text{syst}) \text{ pb}, \\ \sigma_{\text{fid}}^{\text{OS-SS}}(W^+ + D^{*-}) &= 50.0 \pm 0.4(\text{stat})_{-1.8}^{+1.9}(\text{syst}) \text{ pb}, \\ R_c^\pm(D^{(*)}) &= 0.971 \pm 0.006(\text{stat}) \pm 0.011(\text{syst}).\end{aligned}$$

The uncertainty in the measured absolute integrated and differential fiducial cross sections is about 5% and is dominated by the systematic uncertainty. On the other hand, cross-section ratios and normalized differential cross sections are measured with percent-level precision and have comparable contributions from systematic and statistical uncertainties. The experimental precision of these measurements is comparable to the PDF uncertainties and smaller than the total theory uncertainty.

Measured differential cross sections as a function of $|\eta(\ell)|$ have a broader distribution than the central values of the predictions. These measurements are, however, consistent with the predictions if the uncertainties associated with the PDF sets are included, indicating that these measurements would provide useful constraints for global PDF fits. The measured values of R_c^\pm are consistent with predictions obtained with a range of PDF sets, including those that constrain the s - \bar{s} sea to be symmetric.

ACKNOWLEDGMENTS

We thank CERN for the very successful operation of the LHC, as well as the support staff from our institutions without whom ATLAS could not be operated efficiently. We acknowledge the support of ANPCyT, Argentina; Yerevan Physics Institute (YerPhI), Armenia; ARC, Australia; BMWFW and FWF, Austria; ANAS, Azerbaijan; CNPq and FAPESP, Brazil; NSERC, NRC, and CFI, Canada; CERN; ANID, Chile; CAS, MOST, and NSFC, China; Minciencias, Colombia; MEYS CR, Czech Republic; DNRF and Danish Natural Science Research Council (DNSRC), Denmark; IN2P3-CNRS and Institut de recherche sur les lois fondamentales de l’Univers, Direction des Sciences de la Matière, Commissariat à l’Énergie Atomique (CEA-DRF/IRFU), France; Shota Rustaveli National Science Foundation of Georgia (SRNSFG), Georgia; BMBF, HGF, and MPG, Germany; General Secretariat for Research and Innovation (GSRI), Greece; RGC and Hong Kong SAR, China; ISF and Benoziyo Center, Israel; INFN, Italy; MEXT and JSPS, Japan; CNRST, Morocco; NWO, Netherlands; RCN, Norway; MEiN, Poland; FCT, Portugal; MNE/IFA, Romania; MESTD, Serbia; Ministry of Education, Science, Research and Sport (MSSR), Slovakia; ARRS and MIZŽ, Slovenia; DSI/NRF, South Africa; MICINN, Spain; Swedish Research Council (SRC) and Wallenberg Foundation, Sweden; SERI, SNSF, and Cantons of Bern and Geneva, Switzerland; MOST, Taiwan; TENMAK, Türkiye; STFC, United Kingdom; DOE and NSF, USA. In addition, individual groups and members have received support from BCKDF, CANARIE, Compute Canada and CRC, Canada; RIMUS Research Programme (PRIMUS 21/SCI/017) and The University Research Center (UNCE SCI/013), Czech Republic; COST, ERC, ERDF, Horizon 2020, and Marie Skłodowska-Curie Actions, European Union; Investissements d’Avenir Labex,

Investissements d’Avenir Idex, and ANR, France; DFG and AvH Foundation, Germany; Herakleitos, Thales, and Aristeia programs co-financed by EU-ESF and the National Strategic Reference Framework (Greek NSRF), Greece; BSF-NSF and MINERVA Foundation (MINERVA), Israel; Norwegian Financial Mechanism 2014–2021, Norway; NCN and NAWA, Poland; La Caixa Banking Foundation, CERCA Programme Generalitat de Catalunya, and PROMETEO and GenT Programmes Generalitat Valenciana (PROMETEO) and GenT Programmes Generalitat Valenciana, Spain; Göran Gustafssons Stiftelse, Sweden; The Royal Society and Leverhulme Trust, United Kingdom. The crucial computing support from all WLCG partners is acknowledged gratefully, in particular from CERN, the ATLAS Tier-1 facilities at TRIUMF (Canada), NDGF (Denmark, Norway, Sweden), CC-IN2P3 (France), KIT/GridKA (Germany), INFN-CNAF (Italy), NL-T1 (Netherlands), PIC (Spain), ASGC (Taiwan), RAL (United Kingdom), and BNL (USA), the Tier-2 facilities worldwide and large non-WLCG resource providers. Major contributors of computing resources are listed in Ref. [123].

APPENDIX A: BREAKDOWN OF SYSTEMATIC UNCERTAINTIES IN DIFFERENTIAL BINS

The breakdown of uncertainties in the measured differential fiducial cross sections is summarized in Tables XIV–XVII. The uncertainties in the normalized cross sections are given in parentheses next to the uncertainties in the corresponding absolute cross-sections.

TABLE XIV. Summary of the main systematic uncertainties as percentages of the measured observable for the $p_T(D^+)$ differential cross sections in the D^+ channel. The uncertainty in the corresponding normalized cross section is given in parentheses next to the uncertainty in the absolute differential cross section.

Uncertainty (%)	$d\sigma_{\text{fid}}^{\text{OS-SS}}(W^- + D^+)/d(p_T(D^+))$ ($1/\sigma d\sigma/dp_T$)					$d\sigma_{\text{fid}}^{\text{OS-SS}}(W^+ + D^-)/d(p_T(D^+))$ ($1/\sigma d\sigma/dp_T$)				
	$p_T(D^+)$ bins (GeV)	[8, 12]	[12, 20]	[20, 40]	[40, 80]	[80, ∞)	[8, 12]	[12, 20]	[20, 40]	[40, 80]
SV reconstruction	3.1 (1.2)	2.8 (0.6)	3.2 (0.7)	4.7 (2.6)	5.7 (4.3)	2.6 (1.0)	2.5 (0.7)	3.3 (0.7)	4.5 (2.5)	5.8 (3.9)
Jets and E_T^{miss}	1.8 (0.8)	1.9 (0.4)	1.9 (0.5)	2.0 (1.2)	3.4 (2.4)	2.1 (0.6)	1.9 (0.6)	2.1 (0.7)	2.0 (1.2)	3.7 (2.7)
Luminosity	0.8 (0.0)	0.8 (0.0)	0.8 (0.0)	0.8 (0.0)	0.8 (0.0)	0.8 (0.0)	0.8 (0.0)	0.8 (0.0)	0.8 (0.0)	0.8 (0.0)
Muon reconstruction	0.8 (0.2)	0.7 (0.1)	0.6 (0.1)	0.5 (0.3)	0.6 (0.5)	0.8 (0.2)	0.7 (0.1)	0.6 (0.1)	0.5 (0.3)	0.5 (0.4)
Electron reconstruction	0.2 (0.0)	0.2 (0.1)	0.3 (0.0)	0.4 (0.2)	0.5 (0.4)	0.2 (0.0)	0.2 (0.0)	0.2 (0.0)	0.4 (0.2)	0.5 (0.4)
Multijet background	0.3 (0.2)	0.3 (0.1)	0.2 (0.1)	0.1 (0.3)	1.1 (1.3)	0.1 (0.1)	0.3 (0.1)	0.2 (0.1)	0.2 (0.1)	0.1 (0.2)
Signal modeling	1.5 (3.2)	2.7 (0.7)	4.6 (2.7)	2.4 (0.4)	3.0 (1.2)	1.5 (3.2)	2.7 (0.7)	4.6 (2.7)	2.3 (0.4)	3.0 (1.1)
Signal branching ratio	1.7 (0.1)	1.6 (0.0)	1.5 (0.1)	1.6 (0.0)	1.7 (0.1)	1.7 (0.1)	1.6 (0.0)	1.5 (0.1)	1.6 (0.0)	1.7 (0.1)
Background modeling	1.7 (1.4)	1.5 (0.8)	1.8 (1.2)	1.8 (1.6)	1.8 (1.7)	1.9 (1.5)	1.6 (1.0)	1.8 (1.3)	1.6 (1.5)	3.5 (3.2)
Finite size of MC samples	2.3 (1.7)	1.7 (1.3)	1.6 (1.3)	2.1 (1.9)	4.6 (4.6)	2.4 (1.8)	1.7 (1.3)	1.7 (1.4)	2.1 (1.9)	4.8 (4.6)
Data statistical uncertainty	1.2 (1.0)	0.9 (0.8)	0.9 (0.9)	1.4 (1.4)	4.0 (4.0)	1.3 (1.1)	1.0 (0.9)	1.0 (0.9)	1.5 (1.5)	4.6 (4.6)
Total	5.1 (4.0)	5.1 (1.9)	6.5 (3.3)	6.5 (3.9)	9.9 (8.2)	5.0 (4.0)	5.0 (2.0)	6.6 (3.4)	6.3 (3.8)	10.6 (8.6)

TABLE XV. Summary of the main systematic uncertainties as percentages of the measured observable for the $|\eta(\ell)|$ differential cross sections in the D^+ channel. The uncertainty in the corresponding normalized cross section is given in parentheses next to the uncertainty in the absolute differential cross section.

Uncertainty (%)	$d\sigma_{\text{fid}}^{\text{OS-SS}}(W^- + D^+)/d(\eta(\ell))$ ($1/\sigma d\sigma/d\eta$)					$d\sigma_{\text{fid}}^{\text{OS-SS}}(W^+ + D^-)/d(\eta(\ell))$ ($1/\sigma d\sigma/d\eta$)				
	$ \eta(\ell) $ bins	[0.0, 0.5]	[0.5, 1.0]	[1.0, 1.5]	[1.5, 2.0]	[2.0, 2.5]	[0.0, 0.5]	[0.5, 1.0]	[1.0, 1.5]	[1.5, 2.0]
SV reconstruction	3.2 (0.1)	3.1 (0.2)	3.2 (0.2)	3.2 (0.1)	3.3 (0.2)	3.1 (0.1)	3.0 (0.1)	3.1 (0.2)	3.0 (0.2)	3.1 (0.2)
Jets and E_T^{miss}	1.6 (0.2)	1.9 (0.4)	1.6 (0.2)	1.5 (0.6)	1.7 (0.4)	1.6 (0.2)	1.8 (0.3)	1.8 (0.2)	1.5 (0.4)	1.9 (0.5)
Luminosity	0.8 (0.0)	0.8 (0.0)	0.8 (0.0)	0.8 (0.0)	0.8 (0.0)	0.8 (0.0)	0.8 (0.0)	0.8 (0.0)	0.8 (0.0)	0.8 (0.0)
Muon reconstruction	0.5 (0.2)	0.6 (0.1)	0.8 (0.1)	0.8 (0.1)	0.8 (0.2)	0.5 (0.2)	0.6 (0.1)	0.8 (0.1)	0.8 (0.1)	0.9 (0.2)
Electron reconstruction	0.2 (0.2)	0.3 (0.0)	0.3 (0.1)	0.4 (0.1)	0.4 (0.1)	0.2 (0.2)	0.3 (0.0)	0.3 (0.1)	0.4 (0.1)	0.4 (0.2)
Multijet background	0.2 (0.2)	0.2 (0.2)	0.2 (0.2)	0.3 (0.1)	0.9 (0.7)	0.2 (0.3)	0.1 (0.1)	0.1 (0.1)	0.4 (0.3)	0.7 (0.6)
Signal modeling	3.2 (0.4)	2.9 (0.3)	3.9 (1.1)	1.8 (1.4)	2.4 (0.7)	3.2 (0.4)	2.9 (0.3)	3.9 (1.2)	1.9 (1.4)	2.5 (0.7)
Signal branching ratio	1.6 (0.0)	1.6 (0.0)	1.5 (0.0)	1.6 (0.0)	1.5 (0.0)	1.6 (0.0)	1.6 (0.0)	1.6 (0.0)	1.7 (0.1)	1.6 (0.0)
Background modeling	1.5 (0.8)	2.2 (1.2)	1.7 (0.7)	1.2 (0.8)	2.1 (1.3)	1.8 (0.7)	2.0 (1.2)	1.7 (0.8)	1.3 (0.9)	1.9 (1.4)
Finite size of MC samples	1.6 (1.3)	1.8 (1.4)	2.1 (1.6)	1.9 (1.7)	2.7 (2.4)	1.7 (1.3)	1.8 (1.5)	1.9 (1.5)	2.2 (1.8)	3.0 (2.7)
Data statistical uncertainty	1.0 (0.9)	1.1 (1.0)	1.2 (1.1)	1.2 (1.1)	1.6 (1.5)	1.1 (1.0)	1.1 (1.0)	1.2 (1.1)	1.3 (1.2)	1.8 (1.7)
Total	5.5 (1.7)	5.5 (2.0)	6.0 (2.3)	5.0 (2.5)	5.8 (3.0)	5.4 (1.8)	5.4 (2.0)	6.0 (2.3)	5.1 (2.7)	6.0 (3.4)

TABLE XVI. Summary of the main systematic uncertainties as percentages of the measured observable for the $p_T(D^*)$ differential cross sections in the D^* channel. The uncertainty in the corresponding normalized cross section is given in parentheses next to the uncertainty in the absolute differential cross section.

Uncertainty (%)	$d\sigma_{\text{fid}}^{\text{OS-SS}}(W^- + D^+)/d(p_T(D^*)) (1/\sigma d\sigma/dp_T)$					$d\sigma_{\text{fid}}^{\text{OS-SS}}(W^+ + D^-)/d(p_T(D^*)) (1/\sigma d\sigma/dp_T)$				
	$p_T(D^*)$ bins [GeV]	[8, 12]	[12, 20]	[20, 40]	[40, 80]	[80, ∞]	[8, 12]	[12, 20]	[20, 40]	[40, 80]
SV reconstruction	2.4 (0.5)	2.3 (0.3)	2.3 (0.3)	2.4 (1.0)	4.5 (2.8)	2.4 (0.5)	2.3 (0.3)	2.3 (0.4)	2.5 (1.0)	4.8 (2.9)
Jets and E_T^{miss}	1.5 (0.6)	1.6 (0.5)	1.4 (0.5)	2.0 (1.3)	4.3 (3.2)	1.4 (0.6)	1.8 (0.6)	1.5 (0.4)	1.8 (1.3)	3.9 (3.2)
Luminosity	0.8 (0.0)	0.8 (0.0)	0.8 (0.0)	0.8 (0.0)	0.8 (0.0)	0.8 (0.0)	0.8 (0.0)	0.8 (0.0)	0.8 (0.0)	0.8 (0.0)
Muon reconstruction	0.8 (0.2)	0.7 (0.1)	0.6 (0.1)	0.5 (0.4)	0.6 (0.6)	0.8 (0.2)	0.7 (0.1)	0.6 (0.1)	0.5 (0.3)	0.5 (0.5)
Electron reconstruction	0.2 (0.1)	0.1 (0.2)	0.3 (0.2)	0.4 (0.2)	0.6 (0.4)	0.1 (0.1)	0.1 (0.2)	0.3 (0.2)	0.4 (0.2)	0.6 (0.4)
Multijet background	0.1 (0.1)	0.1 (0.1)	0.1 (0.1)	0.1 (0.1)	1.0 (1.0)	0.2 (0.1)	0.1 (0.1)	0.1 (0.1)	0.1 (0.1)	0.3 (0.4)
Signal modeling	3.7 (2.9)	2.6 (1.9)	3.1 (3.5)	3.5 (3.9)	1.2 (0.4)	3.7 (2.8)	2.6 (1.9)	3.1 (3.5)	3.5 (3.9)	1.2 (0.4)
Signal branching ratio	1.1 (0.0)	1.0 (0.0)	1.1 (0.0)	1.1 (0.0)	1.1 (0.0)	1.0 (0.0)	1.0 (0.0)	1.1 (0.0)	1.1 (0.0)	1.1 (0.0)
Background modeling	2.2 (1.3)	1.3 (0.6)	1.2 (0.7)	1.2 (0.9)	2.7 (2.2)	1.7 (0.8)	1.5 (0.5)	1.3 (0.7)	1.8 (1.5)	1.9 (1.8)
Finite size of MC samples	2.6 (1.9)	1.8 (1.4)	1.7 (1.4)	2.6 (2.3)	7.2 (6.9)	2.5 (1.8)	1.9 (1.4)	1.7 (1.4)	2.7 (2.4)	6.3 (6.0)
Data statistical uncertainty	1.8 (1.4)	1.2 (1.1)	1.1 (1.1)	1.9 (1.8)	5.0 (4.9)	1.9 (1.5)	1.3 (1.1)	1.2 (1.1)	2.0 (2.0)	5.7 (5.7)
Total	6.0 (3.8)	4.7 (2.7)	4.8 (4.0)	5.8 (5.1)	10.3 (8.9)	5.8 (3.8)	4.8 (2.7)	4.8 (4.0)	6.0 (5.3)	10.4 (9.1)

TABLE XVII. Summary of the main systematic uncertainties as percentages of the measured observable for the $|\eta(\ell)|$ differential cross sections in the D^* channel. The uncertainty in the corresponding normalized cross section is given in parentheses next to the uncertainty in the absolute differential cross section.

Uncertainty (%)	$d\sigma_{\text{fid}}^{\text{OS-SS}}(W^- + D^+)/d(\eta(\ell)) (1/\sigma d\sigma/d\eta)$					$d\sigma_{\text{fid}}^{\text{OS-SS}}(W^+ + D^-)/d(\eta(\ell)) (1/\sigma d\sigma/d\eta)$				
	$ \eta(\ell) $ bins	[0.0, 0.5]	[0.5, 1.0]	[1.0, 1.5]	[1.5, 2.0]	[2.0, 2.5]	[0.0, 0.5]	[0.5, 1.0]	[1.0, 1.5]	[1.5, 2.0]
SV reconstruction	2.4 (0.1)	2.4 (0.0)	2.4 (0.1)	2.5 (0.1)	2.5 (0.2)	2.4 (0.1)	2.5 (0.1)	2.4 (0.2)	2.4 (0.1)	2.4 (0.1)
Jets and E_T^{miss}	1.4 (0.7)	1.5 (0.4)	1.4 (0.4)	1.6 (0.5)	1.4 (1.0)	1.5 (0.2)	1.5 (0.2)	1.4 (0.2)	1.3 (0.3)	1.1 (0.5)
Luminosity	0.8 (0.0)	0.8 (0.0)	0.8 (0.0)	0.8 (0.0)	0.8 (0.0)	0.8 (0.0)	0.8 (0.0)	0.8 (0.0)	0.8 (0.0)	0.8 (0.0)
Muon reconstruction	0.5 (0.2)	0.6 (0.1)	0.8 (0.1)	0.8 (0.1)	0.8 (0.2)	0.5 (0.2)	0.6 (0.1)	0.8 (0.1)	0.8 (0.1)	0.9 (0.2)
Electron reconstruction	0.2 (0.1)	0.2 (0.0)	0.3 (0.0)	0.4 (0.1)	0.3 (0.1)	0.2 (0.1)	0.3 (0.0)	0.3 (0.1)	0.3 (0.1)	0.3 (0.1)
Multijet background	0.1 (0.1)	0.2 (0.1)	0.1 (0.1)	0.2 (0.2)	0.2 (0.2)	0.1 (0.1)	0.1 (0.1)	0.1 (0.1)	0.1 (0.1)	0.2 (0.2)
Signal modeling	1.1 (2.7)	2.0 (0.2)	4.6 (2.7)	1.8 (0.4)	2.6 (0.7)	1.1 (2.7)	2.1 (0.2)	4.5 (2.7)	1.8 (0.4)	2.6 (0.8)
Signal branching ratio	1.1 (0.0)	1.0 (0.0)	1.0 (0.0)	1.1 (0.0)	1.1 (0.0)	1.1 (0.0)	1.0 (0.0)	1.0 (0.0)	1.0 (0.0)	1.1 (0.0)
Background modeling	1.4 (0.6)	1.8 (1.0)	1.5 (0.8)	1.7 (1.0)	1.1 (0.7)	1.4 (0.7)	1.8 (1.0)	1.3 (0.7)	1.7 (1.1)	1.6 (0.9)
Finite size of MC samples	1.9 (1.6)	1.9 (1.6)	2.2 (1.8)	2.6 (2.2)	3.3 (2.9)	1.8 (1.5)	1.9 (1.6)	2.1 (1.8)	2.7 (2.3)	3.8 (3.3)
Data statistical uncertainty	1.4 (1.3)	1.5 (1.3)	1.6 (1.5)	1.8 (1.6)	2.2 (2.0)	1.4 (1.3)	1.5 (1.3)	1.7 (1.5)	2.0 (1.8)	2.5 (2.3)
Total	4.1 (3.5)	4.6 (2.2)	6.2 (3.6)	5.0 (2.8)	5.5 (3.5)	4.1 (3.4)	4.7 (2.2)	6.2 (3.6)	5.0 (3.0)	6.0 (4.0)

APPENDIX B: DIFFERENTIAL CROSS-SECTION TABLES

The measured differential cross sections in bins of $p_T(D^{(*)})$ and $|\eta(\ell)|$ are shown in Tables XVIII–XXI for the D^+ and D^* channels.

TABLE XVIII. Measured $p_T(D^+)$ differential fiducial cross section times the single-lepton-flavor W branching ratio in the $W + D^+$ channel. The displayed cross sections are integrated over each differential bin.

$p_T(D^{(*)})$ (GeV)	$\int d\sigma_{\text{fid}}^{\text{OS-SS}}(W^- + D^+)/d(p_T(D^+))$ (pb)	$1/\sigma \int d\sigma_{\text{fid}}^{\text{OS-SS}}(W^- + D^+)/d(p_T(D^+))$
[8, 12]	$15.04 \pm 0.19(\text{stat})^{+0.76}_{-0.72}(\text{syst})$	$0.2994 \pm 0.0030(\text{stat})^{+0.0117}_{-0.0116}(\text{syst})$
[12, 20]	$15.34 \pm 0.14(\text{stat})^{+0.78}_{-0.75}(\text{syst})$	$0.3054 \pm 0.0026(\text{stat})^{+0.0052}_{-0.0052}(\text{syst})$
[20, 40]	$13.78 \pm 0.12(\text{stat})^{+0.92}_{-0.85}(\text{syst})$	$0.2744 \pm 0.0024(\text{stat})^{+0.0088}_{-0.0085}(\text{syst})$
[40, 80]	$5.13 \pm 0.07(\text{stat})^{+0.34}_{-0.31}(\text{syst})$	$0.1021 \pm 0.0014(\text{stat})^{+0.0038}_{-0.0036}(\text{syst})$
[80, ∞)	$0.93 \pm 0.04(\text{stat})^{+0.09}_{-0.08}(\text{syst})$	$0.0186 \pm 0.0007(\text{stat})^{+0.0014}_{-0.0013}(\text{syst})$
	$\int d\sigma_{\text{fid}}^{\text{OS-SS}}(W^+ + D^-)/d(p_T(D^-))$ (pb)	$1/\sigma \int d\sigma_{\text{fid}}^{\text{OS-SS}}(W^+ + D^-)/d(p_T(D^-))$
[8, 12]	$14.61 \pm 0.19(\text{stat})^{+0.73}_{-0.69}(\text{syst})$	$0.3014 \pm 0.0032(\text{stat})^{+0.0116}_{-0.0115}(\text{syst})$
[12, 20]	$15.12 \pm 0.15(\text{stat})^{+0.75}_{-0.72}(\text{syst})$	$0.3120 \pm 0.0027(\text{stat})^{+0.0057}_{-0.0057}(\text{syst})$
[20, 40]	$13.07 \pm 0.12(\text{stat})^{+0.89}_{-0.82}(\text{syst})$	$0.2697 \pm 0.0025(\text{stat})^{+0.0089}_{-0.0085}(\text{syst})$
[40, 80]	$4.84 \pm 0.07(\text{stat})^{+0.31}_{-0.29}(\text{syst})$	$0.0999 \pm 0.0015(\text{stat})^{+0.0039}_{-0.0035}(\text{syst})$
[80, ∞)	$0.82 \pm 0.04(\text{stat})^{+0.08}_{-0.07}(\text{syst})$	$0.01690 \pm 0.0008(\text{stat})^{+0.0013}_{-0.0012}(\text{syst})$

TABLE XIX. Measured $|\eta(\ell)|$ differential fiducial cross section times the single-lepton-flavor W branching ratio in the $W + D^+$ channel. The displayed cross sections are integrated over each differential bin.

$ \eta(\ell) $	$\int d\sigma_{\text{fid}}^{\text{OS-SS}}(W^- + D^+)/d(\eta(\ell))$ (pb)	$1/\sigma \int d\sigma_{\text{fid}}^{\text{OS-SS}}(W^- + D^+)/d(\eta(\ell))$
[0.0, 0.5]	$12.27 \pm 0.13(\text{stat})^{+0.67}_{-0.64}(\text{syst})$	$0.2446 \pm 0.0023(\text{stat})^{+0.0036}_{-0.0036}(\text{syst})$
[0.5, 1.0]	$11.57 \pm 0.12(\text{stat})^{+0.63}_{-0.61}(\text{syst})$	$0.2305 \pm 0.0022(\text{stat})^{+0.0040}_{-0.0040}(\text{syst})$
[1.0, 1.5]	$10.41 \pm 0.12(\text{stat})^{+0.64}_{-0.59}(\text{syst})$	$0.2075 \pm 0.0022(\text{stat})^{+0.0042}_{-0.0041}(\text{syst})$
[1.5, 2.0]	$9.09 \pm 0.11(\text{stat})^{+0.45}_{-0.43}(\text{syst})$	$0.1810 \pm 0.0020(\text{stat})^{+0.0041}_{-0.0041}(\text{syst})$
[2.0, 2.5]	$6.85 \pm 0.11(\text{stat})^{+0.39}_{-0.37}(\text{syst})$	$0.1365 \pm 0.0020(\text{stat})^{+0.0037}_{-0.0036}(\text{syst})$
	$\int d\sigma_{\text{fid}}^{\text{OS-SS}}(W^+ + D^-)/d(\eta(\ell))$ (pb)	$1/\sigma \int d\sigma_{\text{fid}}^{\text{OS-SS}}(W^+ + D^-)/d(\eta(\ell))$
[0.0, 0.5]	$11.87 \pm 0.13(\text{stat})^{+0.65}_{-0.62}(\text{syst})$	$0.2455 \pm 0.0024(\text{stat})^{+0.0037}_{-0.0037}(\text{syst})$
[0.5, 1.0]	$11.55 \pm 0.12(\text{stat})^{+0.61}_{-0.60}(\text{syst})$	$0.2387 \pm 0.0023(\text{stat})^{+0.0041}_{-0.0041}(\text{syst})$
[1.0, 1.5]	$10.09 \pm 0.12(\text{stat})^{+0.61}_{-0.57}(\text{syst})$	$0.2087 \pm 0.0023(\text{stat})^{+0.0042}_{-0.0040}(\text{syst})$
[1.5, 2.0]	$8.60 \pm 0.12(\text{stat})^{+0.43}_{-0.41}(\text{syst})$	$0.1779 \pm 0.0022(\text{stat})^{+0.0042}_{-0.0042}(\text{syst})$
[2.0, 2.5]	$6.25 \pm 0.11(\text{stat})^{+0.37}_{-0.35}(\text{syst})$	$0.1292 \pm 0.0022(\text{stat})^{+0.0038}_{-0.0037}(\text{syst})$

TABLE XX. Measured $p_T(D^{*+})$ differential fiducial cross section times the single-lepton-flavor W branching ratio in the $W + D^{*+}$ channel. The displayed cross sections are integrated over each differential bin.

$p_T(D^{(*)})$ (GeV)	$\int d\sigma_{\text{fid}}^{\text{OS-SS}}(W^- + D^{*+})/d(p_T(D^{*+}))$ (pb)	$1/\sigma \int d\sigma_{\text{fid}}^{\text{OS-SS}}(W^- + D^{*+})/d(p_T(D^{*+}))$
[8, 12]	$14.50 \pm 0.26(\text{stat})^{+0.85}_{-0.79}(\text{syst})$	$0.2839 \pm 0.0041(\text{stat})^{+0.0102}_{-0.0100}(\text{syst})$
[12, 20]	$15.88 \pm 0.19(\text{stat})^{+0.73}_{-0.69}(\text{syst})$	$0.3110 \pm 0.0034(\text{stat})^{+0.0075}_{-0.0075}(\text{syst})$
[20, 40]	$14.19 \pm 0.16(\text{stat})^{+0.68}_{-0.64}(\text{syst})$	$0.2779 \pm 0.0030(\text{stat})^{+0.0107}_{-0.0105}(\text{syst})$
[40, 80]	$5.42 \pm 0.10(\text{stat})^{+0.31}_{-0.29}(\text{syst})$	$0.1062 \pm 0.0019(\text{stat})^{+0.0052}_{-0.0049}(\text{syst})$
[80, ∞)	$1.07 \pm 0.05(\text{stat})^{+0.10}_{-0.09}(\text{syst})$	$0.0209 \pm 0.0010(\text{stat})^{+0.0016}_{-0.0015}(\text{syst})$
	$\int d\sigma_{\text{fid}}^{\text{OS-SS}}(W^+ + D^{*-})/d(p_T(D^{*-}))$ (pb)	$1/\sigma \int d\sigma_{\text{fid}}^{\text{OS-SS}}(W^+ + D^{*-})/d(p_T(D^{*-}))$
[8, 12]	$14.26 \pm 0.27(\text{stat})^{+0.82}_{-0.76}(\text{syst})$	$0.2849 \pm 0.0043(\text{stat})^{+0.0100}_{-0.0097}(\text{syst})$
[12, 20]	$15.60 \pm 0.20(\text{stat})^{+0.74}_{-0.70}(\text{syst})$	$0.3118 \pm 0.0036(\text{stat})^{+0.0076}_{-0.0076}(\text{syst})$
[20, 40]	$14.08 \pm 0.17(\text{stat})^{+0.68}_{-0.64}(\text{syst})$	$0.2814 \pm 0.0032(\text{stat})^{+0.0108}_{-0.0107}(\text{syst})$
[40, 80]	$5.11 \pm 0.10(\text{stat})^{+0.30}_{-0.28}(\text{syst})$	$0.1022 \pm 0.0020(\text{stat})^{+0.0052}_{-0.0050}(\text{syst})$
[80, ∞)	$0.99 \pm 0.06(\text{stat})^{+0.09}_{-0.08}(\text{syst})$	$0.0197 \pm 0.0011(\text{stat})^{+0.0015}_{-0.0013}(\text{syst})$

TABLE XXI. Measured $|\eta(\ell)|$ differential fiducial cross section times the single-lepton-flavor W branching ratio in the $W + D^{*+}$ channel. The displayed cross sections are integrated over each differential bin.

$ \eta(\ell) $	$\int d\sigma_{\text{fid}}^{\text{OS-SS}}(W^- + D^{*+})/d(\eta(\ell))$ (pb)	$1/\sigma \int d\sigma_{\text{fid}}^{\text{OS-SS}}(W^- + D^{*+})/d(\eta(\ell))$
[0.0, 0.5]	$12.18 \pm 0.18(\text{stat})^{+0.48}_{-0.46}(\text{syst})$	$0.2405 \pm 0.0031(\text{stat})^{+0.0078}_{-0.0078}(\text{syst})$
[0.5, 1.0]	$11.77 \pm 0.17(\text{stat})^{+0.53}_{-0.50}(\text{syst})$	$0.2325 \pm 0.0031(\text{stat})^{+0.0042}_{-0.0041}(\text{syst})$
[1.0, 1.5]	$10.61 \pm 0.17(\text{stat})^{+0.67}_{-0.61}(\text{syst})$	$0.2095 \pm 0.0031(\text{stat})^{+0.0071}_{-0.0066}(\text{syst})$
[1.5, 2.0]	$8.85 \pm 0.16(\text{stat})^{+0.42}_{-0.40}(\text{syst})$	$0.1748 \pm 0.0029(\text{stat})^{+0.0040}_{-0.0039}(\text{syst})$
[2.0, 2.5]	$7.22 \pm 0.16(\text{stat})^{+0.38}_{-0.36}(\text{syst})$	$0.1427 \pm 0.0028(\text{stat})^{+0.0042}_{-0.0040}(\text{syst})$
	$\int d\sigma_{\text{fid}}^{\text{OS-SS}}(W^+ + D^{*-})/d(\eta(\ell))$ (pb)	$1/\sigma \int d\sigma_{\text{fid}}^{\text{OS-SS}}(W^+ + D^{*-})/d(\eta(\ell))$
[0.0, 0.5]	$12.52 \pm 0.18(\text{stat})^{+0.50}_{-0.48}(\text{syst})$	$0.2510 \pm 0.0033(\text{stat})^{+0.0078}_{-0.0077}(\text{syst})$
[0.5, 1.0]	$12.14 \pm 0.18(\text{stat})^{+0.55}_{-0.52}(\text{syst})$	$0.2434 \pm 0.0032(\text{stat})^{+0.0042}_{-0.0042}(\text{syst})$
[1.0, 1.5]	$10.29 \pm 0.18(\text{stat})^{+0.64}_{-0.58}(\text{syst})$	$0.2063 \pm 0.0032(\text{stat})^{+0.0070}_{-0.0065}(\text{syst})$
[1.5, 2.0]	$8.38 \pm 0.16(\text{stat})^{+0.39}_{-0.37}(\text{syst})$	$0.1680 \pm 0.0030(\text{stat})^{+0.0040}_{-0.0039}(\text{syst})$
[2.0, 2.5]	$6.55 \pm 0.16(\text{stat})^{+0.37}_{-0.34}(\text{syst})$	$0.1313 \pm 0.0030(\text{stat})^{+0.0044}_{-0.0042}(\text{syst})$

APPENDIX C: THE MEASUREMENT COVARIANCE MATRICES

Covariance matrices encoding the measurement error associated with the differential $W + D^{(*)}$ cross-section measurement are given in Figs. 11–13. Covariance matrices are given separately for the D^+ and D^* channels and separately for $p_T(D^{(*)})$

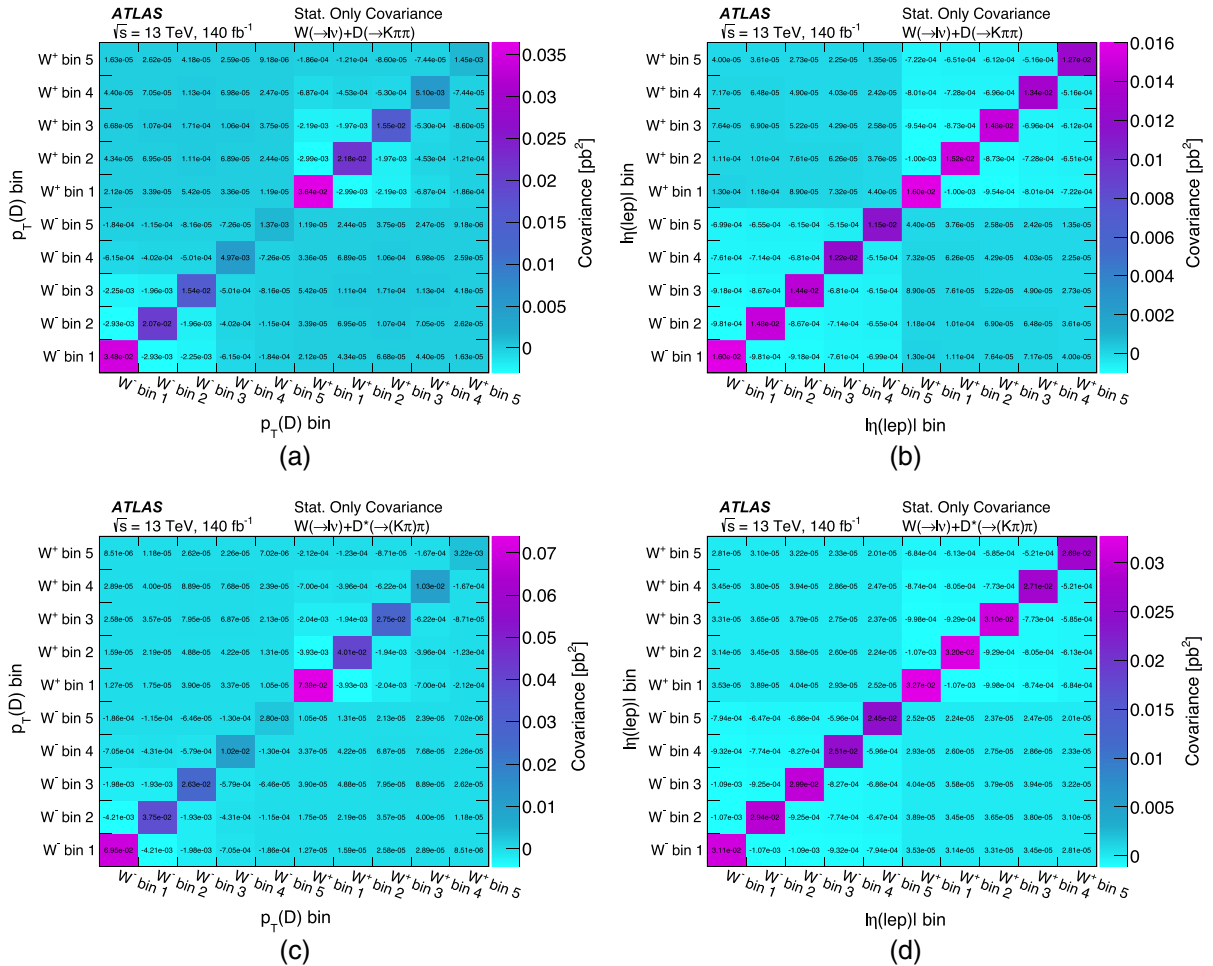


FIG. 11. The data statistical uncertainty covariance matrix for the differential $W + D^{(*)}$ fits: (a) D^+ $p_T(D^{(*)})$ fit, (b) D^+ $|\eta(\ell)|$ fit, (c) D^* $p_T(D^{(*)})$ fit, and (d) D^* $|\eta(\ell)|$ fit.

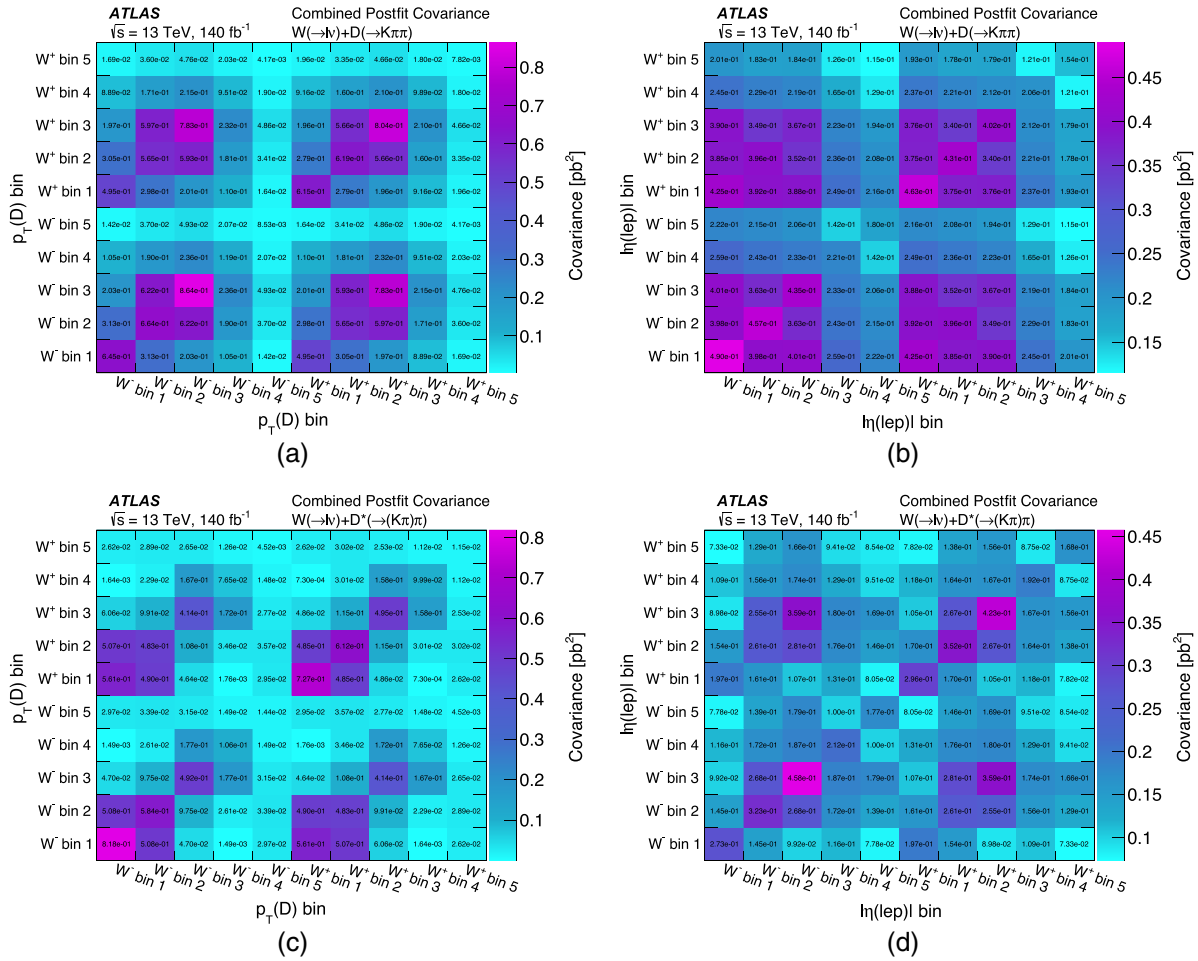


FIG. 12. The combined statistical and systematic uncertainty covariance matrix for the differential $W + D^{(*)}$ fits: (a) $D^+ p_T(D^{(*)})$ fit, (b) $D^+ |\eta(\ell)|$ fit, (c) $D^* p_T(D^{(*)})$ fit, and (d) $D^* |\eta(\ell)|$ fit. The systematic uncertainties are evaluated with the postfit values of the nuisance parameters, corresponding to the measured differential cross sections.

and $|\eta(\ell)|$ differential bins. Covariance matrices encoding only the statistical uncertainty are given in Fig. 11. Figure 12 includes the full set of measurement uncertainties with postfit values of the nuisance parameters and Fig. 13 shows the covariance matrix with prefit values of the nuisance parameters.

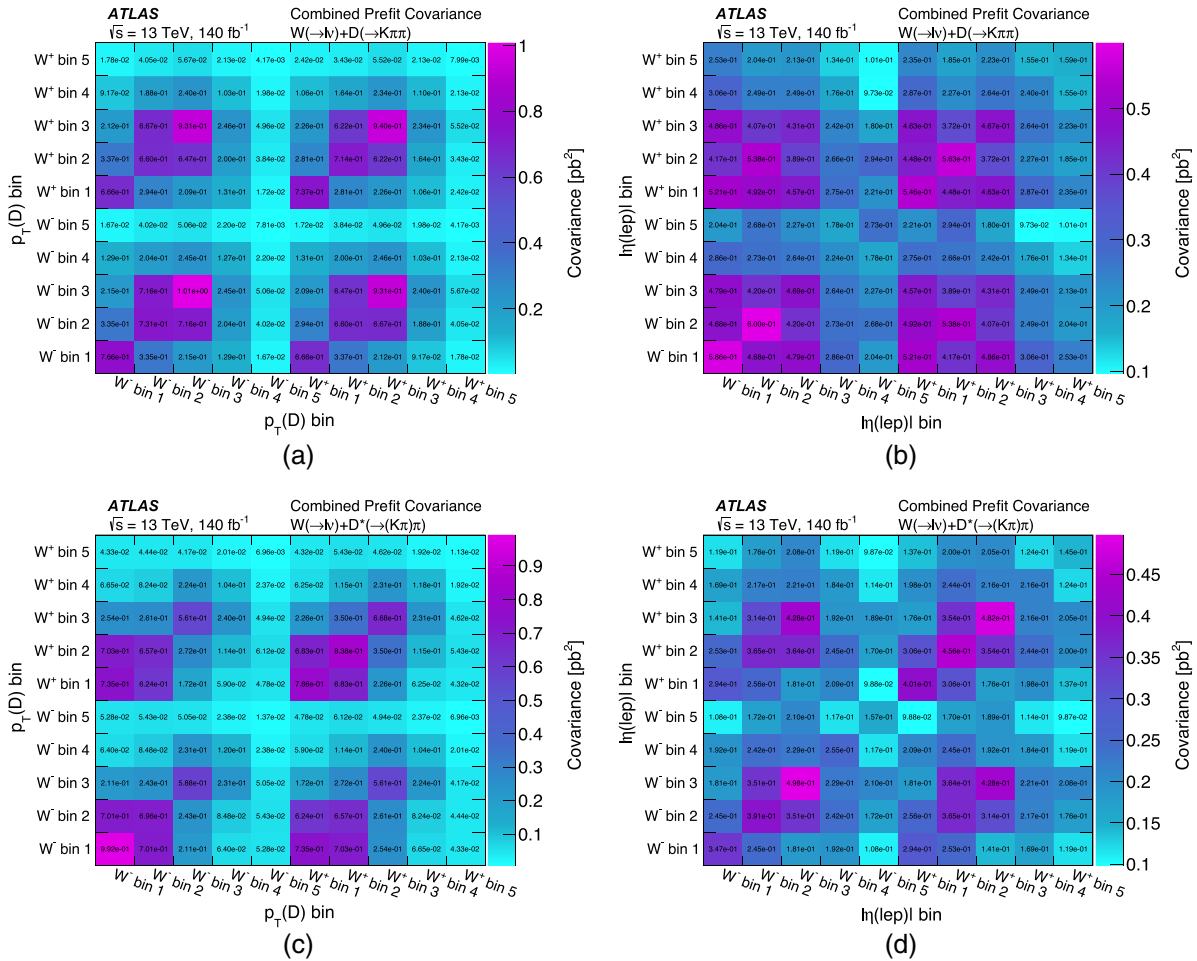


FIG. 13. The combined statistical and systematic uncertainty covariance matrix for the differential $W + D^{(*)}$ fits: (a) $D^+ p_T(D^{*})$ fit, (b) $D^+ |\eta(\ell)|$ fit, (c) $D^* p_T(D^{*})$ fit, and (d) $D^* |\eta(\ell)|$ fit. The systematic uncertainties are evaluated with the prefit values of the nuisance parameters.

- [1] HERMES Collaboration, Measurement of parton distributions of strange quarks in the nucleon from charged-kaon production in deep-inelastic scattering on the deuteron, *Phys. Lett. B* **666**, 446 (2008).
- [2] ZEUS Collaboration, Charm production in charged current deep inelastic scattering at HERA, *J. High Energy Phys.* **05** (2019) 201.
- [3] CCFR Collaboration, Determination of the strange quark content of the nucleon from a next-to-leading order QCD analysis of neutrino charm production, *Z. Phys. C* **65**, 189 (1995).
- [4] CHORUS Collaboration, Leading order analysis of neutrino induced dimuon events in the CHORUS experiment, *Nucl. Phys.* **B798**, 1 (2008).
- [5] NuTeV Collaboration, Precise measurement of dimuon production cross-sections in ν_μ Fe and $\bar{\nu}_\mu$ Fe deep inelastic scattering at the Tevatron, *Phys. Rev. D* **64**, 112006 (2001).
- [6] NuTeV Collaboration, Measurement of the Nucleon Strange-Antistrange Asymmetry at Next-to-Leading Order in QCD from NuTeV Dimuon Data, *Phys. Rev. Lett.* **99**, 192001 (2007).
- [7] NOMAD Collaboration, A precision measurement of charm dimuon production in neutrino interactions from the NOMAD experiment, *Nucl. Phys.* **B876**, 339 (2013).
- [8] L. Evans and P. Bryant, LHC machine, *J. Instrum.* **3**, S08001 (2008).
- [9] ATLAS Collaboration, Determination of the parton distribution functions of the proton using diverse ATLAS data

- from pp collisions at $\sqrt{s} = 7, 8$ and 13 TeV, *Eur. Phys. J. C* **82**, 438 (2021).
- [10] ATLAS Collaboration, Precision measurement and interpretation of inclusive W^+ , W^- and Z/γ^* production cross sections with the ATLAS detector, *Eur. Phys. J. C* **77**, 367 (2017).
- [11] ATLAS Collaboration, Measurement of the transverse momentum and ϕ_η^* distributions of Drell-Yan lepton pairs in proton–proton collisions at $\sqrt{s} = 8$ TeV with the ATLAS detector, *Eur. Phys. J. C* **76**, 291 (2016).
- [12] F. Faura, S. Iranipour, E. R. Nocera, J. Rojo, and M. Ubiali, The strangest proton?, *Eur. Phys. J. C* **80**, 1168 (2020).
- [13] N. Cabibbo, Unitary Symmetry and Leptonic Decays, *Phys. Rev. Lett.* **10**, 531 (1963).
- [14] M. Kobayashi and T. Maskawa, CP violation in the renormalizable theory of weak interaction, *Prog. Theor. Phys.* **49**, 652 (1973).
- [15] M. Czakon, A. Mitov, M. Pellen, and R. Poncelet, NNLO QCD predictions for $W+c$ -jet production at the LHC, *J. High Energy Phys.* **06** (2021) 100.
- [16] U. Baur, F. Halzen, S. Keller, M. L. Mangano, and K. Riesselmann, The charm content of $W + 1$ jet events as a probe of the strange quark distribution function, *Phys. Lett. B* **318**, 544 (1993).
- [17] W. T. Giele, S. Keller, and E. Laenen, QCD corrections to W boson plus heavy quark production at the Tevatron, *Phys. Lett. B* **372**, 141 (1996).
- [18] CDF Collaboration, Observation of the Production of a W Boson in Association with a Single Charm Quark, *Phys. Rev. Lett.* **110**, 071801 (2013).
- [19] ATLAS Collaboration, Measurement of the production cross section for W -bosons in association with jets in pp collisions at $\sqrt{s} = 7$ TeV with the ATLAS detector, *Phys. Lett. B* **698**, 325 (2011).
- [20] ATLAS Collaboration, Measurement of the production of a W boson in association with a charm quark in pp collisions at $\sqrt{s} = 7$ TeV with the ATLAS detector, *J. High Energy Phys.* **05** (2014) 068.
- [21] CMS Collaboration, Measurement of associated $W +$ charm production in pp collisions at $\sqrt{s} = 7$ TeV, *J. High Energy Phys.* **02** (2014) 013.
- [22] CMS Collaboration, Measurements of the associated production of a W boson and a charm quark in proton–proton collisions at $\sqrt{s} = 8$ TeV, *Eur. Phys. J. C* **82**, 1094 (2022).
- [23] CMS Collaboration, Measurement of associated production of a W boson and a charm quark in proton–proton collisions at $\sqrt{s} = 13$ TeV, *Eur. Phys. J. C* **79**, 269 (2019).
- [24] LHCb Collaboration, Study of W boson production in association with beauty and charm, *Phys. Rev. D* **92**, 052001 (2015).
- [25] G. Cowan, K. Cranmer, E. Gross, and O. Vitells, Asymptotic formulae for likelihood-based tests of new physics, *Eur. Phys. J. C* **71**, 1554 (2011); **73**, 2501(E) (2013).
- [26] S. Alekhin, J. Blümlein, S. Moch, and R. Placakyte, Parton distribution functions, α_s , and heavy-quark masses for LHC Run II, *Phys. Rev. D* **96**, 014011 (2017).
- [27] T.-J. Hou *et al.*, New CTEQ global analysis of quantum chromodynamics with high-precision data from the LHC, *Phys. Rev. D* **103**, 014013 (2021).
- [28] S. Bailey, T. Cridge, L. A. Harland-Lang, A. D. Martin, and R. S. Thorne, Parton distributions from LHC, HERA, Tevatron and fixed target data: MSHT20 PDFs, *Eur. Phys. J. C* **81**, 341 (2021).
- [29] R. D. Ball *et al.*, The PDF4LHC21 combination of global PDF fits for the LHC Run III, *J. Phys. G* **49**, 080501 (2022).
- [30] R. D. Ball *et al.*, Parton distributions from high-precision collider data, *Eur. Phys. J. C* **77**, 663 (2017).
- [31] R. D. Ball *et al.*, The path to proton structure at 1% accuracy, *Eur. Phys. J. C* **82**, 428 (2022).
- [32] M. Czakon, A. Mitov, M. Pellen, and R. Poncelet, A detailed investigation of $W+c$ -jet at the LHC, *J. High Energy Phys.* **02** (2023) 241.
- [33] A. Banfi, G. P. Salam, and G. Zanderighi, Infrared safe definition of jet flavor, *Eur. Phys. J. C* **47**, 113 (2006).
- [34] M. Czakon, T. Generet, A. Mitov, and R. Poncelet, B-hadron production in NNLO QCD: Application to LHC $t\bar{t}$ events with leptonic decays, *J. High Energy Phys.* **10** (2021) 216.
- [35] J. Alwall, R. Frederix, S. Frixione, V. Hirschi, F. Maltoni, O. Mattelaer, H.-S. Shao, T. Stelzer, P. Torrielli, and M. Zaro, The automated computation of tree-level and next-to-leading order differential cross sections, and their matching to parton shower simulations, *J. High Energy Phys.* **07** (2014) 079.
- [36] G. Bevilacqua, M. V. Garzelli, A. Kardos, and L. Toth, $W +$ charm production with massive c quarks in Powhel, *J. High Energy Phys.* **04** (2022) 056.
- [37] Z. Trocsanyi, M. V. Garzelli, and A. Kardos, NLO event samples for the LHC, *Proc. Sci. EPS-HEP2011* (**2011**) 282 [arXiv:1111.1446].
- [38] ATLAS Collaboration, The ATLAS experiment at the CERN Large Hadron Collider, *J. Instrum.* **3**, S08003 (2008).
- [39] ATLAS Collaboration, ATLAS insertable B-layer technical design, Report No. ATLAS-TDR-19; No. CERN-LHCC-2010-013, 2010, <https://cds.cern.ch/record/1291633>; Addendum No. ATLAS-TDR-19-ADD-1; CERN-LHCC-2012-009, 2012, <https://cds.cern.ch/record/1451888>.
- [40] B. Abbott *et al.*, Production and integration of the ATLAS insertable B-layer, *J. Instrum.* **13**, T05008 (2018).
- [41] ATLAS Collaboration, Performance of the ATLAS trigger system in 2015, *Eur. Phys. J. C* **77**, 317 (2017).
- [42] ATLAS Collaboration, The ATLAS Collaboration software and firmware, Report No. ATL-SOFT-PUB-2021-001, 2021, <https://cds.cern.ch/record/2767187>.
- [43] ATLAS Collaboration, ATLAS data quality operations and performance for 2015–2018 data-taking, *J. Instrum.* **15**, P04003 (2020).
- [44] ATLAS Collaboration, Luminosity determination in pp collisions at $\sqrt{s} = 13$ TeV using the ATLAS detector at the LHC, arXiv:2212.09379.
- [45] G. Avoni *et al.*, The new LUCID-2 detector for luminosity measurement and monitoring in ATLAS, *J. Instrum.* **13**, P07017 (2018).
- [46] ATLAS Collaboration, Performance of electron and photon triggers in ATLAS during LHC Run 2, *Eur. Phys. J. C* **80**, 47 (2020).
- [47] ATLAS Collaboration, Performance of the ATLAS muon triggers in Run 2, *J. Instrum.* **15**, P09015 (2020).

- [48] ATLAS Collaboration, The ATLAS simulation infrastructure, *Eur. Phys. J. C* **70**, 823 (2010).
- [49] S. Agostinelli *et al.* (GEANT4 Collaboration), GEANT4—A simulation toolkit, *Nucl. Instrum. Methods Phys. Res., Sect. A* **506**, 250 (2003).
- [50] T. Sjöstrand, S. Mrenna, and P. Skands, A brief introduction to PYTHIA 8.1, *Comput. Phys. Commun.* **178**, 852 (2008).
- [51] R. D. Ball *et al.*, Parton distributions with LHC data, *Nucl. Phys.* **B867**, 244 (2013).
- [52] ATLAS Collaboration, The PYTHIA 8 A3 tune description of ATLAS minimum bias and inelastic measurements incorporating the Donnachie–Landshoff diffractive model, Report No. ATL-PHYS-PUB-2016-017, 2016, <https://cds.cern.ch/record/2206965>.
- [53] ATLAS Collaboration, Measurement of the Inelastic Proton-Proton Cross Section at $\sqrt{s} = 13$ TeV with the ATLAS Detector at the LHC, *Phys. Rev. Lett.* **117**, 182002 (2016).
- [54] M. Lisovsky, A. Verbytskyi, and O. Zenaiev, Combined analysis of charm-quark fragmentation-fraction measurements, *Eur. Phys. J. C* **76**, 397 (2016).
- [55] ATLAS Collaboration, Reweighting heavy-flavor production fractions to reduce flavor modelling uncertainties for ATLAS, Report No. ATL-PHYS-PUB-2022-035, 2022, <https://cds.cern.ch/record/2816367>.
- [56] E. Bothmann *et al.*, Event generation with Sherpa 2.2, *SciPost Phys.* **7**, 034 (2019).
- [57] T. Gleisberg and S. Höche, COMIX, A new matrix element generator, *J. High Energy Phys.* **12** (2008) 039.
- [58] F. Buccioni, J.-N. Lang, J. M. Lindert, P. Maierhöfer, S. Pozzorini, H. Zhang, and M. F. Zoller, OpenLoops 2, *Eur. Phys. J. C* **79**, 866 (2019).
- [59] F. Cascioli, P. Maierhöfer, and S. Pozzorini, Scattering Amplitudes with OpenLoops, *Phys. Rev. Lett.* **108**, 111601 (2012).
- [60] A. Denner, S. Dittmaier, and L. Hofer, Collier: A Fortran-based complex one-loop library in extended regularizations, *Comput. Phys. Commun.* **212**, 220 (2017).
- [61] R. D. Ball *et al.*, Parton distributions for the LHC run II, *J. High Energy Phys.* **04** (2015) 040.
- [62] S. Schumann and F. Krauss, A parton shower algorithm based on Catani-Seymour dipole factorisation, *J. High Energy Phys.* **03** (2008) 038.
- [63] J.-C. Winter, F. Krauss, and G. Soff, A modified cluster-hadronization model, *Eur. Phys. J. C* **36**, 381 (2004).
- [64] S. Höche, F. Krauss, M. Schönherr, and F. Siegert, A critical appraisal of NLO + PS matching methods, *J. High Energy Phys.* **09** (2012) 049.
- [65] S. Catani, F. Krauss, B. R. Webber, and R. Kuhn, QCD matrix elements + parton showers, *J. High Energy Phys.* **11** (2001) 063.
- [66] S. Höche, F. Krauss, S. Schumann, and F. Siegert, QCD matrix elements and truncated showers, *J. High Energy Phys.* **05** (2009) 053.
- [67] S. Höche, F. Krauss, M. Schönherr, and F. Siegert, QCD matrix elements + parton showers. The NLO case, *J. High Energy Phys.* **04** (2013) 027.
- [68] E. Bothmann, M. Schönherr, and S. Schumann, Reweighting QCD matrix-element and parton-shower calculations, *Eur. Phys. J. C* **76**, 590 (2016).
- [69] ATLAS Collaboration, Modelling and computational improvements to the simulation of single vector-boson plus jet processes for the ATLAS experiment, *J. High Energy Phys.* **08** (2022) 089.
- [70] L. Lönnblad, Correcting the colour-dipole cascade model with fixed order matrix elements, *J. High Energy Phys.* **05** (2002) 046.
- [71] L. Lönnblad and S. Prestel, Matching tree-level matrix elements with interleaved showers, *J. High Energy Phys.* **03** (2012) 019.
- [72] ATLAS Collaboration, ATLAS PYTHIA 8 tunes to 7 TeV data, Report No. ATL-PHYS-PUB-2014-021, 2014, <https://cds.cern.ch/record/1966419>.
- [73] D. J. Lange, The EvtGen particle decay simulation package, *Nucl. Instrum. Methods Phys. Res., Sect. A* **462**, 152 (2001).
- [74] R. Frederix and S. Frixione, Merging meets matching in MC@NLO, *J. High Energy Phys.* **12** (2012) 061.
- [75] G. Bonvicini *et al.*, Dalitz plot analysis of the $D^+ \rightarrow K^- \pi^+ \pi^+$ decay, *Phys. Rev. D* **78**, 052001 (2008).
- [76] S. Frixione, G. Ridolfi, and P. Nason, A positive-weight next-to-leading-order Monte Carlo for heavy flavour hadroproduction, *J. High Energy Phys.* **09** (2007) 126.
- [77] P. Nason, A new method for combining NLO QCD with shower Monte Carlo algorithms, *J. High Energy Phys.* **11** (2004) 040.
- [78] S. Frixione, P. Nason, and C. Oleari, Matching NLO QCD computations with parton shower simulations: The POWHEG method, *J. High Energy Phys.* **11** (2007) 070.
- [79] S. Alioli, P. Nason, C. Oleari, and E. Re, A general framework for implementing NLO calculations in shower Monte Carlo programs: The POWHEG BOX, *J. High Energy Phys.* **06** (2010) 043.
- [80] ATLAS Collaboration, Studies on top-quark Monte Carlo modelling for Top2016, Report No. ATL-PHYS-PUB-2016-020, 2016, <https://cds.cern.ch/record/2216168>.
- [81] S. Frixione, E. Laenen, P. Motylinski, and B. R. Webber, Angular correlations of lepton pairs from vector boson and top quark decays in Monte Carlo simulations, *J. High Energy Phys.* **04** (2007) 081.
- [82] P. Artoisenet, R. Frederix, O. Mattelaer, and R. Rietkerk, Automatic spin-entangled decays of heavy resonances in Monte Carlo simulations, *J. High Energy Phys.* **03** (2013) 015.
- [83] M. Beneke, P. Falgari, S. Klein, and C. Schwinn, Hadronic top-quark pair production with NNLL threshold resummation, *Nucl. Phys.* **B855**, 695 (2012).
- [84] M. Cacciari, M. Czakon, M. Mangano, A. Mitov, and P. Nason, Top-pair production at hadron colliders with next-to-next-to-leading logarithmic soft-gluon resummation, *Phys. Lett. B* **710**, 612 (2012).
- [85] P. Bärnreuther, M. Czakon, and A. Mitov, Percent-Level-Precision Physics at the Tevatron: Next-to-Next-to-Leading Order QCD Corrections to $q\bar{q} \rightarrow t\bar{t} + X$, *Phys. Rev. Lett.* **109**, 132001 (2012).
- [86] M. Czakon and A. Mitov, NNLO corrections to top-pair production at hadron colliders: The all-fermionic scattering channels, *J. High Energy Phys.* **12** (2012) 054.
- [87] M. Czakon and A. Mitov, NNLO corrections to top pair production at hadron colliders: The quark-gluon reaction, *J. High Energy Phys.* **01** (2013) 080.

- [88] M. Czakon, P. Fiedler, and A. Mitov, Total Top-Quark Pair-Production Cross Section at Hadron Colliders Through $O(\alpha_s^4)$, *Phys. Rev. Lett.* **110**, 252004 (2013).
- [89] M. Czakon and A. Mitov, $\text{Top}++$: A program for the calculation of the top-pair cross-section at hadron colliders, *Comput. Phys. Commun.* **185**, 2930 (2014).
- [90] M. Bähr *et al.*, Herwig++ physics and manual, *Eur. Phys. J. C* **58**, 639 (2008).
- [91] J. Bellm *et al.*, Herwig 7.0/Herwig++ 3.0 release note, *Eur. Phys. J. C* **76**, 196 (2016).
- [92] L. A. Harland-Lang, A. D. Martin, P. Motylinski, and R. S. Thorne, Parton distributions in the LHC era: MMHT2014PDFs, *Eur. Phys. J. C* **75**, 204 (2015).
- [93] S. Frixione, E. Laenen, P. Motylinski, C. White, and B. R. Webber, Single-top hadroproduction in association with a W boson, *J. High Energy Phys.* **07** (2008) 029.
- [94] M. Aliev, H. Lacker, U. Langenfeld, S. Moch, P. Uwer, and M. Wiedermann, HATHOR—HADronic top and heavy quarks crOSS section calculator, *Comput. Phys. Commun.* **182**, 1034 (2011).
- [95] P. Kant, O.M. Kind, T. Kintscher, T. Lohse, T. Martini, S. Mölbitz, P. Rieck, and P. Uwer, HATHOR for single top-quark production: Updated predictions and uncertainty estimates for single top-quark production in hadronic collisions, *Comput. Phys. Commun.* **191**, 74 (2015).
- [96] ATLAS Collaboration, Studies on top-quark Monte Carlo modelling with sherpa and MG5_aMC@NLO, Report No. ATL-PHYS-PUB-2017-007, 2017, <https://cds.cern.ch/record/2261938>.
- [97] A. Denner, S. Dittmaier, M. Roth, and M.M. Weber, Electroweak radiative corrections to $e^+e^- \rightarrow \nu$ anti- ν H, *Nucl. Phys.* **B660**, 289 (2003).
- [98] ATLAS Collaboration, Electron and photon performance measurements with the ATLAS detector using the 2015–2017 LHC proton-proton collision data, *J. Instrum.* **14**, P12006 (2019).
- [99] ATLAS Collaboration, Muon reconstruction performance of the ATLAS detector in proton–proton collision data at $\sqrt{s} = 13$ TeV, *Eur. Phys. J. C* **76**, 292 (2016).
- [100] ATLAS Collaboration, Muon reconstruction and identification efficiency in ATLAS using the full Run 2 pp collision data set at $\sqrt{s} = 13$ TeV, *Eur. Phys. J. C* **81**, 578 (2021).
- [101] ATLAS Collaboration, Jet reconstruction and performance using particle flow with the ATLAS detector, *Eur. Phys. J. C* **77**, 466 (2017).
- [102] M. Cacciari, G.P. Salam, and G. Soyez, The anti- k_r jet clustering algorithm, *J. High Energy Phys.* **04** (2008) 063.
- [103] M. Cacciari, G.P. Salam, and G. Soyez, Fastjet user manual, *Eur. Phys. J. C* **72**, 1896 (2012).
- [104] ATLAS Collaboration, Jet energy scale and resolution measured in proton–proton collisions at $\sqrt{s} = 13$ TeV with the ATLAS detector, *Eur. Phys. J. C* **81**, 689 (2020).
- [105] ATLAS Collaboration, Tagging and suppression of pileup jets with the ATLAS detector, Report No. ATLAS-CONF-2014-018, 2014, <https://cds.cern.ch/record/1700870>.
- [106] ATLAS Collaboration, ATLAS b -jet identification performance and efficiency measurement with $t\bar{t}$ events in pp collisions at $\sqrt{s} = 13$ TeV, *Eur. Phys. J. C* **79**, 970 (2019).
- [107] ATLAS Collaboration, Optimisation and performance studies of the ATLAS b -tagging algorithms for the 2017–18 LHC run, Report No. ATL-PHYS-PUB-2017-013, 2017, <https://cds.cern.ch/record/2273281>.
- [108] ATLAS Collaboration, ATLAS flavour-tagging algorithms for the LHC Run 2 pp collision dataset, [arXiv:2211.16345](https://arxiv.org/abs/2211.16345).
- [109] ATLAS Collaboration, Performance of missing transverse momentum reconstruction with the ATLAS detector using proton–proton collisions at $\sqrt{s} = 13$ TeV, *Eur. Phys. J. C* **78**, 903 (2018).
- [110] ATLAS Collaboration, E_T^{miss} performance in the ATLAS detector using 2015–2016 LHC pp collisions, Report No. ATLAS-CONF-2018-023, 2018, <https://cds.cern.ch/record/2625233>.
- [111] ATLAS Collaboration, Early inner detector tracking performance in the 2015 data at $\sqrt{s} = 13$ TeV, Report No. ATL-PHYS-PUB-2015-051, 2015, <https://cds.cern.ch/record/2110140>.
- [112] R.L. Workman *et al.* (Particle Data Group), Review of particle physics, *Prog. Theor. Exp. Phys.* **2022**, 083C01 (2022).
- [113] ATLAS Collaboration, Tools for estimating fake/non-prompt lepton backgrounds with the ATLAS detector at the LHC, [arXiv:2211.16178](https://arxiv.org/abs/2211.16178).
- [114] L. Moneta *et al.*, The RooStats project, *Proc. Sci. ACAT2010* (2010) 057 [[arXiv:1009.1003](https://arxiv.org/abs/1009.1003)].
- [115] W. Verkerke and D. Kirkby, The RooFit toolkit for data modeling, [arXiv:physics/0306116](https://arxiv.org/abs/physics/0306116).
- [116] R.J. Barlow and C. Beeston, Fitting using finite Monte Carlo samples, *Comput. Phys. Commun.* **77**, 219 (1993).
- [117] ATLAS Collaboration, Measurement of the c -jet mistagging efficiency in $t\bar{t}$ events using pp collision data at $\sqrt{s} = 13$ TeV collected with the ATLAS detector, *Eur. Phys. J. C* **82**, 95 (2022).
- [118] ATLAS Collaboration, Calibration of the light-flavour jet mistagging efficiency of the b -tagging algorithms with $Z + \text{jets}$ events using 139 fb^{-1} of ATLAS proton-proton collision data at $\sqrt{s} = 13$ TeV, [arXiv:2301.06319](https://arxiv.org/abs/2301.06319).
- [119] ATLAS Collaboration, Alignment of the ATLAS inner detector in Run-2, *Eur. Phys. J. C* **80**, 1194 (2020).
- [120] A. Buckley, J. Ferrando, S. Lloyd, K. Nordström, B. Page, M. Rüfenacht, M. Schönherr, and G. Watt, LHAPDF6: Parton density access in the LHC precision era, *Eur. Phys. J. C* **75**, 132 (2015).
- [121] P. Skands, S. Carrazza, and J. Rojo, Tuning PYTHIA 8.1: The Monash 2013 tune, *Eur. Phys. J. C* **74**, 3024 (2014).
- [122] J. Bellm *et al.*, Herwig 7.2 release note, *Eur. Phys. J. C* **80**, 452 (2020).
- [123] ATLAS Collaboration, ATLAS computing acknowledgements, Report No. ATL-SOFT-PUB-2021-003, 2021, <https://cds.cern.ch/record/2776662>.

G. Aad¹⁰², B. Abbott¹²⁰, K. Abeling⁵⁵, S. H. Abidi²⁹, A. Abouhorma^{35e}, H. Abramowicz¹⁵¹, H. Abreu¹⁵⁰, Y. Abulaiti¹¹⁷, A. C. Abusleme Hoffman^{137a}, B. S. Acharya^{69a,69b,b}, C. Adam Bourdarios⁴, L. Adamczyk^{85a}, L. Adamek¹⁵⁵, S. V. Addepalli²⁶, J. Adelman¹¹⁵, A. Adiguzel^{21c}, S. Adorni⁵⁶, T. Adye¹³⁴, A. A. Affolder¹³⁶, Y. Afik³⁶, M. N. Agaras¹³, J. Agarwala^{73a,73b}, A. Aggarwal¹⁰⁰, C. Agheorghiesei^{27c}, J. A. Aguilar-Saavedra^{130f}, A. Ahmad³⁶, F. Ahmadov^{38,c}, W. S. Ahmed¹⁰⁴, S. Ahuja⁹⁵, X. Ai^{62a}, G. Aielli^{76a,76b}, M. Ait Tamlihat^{35e}, B. Aitbenchikh^{35a}, I. Aizenberg¹⁶⁸, M. Akbiyik¹⁰⁰, T. P. A. Åkesson⁹⁸, A. V. Akimov³⁷, D. Akiyama¹⁶⁷, N. N. Akolkar²⁴, K. Al Khoury⁴¹, G. L. Alberghi^{23b}, J. Albert¹⁶⁴, P. Albicocco⁵³, S. Alderweireldt⁵², M. Aleksa³⁶, I. N. Aleksandrov³⁸, C. Alexa^{27b}, T. Alexopoulos¹⁰, A. Alfonsi¹¹⁴, F. Alfonsi^{23b}, M. Alhroob¹²⁰, B. Ali¹³², S. Ali¹⁴⁸, M. Aliev³⁷, G. Alimonti^{71a}, W. Alkakhri⁵⁵, C. Allaire⁶⁶, B. M. M. Allbrooke¹⁴⁶, C. A. Allendes Flores^{137f}, P. P. Allport²⁰, A. Aloisio^{72a,72b}, F. Alonso⁹⁰, C. Alpigiani¹³⁸, M. Alvarez Estevez⁹⁹, A. Alvarez Fernandez¹⁰⁰, M. G. Alviggi^{72a,72b}, M. Aly¹⁰¹, Y. Amaral Coutinho^{82b}, A. Ambler¹⁰⁴, C. Amelung³⁶, M. Amerl¹⁰¹, C. G. Ames¹⁰⁹, D. Amidei¹⁰⁶, S. P. Amor Dos Santos^{130a}, K. R. Amos¹⁶², V. Ananiev¹²⁵, C. Anastopoulos¹³⁹, T. Andeen¹¹, J. K. Anders³⁶, S. Y. Andrean^{47a,47b}, A. Andreatza^{71a,71b}, S. Angelidakis⁹, A. Angerami^{41,d}, A. V. Anisenkov³⁷, A. Annovi^{74a}, C. Antel⁵⁶, M. T. Anthony¹³⁹, E. Antipov¹⁴⁵, M. Antonelli⁵³, D. J. A. Antrim^{17a}, F. Anulli^{75a}, M. Aoki⁸³, T. Aoki¹⁵³, J. A. Aparisi Pozo¹⁶², M. A. Aparo¹⁴⁶, L. Aperio Bella⁴⁸, C. Appelt¹⁸, N. Aranzabal³⁶, V. Araujo Ferraz^{82a}, C. Arcangeletti⁵³, A. T. H. Arce⁵¹, E. Arena⁹², J-F. Arguin¹⁰⁸, S. Argyropoulos⁵⁴, J.-H. Arling⁴⁸, A. J. Armbruster³⁶, O. Arnaez⁴, H. Arnold¹¹⁴, Z. P. Arrubarrena Tame¹⁰⁹, G. Artoni^{75a,75b}, H. Asada¹¹¹, K. Asai¹¹⁸, S. Asai¹⁵³, N. A. Asbah⁶¹, J. Assahsah^{35d}, K. Assamagan²⁹, R. Astalos^{28a}, R. J. Atkin^{33a}, M. Atkinson¹⁶¹, N. B. Atlay¹⁸, H. Atmani^{62b}, P. A. Atmasiddha¹⁰⁶, K. Augsten¹³², S. Auricchio^{72a,72b}, A. D. Aurioi²⁰, V. A. Austrup¹⁷⁰, G. Avner¹⁵⁰, G. Avolio³⁶, K. Axiotis⁵⁶, G. Azuelos^{108,e}, D. Babal^{28b}, H. Bachacou¹³⁵, K. Bachas^{152,f}, A. Bachi³⁴, F. Backman^{47a,47b}, A. Badea⁶¹, P. Bagnaia^{75a,75b}, M. Bahmani¹⁸, A. J. Bailey¹⁶², V. R. Bailey¹⁶¹, J. T. Baines¹³⁴, C. Bakalis¹⁰, O. K. Baker¹⁷¹, E. Bakos¹⁵, D. Bakshi Gupta⁸, R. Balasubramanian¹¹⁴, E. M. Baldin³⁷, P. Balek^{85a}, E. Ballabene^{71a,71b}, F. Balli¹³⁵, L. M. Baltes^{63a}, W. K. Balunas³², J. Balz¹⁰⁰, E. Banas⁸⁶, M. Bandieramonte¹²⁹, A. Bandyopadhyay²⁴, S. Bansal²⁴, L. Barak¹⁵¹, E. L. Barberio¹⁰⁵, D. Barberis^{57b,57a}, M. Barbero¹⁰², G. Barbour⁹⁶, K. N. Barends^{33a}, T. Barillari¹¹⁰, M-S. Barisits³⁶, T. Barklow¹⁴³, P. Baron¹²², D. A. Baron Moreno¹⁰¹, A. Baroncelli^{62a}, G. Barone²⁹, A. J. Barr¹²⁶, L. Barranco Navarro^{47a,47b}, F. Barreiro⁹⁹, J. Barreiro Guimarães da Costa^{14a}, U. Barron¹⁵¹, M. G. Barros Teixeira^{130a}, S. Barsov³⁷, F. Bartels^{63a}, R. Bartoldus¹⁴³, A. E. Barton⁹¹, P. Bartos^{28a}, A. Basan¹⁰⁰, M. Baselga⁴⁹, A. Bassalat^{66,gg}, M. J. Basso¹⁵⁵, C. R. Basson¹⁰¹, R. L. Bates⁵⁹, S. Batlamous^{35e}, J. R. Batley³², B. Batool¹⁴¹, M. Battaglia¹³⁶, D. Battulga¹⁸, M. Bauce^{75a,75b}, M. Bauer³⁶, P. Bauer²⁴, J. B. Beacham⁵¹, T. Beau¹²⁷, P. H. Beauchemin¹⁵⁸, F. Becherer⁵⁴, P. Bechtel²⁴, H. P. Beck^{19,g}, K. Becker¹⁶⁶, A. J. Beddall^{21d}, V. A. Bednyakov³⁸, C. P. Bee¹⁴⁵, L. J. Beemster¹⁵, T. A. Beermann³⁶, M. Begalli^{82d}, M. Begel²⁹, A. Behera¹⁴⁵, J. K. Behr⁴⁸, J. F. Beirer⁵⁵, F. Beisiegel²⁴, M. Belfkir^{116b}, G. Bella¹⁵¹, L. Bellagamba^{23b}, A. Bellerive³⁴, P. Bellos²⁰, K. Beloborodov³⁷, N. L. Belyaev³⁷, D. Benchevkroun^{35a}, F. Bendebba^{35a}, Y. Benhammou¹⁵¹, M. Benoit²⁹, J. R. Bensinger²⁶, S. Bentvelsen¹¹⁴, L. Beresford⁴⁸, M. Beretta⁵³, E. Bergeas Kuutmann¹⁶⁰, N. Berger⁴, B. Bergmann¹³², J. Beringer^{17a}, S. Berlendis⁷, G. Bernardi⁵, C. Bernius¹⁴³, F. U. Bernlochner²⁴, T. Berry⁹⁵, P. Berta¹³³, A. Berthold⁵⁰, I. A. Bertram⁹¹, S. Bethke¹¹⁰, A. Betti^{75a,75b}, A. J. Bevan⁹⁴, M. Bhamjee^{33c}, S. Bhatta¹⁴⁵, D. S. Bhattacharya¹⁶⁵, P. Bhattarai²⁶, V. S. Bhopatkar¹²¹, R. Bi^{29,h}, R. M. Bianchi¹²⁹, G. Bianco^{23b,23a}, O. Biebel¹⁰⁹, R. Bielski¹²³, M. Biglietti^{77a}, T. R. V. Billoud¹³², M. Bindi⁵⁵, A. Bingul^{21b}, C. Bini^{75a,75b}, A. Biondini⁹², C. J. Birch-sykes¹⁰¹, G. A. Bird^{20,134}, M. Birman¹⁶⁸, M. Biros¹³³, T. Bisanz³⁶, E. Bisceglie^{43b,43a}, D. Biswas¹⁶⁹, A. Bitadze¹⁰¹, K. Björke¹²⁵, I. Bloch⁴⁸, C. Blocker²⁶, A. Blue⁵⁹, U. Blumenschein⁹⁴, J. Blumenthal¹⁰⁰, G. J. Bobbink¹¹⁴, V. S. Bobrovnikov³⁷, M. Boehler⁵⁴, B. Boehm¹⁶⁵, D. Bogavac³⁶, A. G. Bogdanchikov³⁷, C. Bohm^{47a}, V. Boisvert⁹⁵, P. Bokal⁴⁸, T. Bold^{85a}, M. Bomben⁵, M. Bona⁹⁴, M. Boonekamp¹³⁵, C. D. Booth⁹⁵, A. G. Borbély⁵⁹, I. S. Bordulev³⁷, H. M. Borecka-Bielska¹⁰⁸, L. S. Borgna⁹⁶, G. Borissov⁹¹, D. Bortoletto¹²⁶, D. Boscherini^{23b}, M. Bosman¹³, J. D. Bossio Sola³⁶, K. Bouaouda^{35a}, N. Bouchhar¹⁶², J. Boudreau¹²⁹, E. V. Bouhova-Thacker⁹¹, D. Boumediene⁴⁰, R. Bouquet⁵, A. Boveia¹¹⁹, J. Boyd³⁶, D. Boye²⁹, I. R. Boyko³⁸, J. Bracinik²⁰, N. Brahimi^{62d}, G. Brandt¹⁷⁰, O. Brandt³², F. Braren⁴⁸, B. Brau¹⁰³, J. E. Brau¹²³, R. Brenner¹⁶⁸, L. Brenner¹¹⁴, R. Brenner¹⁶⁰, S. Bressler¹⁶⁸, D. Britton⁵⁹, D. Britzger¹¹⁰, I. Brock²⁴, G. Brooijmans⁴¹

W. K. Brooks^{137f} E. Brost²⁹ L. M. Brown¹⁶⁴ T. L. Bruckler¹²⁶ P. A. Bruckman de Renstrom⁸⁶ B. Brüers⁴⁸
D. Bruncko^{28b,a} A. Bruni^{23b} G. Bruni^{23b} M. Bruschi^{23b} N. Brusino^{75a,75b} T. Buanes¹⁶ Q. Buat¹³⁸
A. G. Buckley⁵⁹ I. A. Budagov^{38,a} M. K. Bugge¹²⁵ O. Bulekov³⁷ B. A. Bullard¹⁴³ S. Burdin⁹²
C. D. Burgard⁴⁹ A. M. Burger⁴⁰ B. Burghgrave⁸ O. Burlayenko⁵⁴ J. T. P. Burr³² C. D. Burton¹¹
J. C. Burzynski¹⁴² E. L. Busch⁴¹ V. Büscher¹⁰⁰ P. J. Bussey⁵⁹ J. M. Butler²⁵ C. M. Buttar⁵⁹
J. M. Butterworth⁹⁶ W. Buttinger¹³⁴ C. J. Buxo Vazquez¹⁰⁷ A. R. Buzykaev³⁷ G. Cabras^{23b} S. Cabrera Urbán¹⁶²
D. Caforio⁵⁸ H. Cai¹²⁹ Y. Cai^{14a,14e} V. M. M. Cairo³⁶ O. Cakir^{3a} N. Calace³⁶ P. Calafiura^{17a}
G. Calderini¹²⁷ P. Calfayan⁶⁸ G. Callea⁵⁹ L. P. Caloba^{82b} D. Calvet⁴⁰ S. Calvet⁴⁰ T. P. Calvet¹⁰²
M. Calvetti^{74a,74b} R. Camacho Toro¹²⁷ S. Camarda³⁶ D. Camarero Munoz²⁶ P. Camarri^{76a,76b}
M. T. Camerlingo^{72a,72b} D. Cameron¹²⁵ C. Camincher¹⁶⁴ M. Campanelli⁹⁶ A. Camplani⁴² V. Canale^{72a,72b}
A. Canesse¹⁰⁴ M. Cano Bret⁸⁰ J. Cantero¹⁶² Y. Cao¹⁶¹ F. Capocasa²⁶ M. Capua^{43b,43a} A. Carbone^{71a,71b}
R. Cardarelli^{76a} J. C. J. Cardenas⁸ F. Cardillo¹⁶² T. Carli³⁶ G. Carlino^{72a} J. I. Carlotto¹³ B. T. Carlson^{129,i}
E. M. Carlson^{164,156a} L. Carminati^{71a,71b} M. Carnesale^{75a,75b} S. Caron¹¹³ E. Carquin^{137f} S. Carrá^{71a,71b}
G. Carratta^{23b,23a} F. Carrio Argos^{33g} J. W. S. Carter¹⁵⁵ T. M. Carter⁵² M. P. Casado^{13j} A. F. Casha¹⁵⁵
M. Caspar⁴⁸ E. G. Castiglia¹⁷¹ F. L. Castillo^{63a} L. Castillo Garcia¹³ V. Castillo Gimenez¹⁶² N. F. Castro^{130a,130e}
A. Catinaccio³⁶ J. R. Catmore¹²⁵ V. Cavaliere²⁹ N. Cavalli^{23b,23a} V. Cavasinni^{74a,74b} Y. C. Cekmecelioglu⁴⁸
E. Celebi^{21a} F. Celli¹²⁶ M. S. Centonze^{70a,70b} K. Cerny¹²² A. S. Cerqueira^{82a} A. Cerri¹⁴⁶ L. Cerrito^{76a,76b}
F. Cerutti^{17a} B. Cervato¹⁴¹ A. Cervelli^{23b} G. Cesarini⁵³ S. A. Cetin^{21d} Z. Chadi^{35a} D. Chakraborty¹¹⁵
M. Chala^{130f} J. Chan¹⁶⁹ W. Y. Chan¹⁵³ J. D. Chapman³² B. Chargeishvili^{149b} D. G. Charlton²⁰
T. P. Charman⁹⁴ M. Chatterjee¹⁹ C. Chauhan¹³³ S. Chekanov⁶ S. V. Chekulaev^{156a} G. A. Chelkov^{38,k}
A. Chen¹⁰⁶ B. Chen¹⁵¹ B. Chen¹⁶⁴ H. Chen^{14c} H. Chen²⁹ J. Chen^{62c} J. Chen¹⁴² S. Chen¹⁵³ S. J. Chen^{14c}
X. Chen^{62c} X. Chen^{14b,l} Y. Chen^{62a} C. L. Cheng¹⁶⁹ H. C. Cheng^{64a} S. Cheong¹⁴³ A. Cheplakov³⁸
E. Cheremushkina⁴⁸ E. Cherepanova¹¹⁴ R. Cherkaoui El Moursli^{35e} E. Cheu⁷ K. Cheung⁶⁵ L. Chevalier¹³⁵
V. Chiarella⁵³ G. Chiarelli^{74a} N. Chiedde¹⁰² G. Chiodini^{70a} A. S. Chisholm²⁰ A. Chitan^{27b} M. Chitishvili¹⁶²
M. V. Chizhov³⁸ K. Choi¹¹ A. R. Chomont^{75a,75b} Y. Chou¹⁰³ E. Y. S. Chow¹¹⁴ T. Chowdhury^{33g}
L. D. Christopher^{33g} K. L. Chu¹⁶⁸ M. C. Chu^{64a} X. Chu^{14a,14e} J. Chudoba¹³¹ J. J. Chwastowski⁸⁶ D. Cieri¹¹⁰
K. M. Ciesla^{85a} V. Cindro⁹³ A. Ciocio^{17a} F. Ciroto^{72a,72b} Z. H. Citron^{168,II} M. Citterio^{71a} D. A. Ciubotaru^{27b}
B. M. Ciungu¹⁵⁵ A. Clark³⁶ P. J. Clark⁵² J. M. Clavijo Columbie⁴⁸ S. E. Clawson¹⁰¹ C. Clement^{47a,47b}
J. Clercx⁴⁸ L. Clissa^{23b,23a} Y. Coadou¹⁰² M. Cobal^{69a,69c} A. Coccaro^{57b} R. F. Coelho Barrue^{130a}
R. Coelho Lopes De Sa¹⁰³ S. Coelli^{71a} H. Cohen¹⁵¹ A. E. C. Coimbra^{71a,71b} B. Cole⁴¹ J. Collot⁶⁰
P. Conde Muñio^{130a,130g} M. P. Connell^{33c} S. H. Connell^{33c} I. A. Connelly⁵⁹ E. I. Conroy¹²⁶ F. Conventi^{72a,m}
H. G. Cooke²⁰ A. M. Cooper-Sarkar¹²⁶ F. Cormier¹⁶³ L. D. Corpe³⁶ M. Corradi^{75a,75b} F. Corriveau^{104,n}
A. Cortes-Gonzalez¹⁸ M. J. Costa¹⁶² F. Costanza⁴ D. Costanzo¹³⁹ B. M. Cote¹¹⁹ G. Cowan⁹⁵ K. Cranmer¹¹⁷
D. Cremonini^{23b,23a} S. Crépe-Renaudin⁶⁰ F. Crescioli¹²⁷ M. Cristinziani¹⁴¹ M. Cristoforetti^{78a,78b,o} V. Croft¹¹⁴
J. E. Crosby¹²¹ G. Crosetti^{43b,43a} A. Cueto³⁶ T. Cuhadar Donszelmann¹⁵⁹ H. Cui^{14a,14e} Z. Cui⁷
W. R. Cunningham⁵⁹ F. Curcio^{43b,43a} P. Czodrowski³⁶ M. M. Czurylo^{63b} M. J. Da Cunha Sargedas De Sousa^{62a}
J. V. Da Fonseca Pinto^{82b} C. Da Via¹⁰¹ W. Dabrowski^{85a} T. Dado⁴⁹ S. Dahbi^{33g} T. Dai¹⁰⁶ C. Dallapiccola¹⁰³
M. Dam⁴² G. D'amen²⁹ V. D'Amico¹⁰⁹ J. Damp¹⁰⁰ J. R. Dandoy¹²⁸ M. F. Daneri³⁰ M. Danninger¹⁴²
V. Dao³⁶ G. Darbo^{57b} S. Darmora⁶ S. J. Das²⁹ S. D'Auria^{71a,71b} C. David^{156b} T. Davidek¹³³
B. Davis-Purcell³⁴ I. Dawson⁹⁴ K. De⁸ R. De Asmundis^{72a} N. De Biase⁴⁸ S. De Castro^{23b,23a} N. De Groot¹¹³
P. de Jong¹¹⁴ H. De la Torre¹⁰⁷ A. De Maria^{14c} A. De Salvo^{75a} U. De Sanctis^{76a,76b} A. De Santo¹⁴⁶
J. B. De Vivie De Regie⁶⁰ D. V. Dedovich³⁸ J. Degens¹¹⁴ A. M. Deiana⁴⁴ F. Del Corso^{23b,23a} J. Del Peso⁹⁹
F. Del Rio^{63a} F. Deliot¹³⁵ C. M. Delitzsch⁴⁹ M. Della Pietra^{72a,72b} D. Della Volpe⁵⁶ A. Dell'Acqua³⁶
L. Dell'Asta^{71a,71b} M. Delmastro⁴ P. A. Delsart⁶⁰ S. Demers¹⁷¹ M. Demichev³⁸ S. P. Denisov³⁷
L. D'Eramo¹¹⁵ D. Derendarz⁸⁶ F. Derue¹²⁷ P. Dervan⁹² K. Desch²⁴ K. Dette¹⁵⁵ C. Deutsch²⁴
F. A. Di Bello^{57b,57a} A. Di Ciaccio^{76a,76b} L. Di Ciaccio⁴ A. Di Domenico^{75a,75b} C. Di Donato^{72a,72b}
A. Di Girolamo³⁶ G. Di Gregorio⁵ A. Di Luca^{78a,78b} B. Di Micco^{77a,77b} R. Di Nardo^{77a,77b} C. Diaconu¹⁰²
F. A. Dias¹¹⁴ T. Dias Do Vale¹⁴² M. A. Diaz^{137a,137b} F. G. Diaz Capriles²⁴ M. Didenko¹⁶² E. B. Diehl¹⁰⁶
L. Diehl⁵⁴ S. Díez Cornell⁴⁸ C. Diez Pardos¹⁴¹ C. Dimitriadi^{24,160} A. Dimitrievska^{17a} J. Dingfelder²⁴

I-M. Dinu^{27b}, S. J. Dittmeier^{63b}, F. Dittus³⁶, F. Djama¹⁰², T. Djobava^{149b}, J. I. Djuvslund¹⁶, C. Doglioni^{101,98}, J. Dolejsi¹³³, Z. Dolezal¹³³, M. Donadelli^{82c}, B. Dong¹⁰⁷, J. Donini⁴⁰, A. D'Onofrio^{77a,77b}, M. D'Onofrio⁹², J. Dopke¹³⁴, A. Doria^{72a}, M. T. Dova⁹⁰, A. T. Doyle⁵⁹, M. A. Draguet¹²⁶, E. Drechsler¹⁴², E. Dreyer¹⁶⁸, I. Drivas-koulouris¹⁰, A. S. Drobac¹⁵⁸, M. Drozdova⁵⁶, D. Du^{62a}, T. A. du Pree¹¹⁴, F. Dubinin³⁷, M. Dubovsky^{28a}, E. Duchovni¹⁶⁸, G. Duckeck¹⁰⁹, O. A. Ducu^{27b}, D. Duda¹¹⁰, A. Dudarev³⁶, E. R. Duden²⁶, M. D'uffizi¹⁰¹, L. Dufлот⁶⁶, M. Dührssen³⁶, C. Dülsen¹⁷⁰, A. E. Dumitriu^{27b}, M. Dunford^{63a}, S. Dungs⁴⁹, K. Dunne^{47a,47b}, A. Duperrin¹⁰², H. Duran Yildiz^{3a}, M. Düren⁵⁸, A. Durglishvili^{149b}, B. L. Dwyer¹¹⁵, G. I. Dyckes^{17a}, M. Dyndal^{85a}, S. Dysch¹⁰¹, B. S. Dziedzic⁸⁶, Z. O. Earnshaw¹⁴⁶, G. H. Eberwein¹²⁶, B. Eckerova^{28a}, S. Eggebrecht⁵⁵, M. G. Eggleston⁵¹, E. Egidio Purcino De Souza¹²⁷, L. F. Ehrke⁵⁶, G. Eigen¹⁶, K. Einsweiler^{17a}, T. Ekelof¹⁶⁰, P. A. Ekman⁹⁸, Y. El Ghazali^{35b}, H. El Jarrari^{35e,148}, A. El Moussaouy^{35a}, V. Ellajosyula¹⁶⁰, M. Ellert¹⁶⁰, F. Ellinghaus¹⁷⁰, A. A. Elliot⁹⁴, N. Ellis³⁶, J. Elmsheuser²⁹, M. Elsing³⁶, D. Emelianov¹³⁴, Y. Enari¹⁵³, I. Ene^{17a}, S. Epari¹³, J. Erdmann⁴⁹, P. A. Erland⁸⁶, M. Errenst¹⁷⁰, M. Escalier⁶⁶, C. Escobar¹⁶², E. Etzion¹⁵¹, G. Evans^{130a}, H. Evans⁶⁸, L. S. Evans⁹⁵, M. O. Evans¹⁴⁶, A. Ezhilov³⁷, S. Ezzarqtouni^{35a}, F. Fabbri⁵⁹, L. Fabbri^{23b,23a}, G. Facini⁹⁶, V. Fadeyev¹³⁶, R. M. Fakhrutdinov³⁷, S. Falciano^{75a}, L. F. Falda Ulhoa Coelho³⁶, P. J. Falke²⁴, J. Faltova¹³³, C. Fan¹⁶¹, Y. Fan^{14a}, Y. Fang^{14a,14e}, M. Fanti^{71a,71b}, M. Faraj^{69a,69b}, Z. Farazpay⁹⁷, A. Farbin⁸, A. Farilla^{77a}, T. Farooque¹⁰⁷, S. M. Farrington⁵², F. Fassi^{35e}, D. Fassouliotis⁹, M. Fauci Giannelli^{76a,76b}, W. J. Fawcett³², L. Fayard⁶⁶, P. Federic¹³³, P. Federicova¹³¹, O. L. Fedin^{37,k}, G. Fedotov³⁷, M. Feickert¹⁶⁹, L. Feligioni¹⁰², A. Fell¹³⁹, D. E. Fellers¹²³, C. Feng^{62b}, M. Feng^{14b}, Z. Feng¹¹⁴, M. J. Fenton¹⁵⁹, A. B. Fenyuk³⁷, L. Ferencz⁴⁸, R. A. M. Ferguson⁹¹, S. I. Fernandez Luengo^{137f}, M. J. V. Fernoux¹⁰², J. Ferrando⁴⁸, A. Ferrari¹⁶⁰, P. Ferrari^{114,113}, R. Ferrari^{73a}, D. Ferrere⁵⁶, C. Ferretti¹⁰⁶, F. Fiedler¹⁰⁰, A. Filipčić⁹³, E. K. Filmer¹, F. Filthaut¹¹³, M. C. N. Fiolhais^{130a,130c,p}, L. Fiorini¹⁶², W. C. Fisher¹⁰⁷, T. Fitschen¹⁰¹, P. M. Fitzhugh¹³⁵, I. Fleck¹⁴¹, P. Fleischmann¹⁰⁶, T. Flick¹⁷⁰, L. Flores¹²⁸, M. Flores^{33d,ii}, L. R. Flores Castillo^{64a}, F. M. Follega^{78a,78b}, N. Fomin¹⁶, J. H. Foo¹⁵⁵, B. C. Forland⁶⁸, A. Formica¹³⁵, A. C. Forti¹⁰¹, E. Fortin³⁶, A. W. Fortman⁶¹, M. G. Foti^{17a}, L. Fountas⁹, D. Fournier⁶⁶, H. Fox⁹¹, P. Francavilla^{74a,74b}, S. Francescato⁶¹, S. Franchellucci⁵⁶, M. Franchini^{23b,23a}, S. Franchino^{63a}, D. Francis³⁶, L. Franco¹¹³, L. Franconi⁴⁸, M. Franklin⁶¹, G. Frattari²⁶, A. C. Freegard⁹⁴, W. S. Freund^{82b}, Y. Y. Frid¹⁵¹, N. Fritzsche⁵⁰, A. Froch⁵⁴, D. Froidevaux³⁶, J. A. Frost¹²⁶, Y. Fu^{62a}, M. Fujimoto¹¹⁸, E. Fullana Torregrosa^{162a}, E. Furtado De Simas Filho^{82b}, J. Fuster¹⁶², A. Gabrielli^{23b,23a}, A. Gabrielli¹⁵⁵, P. Gadow⁴⁸, G. Gagliardi^{57b,57a}, L. G. Gagnon^{17a}, E. J. Gallas¹²⁶, B. J. Gallop¹³⁴, K. K. Gan¹¹⁹, S. Ganguly¹⁵³, J. Gao^{62a}, Y. Gao⁵², F. M. Garay Walls^{137a,137b}, B. Garcia^{29,h}, C. García¹⁶², A. Garcia Alonso¹¹⁴, A. G. Garcia Caffaro¹⁷¹, J. E. García Navarro¹⁶², M. Garcia-Sciveres^{17a}, R. W. Gardner³⁹, D. Garg⁸⁰, R. B. Garg^{143,mm}, C. A. Garner¹⁵⁵, S. J. Gasiorowski¹³⁸, P. Gaspar^{82b}, G. Gaudio^{73a}, V. Gautam¹³, P. Gauzzi^{75a,75b}, I. L. Gavrilenko³⁷, A. Gavrilyuk³⁷, C. Gay¹⁶³, G. Gaycken⁴⁸, E. N. Gazis¹⁰, A. A. Geanta^{27b,27e}, C. M. Gee¹³⁶, C. Gemme^{57b}, M. H. Genest⁶⁰, S. Gentile^{75a,75b}, S. George⁹⁵, W. F. George²⁰, T. Geralis⁴⁶, L. O. Gerlach⁵⁵, P. Gessinger-Befurt³⁶, M. E. Geyik¹⁷⁰, M. Ghneimat¹⁴¹, K. Ghorbanian⁹⁴, A. Ghosal¹⁴¹, A. Ghosh¹⁵⁹, A. Ghosh⁷, B. Giacobbe^{23b}, S. Giagu^{75a,75b}, P. Giannetti^{74a}, A. Giannini^{62a}, S. M. Gibson⁹⁵, M. Gignac¹³⁶, D. T. Gil^{85b}, A. K. Gilbert^{85a}, B. J. Gilbert⁴¹, D. Gillberg³⁴, G. Gilles¹¹⁴, N. E. K. Gillwald⁴⁸, L. Ginabat¹²⁷, D. M. Gingrich^{2,e}, M. P. Giordani^{69a,69c}, P. F. Giraud¹³⁵, G. Giugliarelli^{69a,69c}, D. Giugni^{71a}, F. Giuli³⁶, I. Gkialas^{9,q}, L. K. Gladilin³⁷, C. Glasman⁹⁹, G. R. Gledhill¹²³, M. Glisic¹²³, I. Gnesi^{43b,r}, Y. Go^{29,h}, M. Goblirsch-Kolb³⁶, B. Gocke⁴⁹, D. Godin¹⁰⁸, B. Gokturk^{21a}, S. Goldfarb¹⁰⁵, T. Golling⁵⁶, M. G. D. Gololo^{33g}, D. Golubkov³⁷, J. P. Gombas¹⁰⁷, A. Gomes^{130a,130b}, G. Gomes Da Silva¹⁴¹, A. J. Gomez Delegido¹⁶², R. Gonçalves^{130a,130c}, G. Gonella¹²³, L. Gonella²⁰, A. Gongadze³⁸, F. Gonnella²⁰, J. L. Gonski⁴¹, S. González de la Hoz¹⁶², S. Gonzalez Fernandez¹³, R. Gonzalez Lopez⁹², C. Gonzalez Renteria^{17a}, R. Gonzalez Suarez¹⁶⁰, S. Gonzalez-Sevilla⁵⁶, G. R. Gonzalvo Rodriguez¹⁶², R. Y. González Andana⁵², L. Goossens³⁶, P. A. Gorbounov³⁷, B. Gorini³⁶, E. Gorini^{70a,70b}, A. Gorišek⁹³, T. C. Gosart¹²⁸, A. T. Goshaw⁵¹, M. I. Gostkin³⁸, S. Goswami¹²¹, C. A. Gottardo³⁶, M. Gouighri^{35b}, V. Goumarre⁴⁸, A. G. Goussiou¹³⁸, N. Govender^{33c}, I. Grabowska-Bold^{85a}, K. Graham³⁴, E. Gramstad¹²⁵, S. Grancagnolo^{70a,70b}, M. Grandi¹⁴⁶, V. Gratchev^{37,a}, P. M. Gravila^{27f}, F. G. Gravili^{70a,70b}, H. M. Gray^{17a}, M. Greco^{70a,70b}, C. Greife²⁴, I. M. Gregor⁴⁸, P. Grenier¹⁴³, C. Grieco¹³, A. A. Grillo¹³⁶, K. Grimm^{31,s}, S. Grinstein^{13,t}, J.-F. Grivaz⁶⁶, E. Gross¹⁶⁸

J. Grosse-Knetter⁵⁵ C. Grud,¹⁰⁶ J. C. Grundy¹²⁶ L. Guan¹⁰⁶ W. Guan¹⁶⁹ C. Gubbels¹⁶³
 J. G. R. Guerrero Rojas¹⁶² G. Guerrieri^{69a,69b} F. Guescini¹¹⁰ R. Gugel¹⁰⁰ J. A. M. Guhit¹⁰⁶ A. Guida⁴⁸
 T. Guillemain⁴ E. Guilloton^{166,134} S. Guindon³⁶ F. Guo^{14a,14e} J. Guo^{62c} L. Guo⁶⁶ Y. Guo¹⁰⁶ R. Gupta⁴⁸
 S. Gurbuz²⁴ S. S. Gurdasani⁵⁴ G. Gustavino³⁶ M. Guth⁵⁶ P. Gutierrez¹²⁰ L. F. Gutierrez Zagazeta¹²⁸
 C. Gutschow⁹⁶ C. Gwenlan¹²⁶ C. B. Gwilliam⁹² E. S. Haaland¹²⁵ A. Haas¹¹⁷ M. Habedank⁴⁸ C. Haber^{17a}
 H. K. Hadavand⁸ A. Hadeef¹⁰⁰ S. Hadzic¹¹⁰ J. J. Hahn¹⁴¹ E. H. Haines⁹⁶ M. Haleem¹⁶⁵ J. Haley¹²¹
 J. J. Hall¹³⁹ G. D. Hallowell¹⁰² L. Halser¹⁹ K. Hamano¹⁶⁴ H. Hamdaoui^{35e} M. Hamer²⁴ G. N. Hamity⁵²
 E. J. Hampshire⁹⁵ J. Han^{62b} K. Han^{62a} L. Han^{14c} L. Han^{62a} S. Han^{17a} Y. F. Han¹⁵⁵ K. Hanagaki⁸³
 M. Hance¹³⁶ D. A. Hangal^{41,d} H. Hanif¹⁴² M. D. Hank¹²⁸ R. Hankache¹⁰¹ J. B. Hansen⁴² J. D. Hansen⁴²
 P. H. Hansen⁴² K. Hara¹⁵⁷ D. Harada⁵⁶ T. Harenberg¹⁷⁰ S. Harkusha³⁷ Y. T. Harris¹²⁶ N. M. Harrison¹¹⁹
 P. F. Harrison¹⁶⁶ N. M. Hartman¹⁴³ N. M. Hartmann¹⁰⁹ Y. Hasegawa¹⁴⁰ A. Hasib⁵² S. Haug¹⁹ R. Hauser¹⁰⁷
 M. Havranek¹³² C. M. Hawkes²⁰ R. J. Hawkins³⁶ Y. Hayashi¹⁵³ S. Hayashida¹¹¹ D. Hayden¹⁰⁷
 C. Hayes¹⁰⁶ R. L. Hayes¹¹⁴ C. P. Hays¹²⁶ J. M. Hays⁹⁴ H. S. Hayward⁹² F. He^{62a} Y. He¹⁵⁴ Y. He¹²⁷
 N. B. Heatley⁹⁴ V. Hedberg⁹⁸ A. L. Heggelund¹²⁵ N. D. Hehir⁹⁴ C. Heidegger⁵⁴ K. K. Heidegger⁵⁴
 W. D. Heidorn⁸¹ J. Heilmann³⁴ S. Heim⁴⁸ T. Heim^{17a} J. G. Heinlein¹²⁸ J. J. Heinrich¹²³ L. Heinrich^{110,jj}
 J. Hejbal¹³¹ L. Helary⁴⁸ A. Held¹⁶⁹ S. Hellesund¹⁶ C. M. Helling¹⁶³ S. Hellman^{47a,47b} C. Helsens³⁶
 R. C. W. Henderson⁹¹ L. Henkelmann³² A. M. Henriques Correia³⁶ H. Herde⁹⁸ Y. Hernández Jiménez¹⁴⁵
 L. M. Herrmann²⁴ T. Herrmann⁵⁰ G. Hertel⁵⁴ R. Hertenberger¹⁰⁹ L. Hervas³⁶ N. P. Hessey^{156a} H. Hibi⁸⁴
 S. J. Hillier²⁰ F. Hinterkeuser²⁴ M. Hirose¹²⁴ S. Hirose¹⁵⁷ D. Hirschbuehl¹⁷⁰ T. G. Hitchings¹⁰¹ B. Hiti⁹³
 J. Hobbs¹⁴⁵ R. Hobincu^{27e} N. Hod¹⁶⁸ M. C. Hodgkinson¹³⁹ B. H. Hodgkinson³² A. Hoecker³⁶ J. Hofer⁴⁸
 T. Holm²⁴ M. Holzbock¹¹⁰ L. B. A. H. Hommels³² B. P. Honan¹⁰¹ J. Hong^{62c} T. M. Hong¹²⁹ J. C. Honig⁵⁴
 B. H. Hooberman¹⁶¹ W. H. Hopkins⁶ Y. Horii¹¹¹ S. Hou¹⁴⁸ A. S. Howard⁹³ J. Howarth⁵⁹ J. Hoya⁶
 M. Hrabovsky¹²² A. Hrynevich⁴⁸ T. Hryn'ova⁴ P. J. Hsu⁶⁵ S.-C. Hsu¹³⁸ Q. Hu⁴¹ Y. F. Hu^{14a,14e}
 D. P. Huang⁹⁶ S. Huang^{64b} X. Huang^{14c} Y. Huang^{62a} Y. Huang^{14a} Z. Huang¹⁰¹ Z. Hubacek¹³²
 M. Huebner²⁴ F. Hugging²⁴ T. B. Huffman¹²⁶ C. A. Hugli⁴⁸ M. Huhtinen³⁶ S. K. Huiberts¹⁶ R. Hulsken¹⁰⁴
 N. Huseynov^{12,k} J. Huston¹⁰⁷ J. Huth⁶¹ R. Hyneman¹⁴³ G. Iacobucci⁵⁶ G. Iakovidis²⁹ I. Ibragimov¹⁴¹
 L. Iconomidou-Fayard⁶⁶ P. Iengo^{72a,72b} R. Iguchi¹⁵³ T. Iizawa⁵⁶ Y. Ikegami⁸³ A. Ilg¹⁹ N. Ilic¹⁵⁵
 H. Imam^{35a} T. Ingebretsen Carlson^{47a,47b} G. Introzzi^{73a,73b} M. Iodice^{77a} V. Ippolito^{75a,75b} M. Ishino¹⁵³
 W. Islam¹⁶⁹ C. Issever^{18,48} S. Istin^{21a,kk} H. Ito¹⁶⁷ J. M. Iturbe Ponce^{64a} R. Iuppa^{78a,78b} A. Ivina¹⁶⁸
 J. M. Izen⁴⁵ V. Izzo^{72a} P. Jacka^{131,132} P. Jackson¹ R. M. Jacobs⁴⁸ B. P. Jaeger¹⁴² C. S. Jagfeld¹⁰⁹ P. Jain⁵⁴
 G. Jäkel¹⁷⁰ K. Jakobs⁵⁴ T. Jakoubek¹⁶⁸ J. Jamieson⁵⁹ K. W. Janas^{85a} A. E. Janspan⁹² M. Javurkova¹⁰³
 F. Jeanneau¹³⁵ L. Jeanty¹²³ J. Jelkava^{149a,u} P. Jenni^{54,v} C. E. Jessiman³⁴ S. Jézéquel⁴ C. Jia^{62b} J. Jia¹⁴⁵
 X. Jia⁶¹ X. Jia^{14a,14e} Z. Jia^{14c} Y. Jiang^{62a} S. Jiggins⁴⁸ J. Jimenez Pena¹¹⁰ S. Jin^{14c} A. Jinaru^{27b}
 O. Jinnouchi¹⁵⁴ P. Johansson¹³⁹ K. A. Johns⁷ J. W. Johnson¹³⁶ D. M. Jones³² E. Jones⁴⁸ P. Jones³²
 R. W. L. Jones⁹¹ T. J. Jones⁹² R. Joshi¹¹⁹ J. Jovicevic¹⁵ X. Ju^{17a} J. J. Junggeburth³⁶ T. Junkermann^{63a}
 A. Juste Rozas^{13,t} S. Kabana^{137e} A. Kaczmarska⁸⁶ M. Kado¹¹⁰ H. Kagan¹¹⁹ M. Kagan¹⁴³ A. Kahn⁴¹
 A. Kahn¹²⁸ C. Kahra¹⁰⁰ T. Kaji¹⁶⁷ E. Kajomovitz¹⁵⁰ N. Kakati¹⁶⁸ C. W. Kalderon²⁹ A. Kamenshchikov¹⁵⁵
 S. Kanayama¹⁵⁴ N. J. Kang¹³⁶ D. Kar^{33g} K. Karava¹²⁶ M. J. Kareem^{156b} E. Karentzos⁵⁴ I. Karkanias^{152,w}
 S. N. Karpov³⁸ Z. M. Karpova³⁸ V. Kartvelishvili⁹¹ A. N. Karyukhin³⁷ E. Kasimi^{152,w} J. Katzy⁴⁸ S. Kaur³⁴
 K. Kawade¹⁴⁰ T. Kawamoto¹³⁵ E. F. Kay³⁶ F. I. Kaya¹⁵⁸ S. Kazakos¹³ V. F. Kazanin³⁷ Y. Ke¹⁴⁵
 J. M. Keaveney^{33a} R. Keeler¹⁶⁴ G. V. Kehris⁶¹ J. S. Keller³⁴ A. S. Kelly⁹⁶ D. Kelsey¹⁴⁶ J. J. Kempster¹⁴⁶
 K. E. Kennedy⁴¹ P. D. Kennedy¹⁰⁰ O. Kepka¹³¹ B. P. Kerridge¹⁶⁶ S. Kersten¹⁷⁰ B. P. Kerševan⁹³ S. Keshri⁶⁶
 L. Keszeghova^{28a} S. Ketabchi Haghghat¹⁵⁵ M. Khandoga¹²⁷ A. Khanov¹²¹ A. G. Kharlamov³⁷
 T. Kharlamova³⁷ E. E. Khoda¹³⁸ T. J. Khoo¹⁸ G. Khoriali¹⁶⁵ J. Khubua^{149b} Y. A. R. Khwaira⁶⁶ M. Kiehn³⁶
 A. Kilgallon¹²³ D. W. Kim^{47a,47b} Y. K. Kim³⁹ N. Kimura⁹⁶ A. Kirchhoff⁵⁵ C. Kirfel²⁴ J. Kirk¹³⁴
 A. E. Kiryunin¹¹⁰ T. Kishimoto¹⁵³ D. P. Kisluk¹⁵⁵ C. Kitsaki¹⁰ O. Kivernyk²⁴ M. Klassen^{63a} C. Klein³⁴
 L. Klein¹⁶⁵ M. H. Klein¹⁰⁶ M. Klein⁹² S. B. Klein⁵⁶ U. Klein⁹² P. Klimek³⁶ A. Klimentov²⁹
 T. Klioutchnikova³⁶ P. Kluit¹¹⁴ S. Kluth¹¹⁰ E. Kneringer⁷⁹ T. M. Knight¹⁵⁵ A. Knue⁵⁴ R. Kobayashi⁸⁷
 M. Kocian¹⁴³ P. Kodyš¹³³ D. M. Koeck¹²³ P. T. Koenig²⁴ T. Koffas³⁴ M. Kolb¹³⁵ I. Koletsou⁴

T. Komarek¹²² K. Köneke⁵⁴ A. X. Y. Kong¹ T. Kono¹¹⁸ N. Konstantinidis⁹⁶ B. Konya⁹⁸ R. Kopeliansky⁶⁸
S. Koperny^{85a} K. Korcyl⁸⁶ K. Kordas^{152,w} G. Koren¹⁵¹ A. Korn⁹⁶ S. Korn⁵⁵ I. Korolkov¹³ N. Korotkova³⁷
B. Kortman¹¹⁴ O. Kortner¹¹⁰ S. Kortner¹¹⁰ W. H. Kostecka¹¹⁵ V. V. Kostyukhin¹⁴¹ A. Kotsokechagia¹³⁵
A. Kotwal⁵¹ A. Koulouris³⁶ A. Kourkoumeli-Charalampidi^{73a,73b} C. Kourkoumelis⁹ E. Kourlitis⁶
O. Kovanda¹⁴⁶ R. Kowalewski¹⁶⁴ W. Kozanecki¹³⁵ A. S. Kozhin³⁷ V. A. Kramarenko³⁷ G. Kramberger⁹³
P. Kramer¹⁰⁰ M. W. Krasny¹²⁷ A. Krasznahorkay³⁶ J. A. Kremer¹⁰⁰ T. Kresse⁵⁰ J. Kretzschmar⁹² K. Kreul¹⁸
P. Krieger¹⁵⁵ S. Krishnamurthy¹⁰³ M. Krivos¹³³ K. Krizka²⁰ K. Kroeninger⁴⁹ H. Kroha¹¹⁰ J. Kroll¹³¹
J. Kroll¹²⁸ K. S. Krowpman¹⁰⁷ U. Kruchonak³⁸ H. Krüger²⁴ N. Krumnack⁸¹ M. C. Kruse⁵¹ J. A. Krzysiak⁸⁶
O. Kuchinskaia³⁷ S. Kuday^{3a} S. Kuehn³⁶ R. Kuesters⁵⁴ T. Kuhl⁴⁸ V. Kukhtin³⁸ Y. Kulchitsky^{37,k}
S. Kuleshov^{137d,137b} M. Kumar^{33g} N. Kumari¹⁰² A. Kupco¹³¹ T. Kupfer⁴⁹ A. Kupich³⁷ O. Kuprash⁵⁴
H. Kurashige⁸⁴ L. L. Kurchaninov^{156a} O. Kurdysh⁶⁶ Y. A. Kurochkin³⁷ A. Kurova³⁷ M. Kuze¹⁵⁴
A. K. Kvam¹⁰³ J. Kvita¹²² T. Kwan¹⁰⁴ N. G. Kyriacou¹⁰⁶ L. A. O. Laatu¹⁰² C. Lacasta¹⁶² F. Lacava^{75a,75b}
H. Lacker¹⁸ D. Lacour¹²⁷ N. N. Lad⁹⁶ E. Ladygin³⁸ B. Laforge¹²⁷ T. Lagouri^{137e} S. Lai⁵⁵
I. K. Lakomic^{85a} N. Lalloue⁶⁰ J. E. Lambert¹²⁰ S. Lammers⁶⁸ W. Lampl⁷ C. Lampoudis^{152,w}
A. N. Lancaster¹¹⁵ E. Lançon²⁹ U. Landgraf⁵⁴ M. P. J. Landon⁹⁴ V. S. Lang⁵⁴ R. J. Langenberg¹⁰³
O. K. B. Langrekken¹²⁵ A. J. Lankford¹⁵⁹ F. Lanni³⁶ K. Lantzsch²⁴ A. Lanza^{73a} A. Lapertosa^{57b,57a}
J. F. Laporte¹³⁵ T. Lari^{71a} F. Lasagni Manghi^{23b} M. Lassnig³⁶ V. Latonova¹³¹ A. Laudrain¹⁰⁰ A. Laurier¹⁵⁰
S. D. Lawlor⁹⁵ Z. Lawrence¹⁰¹ M. Lazzaroni^{71a,71b} B. Le¹⁰¹ E. M. Le Boulicaut⁵¹ B. Leban⁹³ A. Lebedev⁸¹
M. LeBlanc³⁶ F. Ledroit-Guillon⁶⁰ A. C. A. Lee⁹⁶ G. R. Lee¹⁶ S. C. Lee¹⁴⁸ S. Lee^{47a,47b} T. F. Lee⁹²
L. L. Leeuw^{33c} H. P. Lefebvre⁹⁵ M. Lefebvre¹⁶⁴ C. Leggett^{17a} K. Lehmann¹⁴² G. Lehmann Miotto³⁶
M. Leigh⁵⁶ W. A. Leight¹⁰³ A. Leisos^{152,x} M. A. L. Leite^{82c} C. E. Leitgeb⁴⁸ R. Leitner¹³³ K. J. C. Leney⁴⁴
T. Lenz²⁴ S. Leone^{74a} C. Leonidopoulos⁵² A. Leopold¹⁴⁴ C. Leroy¹⁰⁸ R. Les¹⁰⁷ C. G. Lester³²
M. Levchenko³⁷ J. Levêque⁴ D. Levin¹⁰⁶ L. J. Levinson¹⁶⁸ M. P. Lewicki⁸⁶ D. J. Lewis⁴ A. Li⁵ B. Li^{62b}
C. Li^{62a} C-Q. Li^{62c} H. Li^{62a} H. Li^{62b} H. Li^{14c} H. Li^{62b} J. Li^{62c} K. Li¹³⁸ L. Li^{62c} M. Li^{14a,14e} Q. Y. Li^{62a}
S. Li^{14a,14e} S. Li^{62d,62c,y} T. Li^{62b} X. Li¹⁰⁴ Z. Li^{62b} Z. Li¹²⁶ Z. Li¹⁰⁴ Z. Li⁹² Z. Li^{14a,14e} Z. Liang^{14a}
M. Liberatore⁴⁸ B. Liberti^{76a} K. Lie^{64c} J. Lieber Marin^{82b} H. Lien⁶⁸ K. Lin¹⁰⁷ R. A. Linck⁶⁸
R. E. Lindley⁷ J. H. Lindon² A. Linss⁴⁸ E. Lipeles¹²⁸ A. Lipniacka¹⁶ A. Lister¹⁶³ J. D. Little⁴ B. Liu^{14a}
B. X. Liu¹⁴² D. Liu^{62d,62c} J. B. Liu^{62a} J. K. K. Liu³² K. Liu^{62d,62c} M. Liu^{62a} M. Y. Liu^{62a} P. Liu^{14a}
Q. Liu^{62d,138,62c} X. Liu^{62a} Y. Liu^{14d,14e} Y. L. Liu¹⁰⁶ Y. W. Liu^{62a} J. Llorente Merino¹⁴² S. L. Lloyd⁹⁴
E. M. Lobodzinska⁴⁸ P. Loch⁷ S. Loffredo^{76a,76b} T. Lohse¹⁸ K. Lohwasser¹³⁹ E. Loiacono⁴⁸ M. Lokajicek¹³¹
J. D. Lomas²⁰ J. D. Long¹⁶¹ I. Longarini¹⁵⁹ L. Longo^{70a,70b} R. Longo¹⁶¹ I. Lopez Paz⁶⁷ A. Lopez Solis⁴⁸
J. Lorenz¹⁰⁹ N. Lorenzo Martinez⁴ A. M. Lory¹⁰⁹ X. Lou^{47a,47b} X. Lou^{14a,14e} A. Lounis⁶⁶ J. Love⁶
P. A. Love⁹¹ G. Lu^{14a,14e} M. Lu⁸⁰ S. Lu¹²⁸ Y. J. Lu⁶⁵ H. J. Lubatti¹³⁸ C. Luci^{75a,75b} F. L. Lucio Alves^{14c}
A. Lucotte⁶⁰ F. Luehring⁶⁸ I. Luise¹⁴⁵ O. Lukianchuk⁶⁶ O. Lundberg¹⁴⁴ B. Lund-Jensen¹⁴⁴ N. A. Luongo¹²³
M. S. Lutz¹⁵¹ D. Lynn²⁹ H. Lyons⁹² R. Lysak¹³¹ E. Lytken⁹⁸ V. Lyubushkin³⁸ T. Lyubushkina³⁸
M. M. Lyukova¹⁴⁵ H. Ma²⁹ L. L. Ma^{62b} Y. Ma⁹⁶ D. M. Mac Donnell¹⁶⁴ G. Maccarrone⁵³ J. C. MacDonald¹³⁹
R. Madar⁴⁰ W. F. Mader⁵⁰ J. Maeda⁸⁴ T. Maeno²⁹ M. Maerker⁵⁰ H. Maguire¹³⁹ A. Maio^{130a,130b,130d}
K. Maj^{85a} O. Majersky⁴⁸ S. Majewski¹²³ N. Makovec⁶⁶ V. Maksimovic¹⁵ B. Malaescu¹²⁷ Pa. Malecki⁸⁶
V. P. Maleev³⁷ F. Malek⁶⁰ D. Malito^{43b,43a} U. Mallik⁸⁰ C. Malone³² S. Maltezos¹⁰ S. Malyukov³⁸
J. Mamuzic¹³ G. Mancini⁵³ G. Manco^{73a,73b} J. P. Mandalia⁹⁴ I. Mandić⁹³ L. Manhaes de Andrade Filho^{82a}
I. M. Maniatis¹⁶⁸ J. Manjarres Ramos^{102,hh} D. C. Mankad¹⁶⁸ A. Mann¹⁰⁹ B. Mansoulié¹³⁵ S. Manzoni³⁶
A. Marantis¹⁵² G. Marchiori⁵ M. Marcisovsky¹³¹ C. Marcon^{71a,71b} M. Marinescu²⁰ M. Marjanovic¹²⁰
E. J. Marshall⁹¹ Z. Marshall^{17a} S. Marti-Garcia¹⁶² T. A. Martin¹⁶⁶ V. J. Martin⁵² B. Martin dit Latour¹⁶
L. Martinelli^{75a,75b} M. Martinez^{13,t} P. Martinez Agullo¹⁶² V. I. Martinez Outschoorn¹⁰³ P. Martinez Suarez¹³
S. Martin-Haugh¹³⁴ V. S. Martoiu^{27b} A. C. Martyniuk⁹⁶ A. Marzin³⁶ S. R. Maschek¹¹⁰ D. Mascione^{78a,78b}
L. Masetti¹⁰⁰ T. Mashimo¹⁵³ J. Masik¹⁰¹ A. L. Maslennikov³⁷ L. Massa^{23b} P. Massarotti^{72a,72b}
P. Mastrandrea^{74a,74b} A. Mastroberardino^{43b,43a} T. Masubuchi¹⁵³ T. Mathisen¹⁶⁰ J. Matousek¹³³
N. Matsuzawa¹⁵³ J. Maurer^{27b} B. Maček⁹³ D. A. Maximov³⁷ R. Mazini¹⁴⁸ I. Maznas^{152,w} M. Mazza¹⁰⁷
S. M. Mazza¹³⁶ C. Mc Ginn²⁹ J. P. Mc Gowan¹⁰⁴ S. P. Mc Kee¹⁰⁶ E. F. McDonald¹⁰⁵ A. E. McDougall¹¹⁴

J. A. Mcfayden¹⁴⁶ R. P. McGovern¹²⁸ G. Mchedlidze^{149b} R. P. McKenzie^{33g} T. C. Mclachlan⁴⁸
 D. J. Mclaughlin⁹⁶ K. D. McLean¹⁶⁴ S. J. McMahon¹³⁴ P. C. McNamara¹⁰⁵ C. M. Mcpartland⁹²
 R. A. McPherson^{164,n} T. Megy⁴⁰ S. Mehlhase¹⁰⁹ A. Mehta⁹² D. Melini¹⁵⁰ B. R. Mellado Garcia^{33g}
 A. H. Melo⁵⁵ F. Meloni⁴⁸ A. M. Mendes Jacques Da Costa¹⁰¹ H. Y. Meng¹⁵⁵ L. Meng⁹¹ S. Menke¹¹⁰
 M. Mentink³⁶ E. Meoni^{43b,43a} C. Merlassino¹²⁶ L. Merola^{72a,72b} C. Meroni^{71a} G. Merz¹⁰⁶ O. Meshkov³⁷
 J. Metcalfe⁶ A. S. Mete⁶ C. Meyer⁶⁸ J-P. Meyer¹³⁵ R. P. Middleton¹³⁴ L. Mijović⁵² G. Mikenberg¹⁶⁸
 M. Mikestikova¹³¹ M. Mikuž⁹³ H. Mildner¹³⁹ A. Milic³⁶ C. D. Milke⁴⁴ D. W. Miller³⁹ L. S. Miller³⁴
 A. Milov¹⁶⁸ D. A. Milstead^{47a,47b} T. Min^{14c} A. A. Minaenko³⁷ I. A. Minashvili^{149b} L. Mince⁵⁹ A. I. Mincer¹¹⁷
 B. Mindur^{85a} M. Mineev³⁸ Y. Mino⁸⁷ L. M. Mir¹³ M. Miralles Lopez¹⁶² M. Mironova^{17a} A. Mishima¹⁵³
 M. C. Missio¹¹³ T. Mitani¹⁶⁷ A. Mitra¹⁶⁶ V. A. Mitsou¹⁶² O. Miu¹⁵⁵ P. S. Miyagawa⁹⁴ Y. Miyazaki⁸⁹
 A. Mizukami⁸³ T. Mkrtchyan^{63a} M. Mlinarevic⁹⁶ T. Mlinarevic⁹⁶ M. Mlynarikova³⁶ S. Mobius⁵⁵
 K. Mochizuki¹⁰⁸ P. Moder⁴⁸ P. Mogg¹⁰⁹ A. F. Mohammed^{14a,14e} S. Mohapatra⁴¹ G. Mokgatitswane^{33g}
 B. Mondal¹⁴¹ S. Mondal¹³² G. Monig¹⁴⁶ K. Mönig⁴⁸ E. Monnier¹⁰² L. Monsonis Romero¹⁶²
 J. Montejo Berlingen⁸³ M. Montella¹¹⁹ F. Monticelli⁹⁰ N. Morange⁶⁶ A. L. Moreira De Carvalho^{130a}
 M. Moreno Llácer¹⁶² C. Moreno Martinez⁵⁶ P. Morettini^{57b} S. Morgenstern³⁶ M. Morii⁶¹ M. Morinaga¹⁵³
 A. K. Morley³⁶ F. Morodei^{75a,75b} L. Morvaj³⁶ P. Moschovakos³⁶ B. Moser³⁶ M. Mosidze^{149b} T. Moskalets⁵⁴
 P. Moskvitina¹¹³ J. Moss^{31,z} E. J. W. Moyses¹⁰³ O. Mtintsilana^{33g} S. Muanza¹⁰² J. Mueller¹²⁹
 D. Muenstermann⁹¹ R. Müller¹⁹ G. A. Mullier¹⁶⁰ J. J. Mullin¹²⁸ D. P. Mungo¹⁵⁵ D. Munoz Perez¹⁶²
 F. J. Munoz Sanchez¹⁰¹ M. Murin¹⁰¹ W. J. Murray^{166,134} A. Murrone^{71a,71b} J. M. Muse¹²⁰ M. Muškinja^{17a}
 C. Mwewa²⁹ A. G. Myagkov^{37,k} A. J. Myers⁸ A. A. Myers¹²⁹ G. Myers⁶⁸ M. Myska¹³² B. P. Nachman^{17a}
 O. Nackenhorst⁴⁹ A. Nag⁵⁰ K. Nagai¹²⁶ K. Nagano⁸³ J. L. Nagle^{29,h} E. Nagy¹⁰² A. M. Nairz³⁶
 Y. Nakahama⁸³ K. Nakamura⁸³ H. Nanjo¹²⁴ R. Narayan⁴⁴ E. A. Narayanan¹¹² I. Naryshkin³⁷ M. Naseri³⁴
 S. Nasri^{116b} C. Nass²⁴ G. Navarro^{22a} J. Navarro-Gonzalez¹⁶² R. Nayak¹⁵¹ A. Nayaz¹⁸ P. Y. Nechaeva³⁷
 F. Nechansky⁴⁸ L. Nedic¹²⁶ T. J. Neep²⁰ A. Negri^{73a,73b} M. Negrini^{23b} C. Nellist¹¹⁴ C. Nelson¹⁰⁴
 K. Nelson¹⁰⁶ S. Nemecek¹³¹ M. Nessi^{36,aa} M. S. Neubauer¹⁶¹ F. Neuhaus¹⁰⁰ J. Neundorff⁴⁸ R. Newhouse¹⁶³
 P. R. Newman²⁰ C. W. Ng¹²⁹ Y. W. Y. Ng⁴⁸ B. Ngair^{35e} H. D. N. Nguyen¹⁰⁸ R. B. Nickerson¹²⁶
 R. Nicolaidou¹³⁵ J. Nielsen¹³⁶ M. Niemeyer⁵⁵ J. Niermann^{55,36} N. Nikiforou³⁶ V. Nikolaenko^{37,k}
 I. Nikolic-Audit¹²⁷ K. Nikolopoulos²⁰ P. Nilsson²⁹ I. Ninca⁴⁸ H. R. Nindhito⁵⁶ G. Ninio¹⁵¹ A. Nisati^{75a}
 N. Nishu² R. Nisius¹¹⁰ J-E. Nitschke⁵⁰ E. K. Nkademeng^{33g} S. J. Noacco Rosende⁹⁰ T. Nobe¹⁵³
 D. L. Noel³² T. Nommensen¹⁴⁷ M. A. Nomura²⁹ M. B. Norfolk¹³⁹ R. R. B. Norisam⁹⁶ B. J. Norman³⁴
 J. Novak⁹³ T. Novak⁴⁸ L. Novotny¹³² R. Novotny¹¹² L. Nozka¹²² K. Ntekas¹⁵⁹
 N. M. J. Nunes De Moura Junior^{82b} E. Nurse⁹⁶ J. Ocariz¹²⁷ A. Ochi⁸⁴ I. Ochoa^{130a} S. Oerdek¹⁶⁰
 J. T. Offermann³⁹ A. Ogrodnik^{85a} A. Oh¹⁰¹ C. C. Ohm¹⁴⁴ H. Oide⁸³ R. Oishi¹⁵³ M. L. Ojeda⁴⁸
 Y. Okazaki⁸⁷ M. W. O'Keefe⁹² Y. Okumura¹⁵³ L. F. Oleiro Seabra^{130a} S. A. Olivares Pino^{137d}
 D. Oliveira Damazio²⁹ D. Oliveira Goncalves^{82a} J. L. Oliver¹⁵⁹ M. J. R. Olsson¹⁵⁹ A. Olszewski⁸⁶
 Ö. O. Öncel⁵⁴ D. C. O'Neil¹⁴² A. P. O'Neill¹⁹ A. Onofre^{130a,130e} P. U. E. Onyisi¹¹ M. J. Oreglia³⁹
 G. E. Orellana⁹⁰ D. Orestano^{77a,77b} N. Orlando¹³ R. S. Orr¹⁵⁵ V. O'Shea⁵⁹ R. Ospanov^{62a}
 G. Otero y Garzon³⁰ H. Otono⁸⁹ P. S. Ott^{63a} G. J. Ottino^{17a} M. Ouchrif^{35d} J. Ouellette²⁹ F. Ould-Saada¹²⁵
 M. Owen⁵⁹ R. E. Owen¹³⁴ K. Y. Oyulmaz^{21a} V. E. Ozcan^{21a} N. Ozturk⁸ S. Ozturk^{21d} H. A. Pacey³²
 A. Pacheco Pages¹³ C. Padilla Aranda¹³ G. Padovano^{75a,75b} S. Pagan Griso^{17a} G. Palacino⁶⁸ A. Palazzo^{70a,70b}
 S. Palestini³⁶ J. Pan¹⁷¹ T. Pan^{64a} D. K. Panchal¹¹ C. E. Pandini¹¹⁴ J. G. Panduro Vazquez⁹⁵ H. Pang^{14b}
 P. Pani⁴⁸ G. Panizzo^{69a,69c} L. Paolozzi⁵⁶ C. Papadatos¹⁰⁸ S. Parajuli⁴⁴ A. Paramonov⁶ C. Paraskevopoulos¹⁰
 D. Paredes Hernandez^{64b} T. H. Park¹⁵⁵ M. A. Parker³² F. Parodi^{57b,57a} E. W. Parrish¹¹⁵ V. A. Parrish⁵²
 J. A. Parsons⁴¹ U. Parzefall⁵⁴ B. Pascual Dias¹⁰⁸ L. Pascual Dominguez¹⁵¹ F. Pasquali¹¹⁴ E. Pasqualucci^{75a}
 S. Passaggio^{57b} F. Pastore⁹⁵ P. Pasuwan^{47a,47b} P. Patel⁸⁶ U. M. Patel⁵¹ J. R. Pater¹⁰¹ T. Pauly³⁶
 J. Pearkes¹⁴³ M. Pedersen¹²⁵ R. Pedro^{130a} S. V. Peleganchuk³⁷ O. Penc³⁶ E. A. Pender⁵² H. Peng^{62a}
 K. E. Pensi¹⁰⁹ M. Penzin³⁷ B. S. Peralva^{82d} A. P. Pereira Peixoto⁶⁰ L. Pereira Sanchez^{47a,47b}
 D. V. Perpelitsa^{29,h} E. Perez Codina^{156a} M. Perganti¹⁰ L. Perini^{71a,71b,a} H. Pernegger³⁶ S. Perrella³⁶
 A. Perrevoort¹¹³ O. Perrin⁴⁰ K. Peters⁴⁸ R. F. Y. Peters¹⁰¹ B. A. Petersen³⁶ T. C. Petersen⁴² E. Petit¹⁰²

V. Petousis¹³² C. Petridou^{152,w} A. Petrukhin¹⁴¹ M. Pettee^{17a} N. E. Pettersson³⁶ A. Petukhov³⁷
 K. Petukhova¹³³ A. Peyaud¹³⁵ R. Pezoa^{137f} L. Pezzotti³⁶ G. Pezzullo¹⁷¹ T. M. Pham¹⁶⁹ T. Pham¹⁰⁵
 P. W. Phillips¹³⁴ M. W. Phipps¹⁶¹ G. Piacquadio¹⁴⁵ E. Pianori^{17a} F. Piazza^{71a,71b} R. Piegai³⁰ D. Pietreanu^{27b}
 A. D. Pilkington¹⁰¹ M. Pinamonti^{69a,69c} J. L. Pinfold² B. C. Pinheiro Pereira^{130a} A. E. Pinto Pinoargote¹³⁵
 C. Pitman Donaldson⁹⁶ D. A. Pizzi³⁴ L. Pizzimento^{76a,76b} A. Pizzini¹¹⁴ M.-A. Pleier²⁹ V. Plesanovs⁵⁴
 V. Pleskot¹³³ E. Plotnikova³⁸ G. Poddar⁴ R. Poettgen⁹⁸ L. Poggioli¹²⁷ D. Pohl²⁴ I. Pokharel⁵⁵ S. Polacek¹³³
 G. Polesello^{73a} A. Poley^{142,156a} R. Polifka¹³² A. Polini^{23b} C. S. Pollard¹⁶⁶ Z. B. Pollock¹¹⁹
 V. Polychronakos²⁹ E. Pompa Pacchi^{75a,75b} D. Ponomarenko¹¹³ L. Pontecorvo³⁶ S. Popa^{27a} G. A. Popeneciu^{27d}
 D. M. Portillo Quintero^{156a} S. Pospisil¹³² P. Postolache^{27c} K. Potamianos¹²⁶ P. P. Potepa^{85a} I. N. Potrap³⁸
 C. J. Potter³² H. Potti¹ T. Poulsen⁴⁸ J. Poveda¹⁶² M. E. Pozo Astigarraga³⁶ A. Prades Ibanez¹⁶²
 M. M. Prapa⁴⁶ J. Pretel⁵⁴ D. Price¹⁰¹ M. Primavera^{70a} M. A. Principe Martin⁹⁹ R. Privara¹²² T. Procter⁵⁹
 M. L. Proffitt¹³⁸ N. Proklova¹²⁸ K. Prokofiev^{64c} G. Proto^{76a,76b} S. Protopopescu²⁹ J. Proudfoot⁶
 M. Przybycien^{85a} W. W. Przygoda^{85b} J. E. Puddefoot¹³⁹ D. Pudzha³⁷ D. Pyatiizybantseva³⁷ J. Qian¹⁰⁶
 D. Qichen¹⁰¹ Y. Qin¹⁰¹ T. Qiu⁵² A. Quadt⁵⁵ M. Queitsch-Maitland¹⁰¹ G. Quetant⁵⁶ G. Rabanal Bolanos⁶¹
 D. Rafanoharana⁵⁴ F. Ragusa^{71a,71b} J. L. Rainbolt³⁹ J. A. Raine⁵⁶ S. Rajagopalan²⁹ E. Ramakoti³⁷
 K. Ran^{48,14e} N. P. Rapheeha^{33g} H. Rasheed^{27b} V. Raskina¹²⁷ D. F. Rassloff^{63a} S. Rave¹⁰⁰ B. Ravina⁵⁵
 I. Ravinovich¹⁶⁸ M. Raymond³⁶ A. L. Read¹²⁵ N. P. Readioff¹³⁹ D. M. Rebuzzi^{73a,73b} G. Redlinger²⁹
 K. Reeves²⁶ J. A. Reidelsturz¹⁷⁰ D. Reikher¹⁵¹ A. Rej¹⁴¹ C. Rembser³⁶ A. Renardi⁴⁸ M. Renda^{27b}
 M. B. Rendel¹¹⁰ F. Renner⁴⁸ A. G. Rennie⁵⁹ S. Resconi^{71a} M. Ressegotti^{57b,57a} E. D. Resseguie^{17a} S. Rettie³⁶
 J. G. Reyes Rivera¹⁰⁷ B. Reynolds¹¹⁹ E. Reynolds^{17a} M. Rezaei Estabragh¹⁷⁰ O. L. Rezanova³⁷ P. Reznicek¹³³
 N. Ribaric⁹¹ E. Ricci^{78a,78b} R. Richter¹¹⁰ S. Richter^{47a,47b} E. Richter-Was^{85b} M. Ridel¹²⁷ S. Ridouani^{35d}
 P. Rieck¹¹⁷ P. Riedler³⁶ M. Rijssenbeek¹⁴⁵ A. Rimoldi^{73a,73b} M. Rimoldi⁴⁸ L. Rinaldi^{23b,23a} T. T. Rinn²⁹
 M. P. Rinnagel¹⁰⁹ G. Ripellino¹⁶⁰ I. Riu¹³ P. Rivadeneira⁴⁸ J. C. Rivera Vergara¹⁶⁴ F. Rizatdinova¹²¹
 E. Rizvi⁹⁴ C. Rizzi⁵⁶ B. A. Roberts¹⁶⁶ B. R. Roberts^{17a} S. H. Robertson^{104,n} M. Robin⁴⁸ D. Robinson³²
 C. M. Robles Gajardo^{137f} M. Robles Manzano¹⁰⁰ A. Robson⁵⁹ A. Rocchi^{76a,76b} C. Roda^{74a,74b}
 S. Rodriguez Bosca^{63a} Y. Rodriguez Garcia^{22a} A. Rodriguez Rodriguez⁵⁴ A. M. Rodriguez Vera^{156b} S. Roe³⁶
 J. T. Roemer¹⁵⁹ A. R. Roepe-Gier¹³⁶ J. Roggel¹⁷⁰ O. Røhne¹²⁵ R. A. Rojas¹⁰³ C. P. A. Roland⁶⁸ J. Roloff²⁹
 A. Romaniouk³⁷ E. Romano^{73a,73b} M. Romano^{23b} A. C. Romero Hernandez¹⁶¹ N. Rompotis⁹² L. Roos¹²⁷
 S. Rosati^{75a} B. J. Rosser³⁹ E. Rossi¹²⁶ E. Rossi^{72a,72b} L. P. Rossi^{57b} L. Rossini⁴⁸ R. Rosten¹¹⁹
 M. Rotaru^{27b} B. Rottler⁵⁴ C. Rougier¹⁰² D. Rousseau⁶⁶ D. Rousso³² A. Roy¹⁶¹ S. Roy-Garand¹⁵⁵
 A. Rozanov¹⁰² Y. Rozen¹⁵⁰ X. Ruan^{33g} A. Rubio Jimenez¹⁶² A. J. Ruby⁹² V. H. Ruelas Rivera¹⁸
 T. A. Ruggeri¹ A. Ruggiero¹²⁶ A. Ruiz-Martinez¹⁶² A. Rummeler³⁶ Z. Rurikova⁵⁴ N. A. Rusakovich³⁸
 H. L. Russell¹⁶⁴ J. P. Rutherford⁷ K. Rybacki⁹¹ M. Rybar¹³³ E. B. Rye¹²⁵ A. Ryzhov³⁷
 J. A. Sabater Iglesias⁵⁶ P. Sabatini¹⁶² L. Sabetta^{75a,75b} H. F.-W. Sadrozinski¹³⁶ F. Safai Tehrani^{75a}
 B. Safarzadeh Samani¹⁴⁶ M. Safdari¹⁴³ S. Saha¹⁰⁴ M. Sahinsoy¹¹⁰ M. Saimpert¹³⁵ M. Saito¹⁵³ T. Saito¹⁵³
 D. Salamani³⁶ A. Salnikov¹⁴³ J. Salt¹⁶² A. Salvador Salas¹³ D. Salvatore^{43b,43a} F. Salvatore¹⁴⁶
 A. Salzburger³⁶ D. Sammel⁵⁴ D. Sampsonidis^{152,w} D. Sampsonidou^{123,62c} J. Sánchez¹⁶² A. Sanchez Pineda⁴
 V. Sanchez Sebastian¹⁶² H. Sandaker¹²⁵ C. O. Sander⁴⁸ J. A. Sandesara¹⁰³ M. Sandhoff¹⁷⁰ C. Sandoval^{22b}
 D. P. C. Sankey¹³⁴ T. Sano⁸⁷ A. Sansoni⁵³ L. Santi^{75a,75b} C. Santoni⁴⁰ H. Santos^{130a,130b} S. N. Santpur^{17a}
 A. Santra¹⁶⁸ K. A. Saoucha¹³⁹ J. G. Saraiva^{130a,130d} J. Sardain⁷ O. Sasaki⁸³ K. Sato¹⁵⁷ C. Sauer^{63b}
 F. Sauerburger⁵⁴ E. Sauvan⁴ P. Savard^{155,e} R. Sawada¹⁵³ C. Sawyer¹³⁴ L. Sawyer⁹⁷ I. Sayago Galvan¹⁶²
 C. Sbarra^{23b} A. Sbrizzi^{23b,23a} T. Scanlon⁹⁶ J. Schaarschmidt¹³⁸ P. Schacht¹¹⁰ D. Schaefer³⁹ U. Schäfer¹⁰⁰
 A. C. Schaffer^{66,44} D. Schaile¹⁰⁹ R. D. Schamberger¹⁴⁵ E. Schanet¹⁰⁹ C. Scharf¹⁸ M. M. Schefer¹⁹
 V. A. Schegelsky³⁷ D. Scheirich¹³³ F. Schenck¹⁸ M. Schernau¹⁵⁹ C. Scheulen⁵⁵ C. Schiavi^{57b,57a}
 E. J. Schioppa^{70a,70b} M. Schioppa^{43b,43a} B. Schlag^{143,mm} K. E. Schleicher⁵⁴ S. Schlenker³⁶ J. Schmeing¹⁷⁰
 M. A. Schmidt¹⁷⁰ K. Schmieden¹⁰⁰ C. Schmitt¹⁰⁰ S. Schmitt⁴⁸ L. Schoeffel¹³⁵ A. Schoening^{63b}
 P. G. Scholer⁵⁴ E. Schopf¹²⁶ M. Schott¹⁰⁰ J. Schovancova³⁶ S. Schramm⁵⁶ F. Schroeder¹⁷⁰
 H.-C. Schultz-Coulon^{63a} M. Schumacher⁵⁴ B. A. Schumm¹³⁶ Ph. Schune¹³⁵ A. J. Schuy¹³⁸ H. R. Schwartz¹³⁶
 A. Schwartzman¹⁴³ T. A. Schwarz¹⁰⁶ Ph. Schwemling¹³⁵ R. Schwienhorst¹⁰⁷ A. Sciandra¹³⁶ G. Sciolla²⁶

F. Scuri^{74a} F. Scutti,¹⁰⁵ C. D. Sebastiani⁹² K. Sedlaczek⁴⁹ P. Seema¹⁸ S. C. Seidel¹¹² A. Seiden¹³⁶
 B. D. Seidlitz⁴¹ C. Seitz⁴⁸ J. M. Seixas^{82b} G. Sekhniaidze^{72a} S. J. Sekula⁴⁴ L. Selem⁴
 N. Semprini-Cesari^{23b,23a} S. Sen⁵¹ D. Sengupta⁵⁶ V. Senthilkumar¹⁶² L. Serin⁶⁶ L. Serkin^{69a,69b}
 M. Sessa^{77a,77b} H. Severini¹²⁰ F. Sforza^{57b,57a} A. Sfyrla⁵⁶ E. Shabalina⁵⁵ R. Shaheen¹⁴⁴ J. D. Shahinian¹²⁸
 D. Shaked Renous¹⁶⁸ L. Y. Shan^{14a} M. Shapiro^{17a} A. Sharma³⁶ A. S. Sharma¹⁶³ P. Sharma⁸⁰ S. Sharma⁴⁸
 P. B. Shatalov³⁷ K. Shaw¹⁴⁶ S. M. Shaw¹⁰¹ Q. Shen^{62c,5} P. Sherwood⁹⁶ L. Shi⁹⁶ X. Shi^{14a}
 C. O. Shimmin¹⁷¹ Y. Shimogama¹⁶⁷ J. D. Shinner⁹⁵ I. P. J. Shipsey¹²⁶ S. Shirabe⁶⁰ M. Shiyakova^{38,nn}
 J. Shlomi¹⁶⁸ M. J. Shochet³⁹ J. Shojaii¹⁰⁵ D. R. Shope¹²⁵ S. Shrestha^{119,bb} E. M. Shrif^{33g} M. J. Shroff¹⁶⁴
 P. Sicho¹³¹ A. M. Sickles¹⁶¹ E. Sideras Haddad^{33g} A. Sidoti^{23b} F. Siegert⁵⁰ Dj. Sijacki¹⁵ R. Sikora^{85a}
 F. Sili⁹⁰ J. M. Silva²⁰ M. V. Silva Oliveira³⁶ S. B. Silverstein^{47a} S. Simion⁶⁶ R. Simoniello³⁶ E. L. Simpson⁵⁹
 H. Simpson¹⁴⁶ L. R. Simpson¹⁰⁶ N. D. Simpson⁹⁸ S. Simsek^{21d} S. Sindhu⁵⁵ P. Sinervo¹⁵⁵ S. Singh¹⁴²
 S. Singh¹⁵⁵ S. Sinha⁴⁸ S. Sinha^{33g} M. Sioli^{23b,23a} I. Siral³⁶ S. Yu. Sivoklov^{37,a} J. Sjölin^{47a,47b} A. Skaf⁵⁵
 E. Skorda⁹⁸ P. Skubic¹²⁰ M. Slawinska⁸⁶ V. Smakhtin¹⁶⁸ B. H. Smart¹³⁴ J. Smiesko³⁶ S. Yu. Smirnov³⁷
 Y. Smirnov³⁷ L. N. Smirnova^{37,k} O. Smirnova⁹⁸ A. C. Smith⁴¹ E. A. Smith³⁹ H. A. Smith¹²⁶ J. L. Smith⁹²
 R. Smith¹⁴³ M. Smizanska⁹¹ K. Smolek¹³² A. A. Snesarev³⁷ S. R. Snider¹⁵⁵ H. L. Snoek¹¹⁴ S. Snyder²⁹
 R. Sobie^{164,n} A. Soffer¹⁵¹ C. A. Solans Sanchez³⁶ E. Yu. Soldatov³⁷ U. Soldevila¹⁶² A. A. Solodkov³⁷
 S. Solomon²⁶ A. Soloshenko³⁸ K. Solovieva⁵⁴ O. V. Solovyanov⁴⁰ V. Solovyev³⁷ P. Sommer³⁶ A. Sonay¹³
 W. Y. Song^{156b} J. M. Sonneveld¹¹⁴ A. Sopczak¹³² A. L. Sapiro⁹⁶ F. Sopkova^{28b} V. Sothilingam^{63a}
 S. Sottocornola⁶⁸ R. Soualah^{116c} Z. Soumami^{35e} D. South⁴⁸ S. Spagnolo^{70a,70b} M. Spalla¹¹⁰ D. Sperlich⁵⁴
 G. Spigo³⁶ M. Spina¹⁴⁶ S. Spinali⁹¹ D. P. Spiteri⁵⁹ M. Spousta¹³³ E. J. Staats³⁴ A. Stabile^{71a,71b}
 R. Stamen^{63a} M. Stamenkovic¹¹⁴ A. Stampekis²⁰ M. Standke²⁴ E. Stanecka⁸⁶ M. V. Stange⁵⁰
 B. Stanislaus^{17a} M. M. Stanitzki⁴⁸ M. Stankaityte¹²⁶ B. Stapf⁴⁸ E. A. Starchenko³⁷ G. H. Stark¹³⁶
 J. Stark^{102,hh} D. M. Starko^{156b} P. Staroba¹³¹ P. Starovoitov^{63a} S. Stärz¹⁰⁴ R. Staszewski⁸⁶ G. Stavropoulos⁴⁶
 J. Steentoft¹⁶⁰ P. Steinberg²⁹ B. Stelzer^{142,156a} H. J. Stelzer¹²⁹ O. Stelzer-Chilton^{156a} H. Stenzel⁵⁸
 T. J. Stevenson¹⁴⁶ G. A. Stewart³⁶ J. R. Stewart¹²¹ M. C. Stockton³⁶ G. Stoicea^{27b} M. Stolarski^{130a}
 S. Stonjek¹¹⁰ A. Straessner⁵⁰ J. Strandberg¹⁴⁴ S. Strandberg^{47a,47b} M. Strauss¹²⁰ T. Streblor¹⁰²
 P. Strizenec^{28b} R. Ströhmer¹⁶⁵ D. M. Strom¹²³ L. R. Strom⁴⁸ R. Stroynowski⁴⁴ A. Strubig^{47a,47b}
 S. A. Stucci²⁹ B. Stugu¹⁶ J. Stupak¹²⁰ N. A. Styles⁴⁸ D. Su¹⁴³ S. Su^{62a} W. Su^{62d,138,62c} X. Su^{62a,66}
 K. Sugizaki¹⁵³ V. V. Sulin³⁷ M. J. Sullivan⁹² D. M. S. Sultan^{78a,78b} L. Sultanaliyeva³⁷ S. Sultansoy^{3b}
 T. Sumida⁸⁷ S. Sun¹⁰⁶ S. Sun¹⁶⁹ O. Sunneborn Gudnadottir¹⁶⁰ M. R. Sutton¹⁴⁶ M. Svatos¹³¹
 M. Swiatlowski^{156a} T. Swirski¹⁶⁵ I. Sykora^{28a} M. Sykora¹³³ T. Sykora¹³³ D. Ta¹⁰⁰ K. Tackmann^{48,cc}
 A. Taffard¹⁵⁹ R. Tafirout^{156a} J. S. Tafoya Vargas⁶⁶ R. H. M. Taibah¹²⁷ R. Takashima⁸⁸ E. P. Takeva⁵²
 Y. Takubo⁸³ M. Talby¹⁰² A. A. Talyshev³⁷ K. C. Tam^{64b} N. M. Tamir¹⁵¹ A. Tanaka¹⁵³ J. Tanaka¹⁵³
 R. Tanaka⁶⁶ M. Tanasini^{57b,57a} Z. Tao¹⁶³ S. Tapia Araya^{137f} S. Tapprogge¹⁰⁰ A. Tarek Abouelfadl Mohamed¹⁰⁷
 S. Tarem¹⁵⁰ K. Tariq^{62b} G. Tarna^{102,27b} G. F. Tartarelli^{71a} P. Tas¹³³ M. Tasevsky¹³¹ E. Tassi^{43b,43a}
 A. C. Tate¹⁶¹ G. Tatenon¹⁵³ Y. Tayalati^{35e,dd} G. N. Taylor¹⁰⁵ W. Taylor^{156b} H. Teagle⁹² A. S. Tee¹⁶⁹
 R. Teixeira De Lima¹⁴³ P. Teixeira-Dias⁹⁵ J. J. Teoh¹⁵⁵ K. Terashi¹⁵³ J. Terron⁹⁹ S. Terzo¹³ M. Testa⁵³
 R. J. Teuscher^{155,n} A. Thaler⁷⁹ O. Theiner⁵⁶ N. Themistokleous⁵² T. Thevenaux-Pelzer¹⁰² O. Thielmann¹⁷⁰
 D. W. Thomas⁹⁵ J. P. Thomas²⁰ E. A. Thompson^{17a} P. D. Thompson²⁰ E. Thomson¹²⁸ Y. Tian⁵⁵
 V. Tikhomirov^{37,k} Yu. A. Tikhonov³⁷ S. Timoshenko³⁷ E. X. L. Ting¹ P. Tipton¹⁷¹ S. H. Tlou^{33g} A. Tnourji⁴⁰
 K. Todome^{23b,23a} S. Todorova-Nova¹³³ S. Todt⁵⁰ M. Togawa⁸³ J. Tojo⁸⁹ S. Tokár^{28a} K. Tokushuku⁸³
 O. Toldaiev⁶⁸ R. Tombs³² M. Tomoto^{83,111} L. Tompkins^{143,mm} K. W. Topolnicki^{85b} E. Torrence¹²³
 H. Torres¹⁰² E. Torró Pastor¹⁶² M. Toscani³⁰ C. Toscirci³⁹ M. Tost¹¹ D. R. Tovey¹³⁹ A. Traeet¹⁶
 I. S. Trandafir^{27b} T. Trefzger¹⁶⁵ A. Tricoli²⁹ I. M. Trigger^{156a} S. Trincaz-Duvoid¹²⁷ D. A. Trischuk²⁶
 B. Trocme⁶⁰ C. Troncon^{71a} L. Truong^{33c} M. Trzebinski⁸⁶ A. Trzupek⁸⁶ F. Tsai¹⁴⁵ M. Tsai¹⁰⁶
 A. Tsiamis^{152,w} P. V. Tsiarehka³⁷ S. Tsigaridas^{156a} A. Tsigotis^{152,x} V. Tsiskaridze¹⁴⁵ E. G. Tskhadadze^{149a}
 M. Tsopoulou^{152,w} Y. Tsujikawa⁸⁷ I. I. Tsukerman³⁷ V. Tsulaia^{17a} S. Tsuno⁸³ O. Tsur¹⁵⁰ K. Tsurii¹¹⁸
 D. Tsybychev¹⁴⁵ Y. Tu^{64b} A. Tudorache^{27b} V. Tudorache^{27b} A. N. Tuna³⁶ S. Turchikhin³⁸ I. Turk Cakir^{3a}
 R. Turra^{71a} T. Turtuvshin^{38,ee} P. M. Tuts⁴¹ S. Tzamaras^{152,w} P. Tzanis¹⁰ E. Tzovara¹⁰⁰ K. Uchida¹⁵³

F. Ukegawa¹⁵⁷ P. A. Ulloa Poblete^{137c} E. N. Umaka²⁹ G. Unal³⁶ M. Unal¹¹ A. Undrus²⁹ G. Unel¹⁵⁹
 J. Urban^{28b} P. Urquijo¹⁰⁵ G. Usai⁸ R. Ushioda¹⁵⁴ M. Usman¹⁰⁸ Z. Uysal^{21b} L. Vacavant¹⁰² V. Vacek¹³²
 B. Vachon¹⁰⁴ K. O. H. Vadla¹²⁵ T. Vafeiadis³⁶ A. Vaitkus⁹⁶ C. Valderanis¹⁰⁹ E. Valdes Santurio^{47a,47b}
 M. Valente^{156a} S. Valentineti^{23b,23a} A. Valero¹⁶² E. Valiente Moreno¹⁶² A. Vallier^{102,hh} J. A. Valls Ferrer¹⁶²
 D. R. Van Arneeman¹¹⁴ T. R. Van Daalen¹³⁸ P. Van Gemmeren⁶ M. Van Rijnbach^{125,36} S. Van Stroud⁹⁶
 I. Van Vulpen¹¹⁴ M. Vanadia^{76a,76b} W. Vandelli³⁶ M. Vandenbroucke¹³⁵ E. R. Vandewall¹²¹ D. Vannicola¹⁵¹
 L. Vannoli^{57b,57a} R. Vari^{75a} E. W. Varnes⁷ C. Varni^{17a} T. Varol¹⁴⁸ D. Varouchas⁶⁶ L. Varriale¹⁶²
 K. E. Varvell¹⁴⁷ M. E. Vasile^{27b} L. Vaslin⁴⁰ G. A. Vasquez¹⁶⁴ F. Vazeille⁴⁰ T. Vazquez Schroeder³⁶ J. Veatch³¹
 V. Vecchio¹⁰¹ M. J. Veen¹⁰³ I. Veliscek¹²⁶ L. M. Veloce¹⁵⁵ F. Veloso^{130a,130c} S. Veneziano^{75a}
 A. Ventura^{70a,70b} A. Verbytskyi¹¹⁰ M. Verducci^{74a,74b} C. Vergis²⁴ M. Verissimo De Araujo^{82b} W. Verkerke¹¹⁴
 J. C. Vermeulen¹¹⁴ C. Vernieri¹⁴³ P. J. Verschuuren⁹⁵ M. Vessella¹⁰³ M. C. Vetterli^{142,e} A. Vgenopoulos^{152,w}
 N. Viaux Maira^{137f} T. Vickey¹³⁹ O. E. Vickey Boeriu¹³⁹ G. H. A. Viehhauser¹²⁶ L. Vigani^{63b} M. Villa^{23b,23a}
 M. Villaplana Perez¹⁶² E. M. Villhauer⁵² E. Vilucchi⁵³ M. G. Vincter³⁴ G. S. Virdee²⁰ A. Vishwakarma⁵²
 C. Vittori³⁶ I. Vivarelli¹⁴⁶ V. Vladimirov¹⁶⁶ E. Voevodina¹¹⁰ F. Vogel¹⁰⁹ P. Vokac¹³² J. Von Ahnen⁴⁸
 E. Von Toerne²⁴ B. Vormwald³⁶ V. Vorobel¹³³ K. Vorobev³⁷ M. Vos¹⁶² K. Voss¹⁴¹ J. H. Vosseveld⁹²
 M. Vozak¹¹⁴ L. Vozdecky⁹⁴ N. Vranjes¹⁵ M. Vranjes Milosavljevic¹⁵ M. Vreeswijk¹¹⁴ R. Vuillermet³⁶
 O. Vujanovic¹⁰⁰ I. Vukotic³⁹ S. Wada¹⁵⁷ C. Wagner¹⁰³ J. M. Wagner^{17a} W. Wagner¹⁷⁰ S. Wahdan¹⁷⁰
 H. Wahlberg⁹⁰ R. Wakasa¹⁵⁷ M. Wakida¹¹¹ J. Walder¹³⁴ R. Walker¹⁰⁹ W. Walkowiak¹⁴¹ A. Wall¹²⁸
 A. Z. Wang¹⁶⁹ C. Wang¹⁰⁰ C. Wang^{62c} H. Wang^{17a} J. Wang^{64a} R.-J. Wang¹⁰⁰ R. Wang⁶¹ R. Wang⁶
 S. M. Wang¹⁴⁸ S. Wang^{62b} T. Wang^{62a} W. T. Wang⁸⁰ X. Wang^{14c} X. Wang¹⁶¹ X. Wang^{62c} Y. Wang^{62d}
 Y. Wang^{14c} Z. Wang¹⁰⁶ Z. Wang^{62d,51,62c} Z. Wang¹⁰⁶ A. Warburton¹⁰⁴ R. J. Ward²⁰ N. Warrack⁵⁹
 A. T. Watson²⁰ H. Watson⁵⁹ M. F. Watson²⁰ G. Watts¹³⁸ B. M. Waugh⁹⁶ C. Weber²⁹ H. A. Weber¹⁸
 M. S. Weber¹⁹ S. M. Weber^{63a} C. Wei^{62a} Y. Wei¹²⁶ A. R. Weidberg¹²⁶ E. J. Weik¹¹⁷ J. Weingarten⁴⁹
 M. Weirich¹⁰⁰ C. Weiser⁵⁴ C. J. Wells⁴⁸ T. Wenaus²⁹ B. Wendland⁴⁹ T. Wengler³⁶ N. S. Wenke¹¹⁰
 N. Wermes²⁴ M. Wessels^{63a} K. Whalen¹²³ A. M. Wharton⁹¹ A. S. White⁶¹ A. White⁸ M. J. White¹
 D. Whiteson¹⁵⁹ L. Wickremasinghe¹²⁴ W. Wiedenmann¹⁶⁹ C. Wiel⁵⁰ M. Wielers¹³⁴ C. Wiglesworth⁴²
 L. A. M. Wiik-Fuchs⁵⁴ D. J. Wilbern¹²⁰ H. G. Wilkens³⁶ D. M. Williams⁴¹ H. H. Williams¹²⁸ S. Williams³²
 S. Willocq¹⁰³ B. J. Wilson¹⁰¹ P. J. Windischhofer³⁹ F. Winklmeier¹²³ B. T. Winter⁵⁴ J. K. Winter¹⁰¹
 M. Wittgen¹⁴³ M. Wobisch⁹⁷ R. Wölker¹²⁶ J. Wollrath¹⁵⁹ M. W. Wolter⁸⁶ H. Wolters^{130a,130c} V. W. S. Wong¹⁶³
 A. F. Wongel⁴⁸ S. D. Worm⁴⁸ B. K. Wosiek⁸⁶ K. W. Woźniak⁸⁶ K. Wraight⁵⁹ J. Wu^{14a,14e} M. Wu^{64a}
 M. Wu¹¹³ S. L. Wu¹⁶⁹ X. Wu⁵⁶ Y. Wu^{62a} Z. Wu¹³⁵ J. Wuerzinger¹¹⁰ T. R. Wyatt¹⁰¹ B. M. Wynne⁵²
 S. Xella⁴² L. Xia^{14c} M. Xia^{14b} J. Xiang^{64c} X. Xiao¹⁰⁶ M. Xie^{62a} X. Xie^{62a} S. Xin^{14a,14e} J. Xiong^{17a}
 I. Xioutidis¹⁴⁶ D. Xu^{14a} H. Xu^{62a} H. Xu^{62a} L. Xu^{62a} R. Xu¹²⁸ T. Xu¹⁰⁶ Y. Xu^{14b} Z. Xu⁵² Z. Xu^{14a}
 B. Yabsley¹⁴⁷ S. Yacoob^{33a} N. Yamaguchi⁸⁹ Y. Yamaguchi¹⁵⁴ H. Yamauchi¹⁵⁷ T. Yamazaki^{17a}
 Y. Yamazaki⁸⁴ J. Yan^{62c} S. Yan¹²⁶ Z. Yan²⁵ H. J. Yang^{62c,62d} H. T. Yang^{62a} S. Yang^{62a} T. Yang^{64c}
 X. Yang^{62a} X. Yang^{14a} Y. Yang⁴⁴ Z. Yang^{62a,106} W.-M. Yao^{17a} Y. C. Yap⁴⁸ H. Ye^{14c} H. Ye⁵⁵ J. Ye⁴⁴
 S. Ye²⁹ X. Ye^{62a} Y. Yeh⁹⁶ I. Yeletsikh³⁸ B. K. Yeo^{17a} M. R. Yexley⁹¹ P. Yin⁴¹ K. Yorita¹⁶⁷ S. Younas^{27b}
 C. J. S. Young⁵⁴ C. Young¹⁴³ Y. Yu^{62a} M. Yuan¹⁰⁶ R. Yuan^{62b,ff} L. Yue⁹⁶ M. Zaazoua^{35e} B. Zabinski⁸⁶
 E. Zaid⁵² T. Zakareishvili^{149b} N. Zakharchuk³⁴ S. Zambito⁵⁶ J. A. Zamora Saa^{137d,137b} J. Zang¹⁵³ D. Zanzi⁵⁴
 O. Zaplatilek¹³² C. Zeitnitz¹⁷⁰ H. Zeng^{14a} J. C. Zeng¹⁶¹ D. T. Zenger Jr.²⁶ O. Zenin³⁷ T. Ženiš^{28a} S. Zenz⁹⁴
 S. Zerradi^{35a} D. Zerwas⁶⁶ M. Zhai^{14a,14e} B. Zhang^{14c} D. F. Zhang¹³⁹ J. Zhang^{62b} J. Zhang⁶ K. Zhang^{14a,14e}
 L. Zhang^{14c} P. Zhang^{14a,14e} R. Zhang¹⁶⁹ S. Zhang¹⁰⁶ T. Zhang¹⁵³ X. Zhang^{62c} X. Zhang^{62b} Y. Zhang^{62c,5}
 Y. Zhang⁹⁶ Z. Zhang^{17a} Z. Zhang⁶⁶ H. Zhao¹³⁸ P. Zhao⁵¹ T. Zhao^{62b} Y. Zhao¹³⁶ Z. Zhao^{62a}
 A. Zhemchugov³⁸ K. Zheng¹⁶¹ X. Zheng^{62a} Z. Zheng¹⁴³ D. Zhong¹⁶¹ B. Zhou¹⁰⁶ H. Zhou⁷ N. Zhou^{62c}
 Y. Zhou⁷ C. G. Zhu^{62b} J. Zhu¹⁰⁶ Y. Zhu^{62c} Y. Zhu^{62a} X. Zhuang^{14a} K. Zhukov³⁷ V. Zhulanov³⁷
 N. I. Zimine³⁸ J. Zinsser^{63b} M. Ziolkowski¹⁴¹ L. Živković¹⁵ A. Zoccoli^{23b,23a} K. Zoch⁵⁶ T. G. Zorbass¹³⁹
 O. Zormpa⁴⁶ W. Zou⁴¹ and L. Zwalinski³⁶

(ATLAS Collaboration)

- ¹Department of Physics, University of Adelaide, Adelaide, Australia
- ²Department of Physics, University of Alberta, Edmonton, Alberta, Canada
- ^{3a}Department of Physics, Ankara University, Ankara, Türkiye
- ^{3b}Division of Physics, TOBB University of Economics and Technology, Ankara, Türkiye
- ⁴LAPP, University of Savoie Mont Blanc, CNRS/IN2P3, Annecy, France
- ⁵APC, Université Paris Cité, CNRS/IN2P3, Paris, France
- ⁶High Energy Physics Division, Argonne National Laboratory, Argonne, Illinois, USA
- ⁷Department of Physics, University of Arizona, Tucson, Arizona, USA
- ⁸Department of Physics, University of Texas at Arlington, Arlington, Texas, USA
- ⁹Physics Department, National and Kapodistrian University of Athens, Athens, Greece
- ¹⁰Physics Department, National Technical University of Athens, Zografou, Greece
- ¹¹Department of Physics, University of Texas at Austin, Austin, Texas, USA
- ¹²Institute of Physics, Azerbaijan Academy of Sciences, Baku, Azerbaijan
- ¹³Institut de Física d'Altes Energies (IFAE), Barcelona Institute of Science and Technology, Barcelona, Spain
- ^{14a}Institute of High Energy Physics, Chinese Academy of Sciences, Beijing, China
- ^{14b}Physics Department, Tsinghua University, Beijing, China
- ^{14c}Department of Physics, Nanjing University, Nanjing, China
- ^{14d}School of Science, Shenzhen Campus of Sun Yat-sen University, China
- ^{14e}University of Chinese Academy of Science (UCAS), Beijing, China
- ¹⁵Institute of Physics, University of Belgrade, Belgrade, Serbia
- ¹⁶Department for Physics and Technology, University of Bergen, Bergen, Norway
- ^{17a}Physics Division, Lawrence Berkeley National Laboratory, Berkeley, California, USA
- ^{17b}University of California, Berkeley, California, USA
- ¹⁸Institut für Physik, Humboldt Universität zu Berlin, Berlin, Germany
- ¹⁹Albert Einstein Center for Fundamental Physics and Laboratory for High Energy Physics, University of Bern, Bern, Switzerland
- ²⁰School of Physics and Astronomy, University of Birmingham, Birmingham, United Kingdom
- ^{21a}Department of Physics, Bogazici University, Istanbul, Türkiye
- ^{21b}Department of Physics Engineering, Gaziantep University, Gaziantep, Türkiye
- ^{21c}Department of Physics, Istanbul University, Istanbul, Türkiye
- ^{21d}Istinye University, Sariyer, Istanbul, Türkiye
- ^{22a}Facultad de Ciencias y Centro de Investigaciones, Universidad Antonio Nariño, Bogotá, Colombia
- ^{22b}Departamento de Física, Universidad Nacional de Colombia, Bogotá, Colombia
- ^{23a}Dipartimento di Fisica e Astronomia A. Righi, Università di Bologna, Bologna, Italy
- ^{23b}INFN Sezione di Bologna, Bologna, Italy
- ²⁴Physikalisches Institut, Universität Bonn, Bonn, Germany
- ²⁵Department of Physics, Boston University, Boston, Massachusetts, USA
- ²⁶Department of Physics, Brandeis University, Waltham, Massachusetts, USA
- ^{27a}Transilvania University of Brasov, Brasov, Romania
- ^{27b}Horia Hulubei National Institute of Physics and Nuclear Engineering, Bucharest, Romania
- ^{27c}Department of Physics, Alexandru Ioan Cuza University of Iasi, Iasi, Romania
- ^{27d}National Institute for Research and Development of Isotopic and Molecular Technologies, Physics Department, Cluj-Napoca, Romania
- ^{27e}University Politehnica Bucharest, Bucharest, Romania
- ^{27f}West University in Timisoara, Timisoara, Romania
- ^{27g}Faculty of Physics, University of Bucharest, Bucharest, Romania
- ^{28a}Faculty of Mathematics, Physics and Informatics, Comenius University, Bratislava, Slovak Republic
- ^{28b}Department of Subnuclear Physics, Institute of Experimental Physics of the Slovak Academy of Sciences, Kosice, Slovak Republic
- ²⁹Physics Department, Brookhaven National Laboratory, Upton, New York, USA
- ³⁰Universidad de Buenos Aires, Facultad de Ciencias Exactas y Naturales, Departamento de Física, y CONICET, Instituto de Física de Buenos Aires (IFIBA), Buenos Aires, Argentina
- ³¹California State University, Fresno, California, USA
- ³²Cavendish Laboratory, University of Cambridge, Cambridge, United Kingdom
- ^{33a}Department of Physics, University of Cape Town, Cape Town, South Africa
- ^{33b}iThemba Labs, Western Cape, South Africa
- ^{33c}Department of Mechanical Engineering Science, University of Johannesburg, Johannesburg, South Africa

- ^{33d}*National Institute of Physics, University of the Philippines Diliman (Philippines), Philippines*
- ^{33c}*University of South Africa, Department of Physics, Pretoria, South Africa*
- ^{33f}*University of Zululand, KwaDlangezwa, South Africa*
- ^{33g}*School of Physics, University of the Witwatersrand, Johannesburg, South Africa*
- ³⁴*Department of Physics, Carleton University, Ottawa, Ontario, Canada*
- ^{35a}*Faculté des Sciences Ain Chock, Réseau Universitaire de Physique des Hautes Energies—Université Hassan II, Casablanca, Morocco*
- ^{35b}*Faculté des Sciences, Université Ibn-Tofail, Kénitra, Morocco*
- ^{35c}*Faculté des Sciences Semlalia, Université Cadi Ayyad, LPHEA-Marrakech, Morocco*
- ^{35d}*LPMR, Faculté des Sciences, Université Mohamed V, Oujda, Morocco*
- ^{35e}*Faculté des sciences, Université Mohammed V, Rabat, Morocco*
- ^{35f}*Institute of Applied Physics, Mohammed VI Polytechnic University, Ben Guerir, Morocco*
- ³⁶*CERN, Geneva, Switzerland*
- ³⁷*Affiliated with an institute covered by a cooperation agreement with CERN*
- ³⁸*Affiliated with an international laboratory covered by a cooperation agreement with CERN*
- ³⁹*Enrico Fermi Institute, University of Chicago, Chicago, Illinois, USA*
- ⁴⁰*LPC, Université Clermont Auvergne, CNRS/IN2P3, Clermont-Ferrand, France*
- ⁴¹*Nevis Laboratory, Columbia University, Irvington, New York, USA*
- ⁴²*Niels Bohr Institute, University of Copenhagen, Copenhagen, Denmark*
- ^{43a}*Dipartimento di Fisica, Università della Calabria, Rende, Italy*
- ^{43b}*INFN Gruppo Collegato di Cosenza, Laboratori Nazionali di Frascati, Rende, Italy*
- ⁴⁴*Physics Department, Southern Methodist University, Dallas, Texas, USA*
- ⁴⁵*Physics Department, University of Texas at Dallas, Richardson, Texas, USA*
- ⁴⁶*National Centre for Scientific Research “Demokritos,” Agia Paraskevi, Greece*
- ^{47a}*Department of Physics, Stockholm University, Stockholm, Sweden*
- ^{47b}*Oskar Klein Centre, Stockholm, Sweden*
- ⁴⁸*Deutsches Elektronen-Synchrotron DESY, Hamburg and Zeuthen, Germany*
- ⁴⁹*Fakultät Physik, Technische Universität Dortmund, Dortmund, Germany*
- ⁵⁰*Institut für Kern- und Teilchenphysik, Technische Universität Dresden, Dresden, Germany*
- ⁵¹*Department of Physics, Duke University, Durham, North Carolina, USA*
- ⁵²*SUPA—School of Physics and Astronomy, University of Edinburgh, Edinburgh, United Kingdom*
- ⁵³*INFN e Laboratori Nazionali di Frascati, Frascati, Italy*
- ⁵⁴*Physikalisches Institut, Albert-Ludwigs-Universität Freiburg, Freiburg, Germany*
- ⁵⁵*II. Physikalisches Institut, Georg-August-Universität Göttingen, Göttingen, Germany*
- ⁵⁶*Département de Physique Nucléaire et Corpusculaire, Université de Genève, Genève, Switzerland*
- ^{57a}*Dipartimento di Fisica, Università di Genova, Genova, Italy*
- ^{57b}*INFN Sezione di Genova, Genova, Italy*
- ⁵⁸*II. Physikalisches Institut, Justus-Liebig-Universität Giessen, Giessen, Germany*
- ⁵⁹*SUPA—School of Physics and Astronomy, University of Glasgow, Glasgow, United Kingdom*
- ⁶⁰*LPSC, Université Grenoble Alpes, CNRS/IN2P3, Grenoble INP, Grenoble, France*
- ⁶¹*Laboratory for Particle Physics and Cosmology, Harvard University, Cambridge, Massachusetts, USA*
- ^{62a}*Department of Modern Physics and State Key Laboratory of Particle Detection and Electronics, University of Science and Technology of China, Hefei, China*
- ^{62b}*Institute of Frontier and Interdisciplinary Science and Key Laboratory of Particle Physics and Particle Irradiation (MOE), Shandong University, Qingdao, China*
- ^{62c}*School of Physics and Astronomy, Shanghai Jiao Tong University, Key Laboratory for Particle Astrophysics and Cosmology (MOE), SKLPPC, Shanghai, China*
- ^{62d}*Tsung-Dao Lee Institute, Shanghai, China*
- ^{63a}*Kirchhoff-Institut für Physik, Ruprecht-Karls-Universität Heidelberg, Heidelberg, Germany*
- ^{63b}*Physikalisches Institut, Ruprecht-Karls-Universität Heidelberg, Heidelberg, Germany*
- ^{64a}*Department of Physics, Chinese University of Hong Kong, Shatin, N.T., Hong Kong, China*
- ^{64b}*Department of Physics, University of Hong Kong, Hong Kong, China*
- ^{64c}*Department of Physics and Institute for Advanced Study, Hong Kong University of Science and Technology, Clear Water Bay, Kowloon, Hong Kong, China*
- ⁶⁵*Department of Physics, National Tsing Hua University, Hsinchu, Taiwan*
- ⁶⁶*IJCLab, Université Paris-Saclay, CNRS/IN2P3, 91405, Orsay, France*
- ⁶⁷*Centro Nacional de Microelectrónica (IMB-CNM-CSIC), Barcelona, Spain*
- ⁶⁸*Department of Physics, Indiana University, Bloomington, Indiana, USA*
- ^{69a}*INFN Gruppo Collegato di Udine, Sezione di Trieste, Udine, Italy*
- ^{69b}*ICTP, Trieste, Italy*

- ^{69c}*Dipartimento Politecnico di Ingegneria e Architettura, Università di Udine, Udine, Italy*
^{70a}*INFN Sezione di Lecce, Lecce, Italy*
- ^{70b}*Dipartimento di Matematica e Fisica, Università del Salento, Lecce, Italy*
^{71a}*INFN Sezione di Milano, Milano, Italy*
^{71b}*Dipartimento di Fisica, Università di Milano, Milano, Italy*
^{72a}*INFN Sezione di Napoli, Napoli, Italy*
- ^{72b}*Dipartimento di Fisica, Università di Napoli, Napoli, Italy*
^{73a}*INFN Sezione di Pavia, Pavia, Italy*
^{73b}*Dipartimento di Fisica, Università di Pavia, Pavia, Italy*
^{74a}*INFN Sezione di Pisa, Pisa, Italy*
- ^{74b}*Dipartimento di Fisica E. Fermi, Università di Pisa, Pisa, Italy*
^{75a}*INFN Sezione di Roma, Roma, Italy*
- ^{75b}*Dipartimento di Fisica, Sapienza Università di Roma, Roma, Italy*
^{76a}*INFN Sezione di Roma Tor Vergata, Roma, Italy*
- ^{76b}*Dipartimento di Fisica, Università di Roma Tor Vergata, Roma, Italy*
^{77a}*INFN Sezione di Roma Tre, Roma, Italy*
- ^{77b}*Dipartimento di Matematica e Fisica, Università Roma Tre, Roma, Italy*
^{78a}*INFN-TIFPA, Trento, Italy*
^{78b}*Università degli Studi di Trento, Trento, Italy*
- ⁷⁹*Universität Innsbruck, Department of Astro and Particle Physics, Innsbruck, Austria*
⁸⁰*University of Iowa, Iowa City, Iowa, USA*
- ⁸¹*Department of Physics and Astronomy, Iowa State University, Ames, Iowa, USA*
- ^{82a}*Departamento de Engenharia Elétrica, Universidade Federal de Juiz de Fora (UFJF), Juiz de Fora, Brazil*
- ^{82b}*Universidade Federal do Rio De Janeiro COPPE/EE/IF, Rio de Janeiro, Brazil*
^{82c}*Instituto de Física, Universidade de São Paulo, São Paulo, Brazil*
^{82d}*Rio de Janeiro State University, Rio de Janeiro, Brazil*
- ⁸³*KEK, High Energy Accelerator Research Organization, Tsukuba, Japan*
⁸⁴*Graduate School of Science, Kobe University, Kobe, Japan*
^{85a}*AGH University of Science and Technology, Faculty of Physics and Applied Computer Science, Krakow, Poland*
- ^{85b}*Marian Smoluchowski Institute of Physics, Jagiellonian University, Krakow, Poland*
⁸⁶*Institute of Nuclear Physics Polish Academy of Sciences, Krakow, Poland*
⁸⁷*Faculty of Science, Kyoto University, Kyoto, Japan*
⁸⁸*Kyoto University of Education, Kyoto, Japan*
- ⁸⁹*Research Center for Advanced Particle Physics and Department of Physics, Kyushu University, Fukuoka, Japan*
- ⁹⁰*Instituto de Física La Plata, Universidad Nacional de La Plata and CONICET, La Plata, Argentina*
⁹¹*Physics Department, Lancaster University, Lancaster, United Kingdom*
⁹²*Oliver Lodge Laboratory, University of Liverpool, Liverpool, United Kingdom*
- ⁹³*Department of Experimental Particle Physics, Jožef Stefan Institute and Department of Physics, University of Ljubljana, Ljubljana, Slovenia*
- ⁹⁴*School of Physics and Astronomy, Queen Mary University of London, London, United Kingdom*
⁹⁵*Department of Physics, Royal Holloway University of London, Egham, United Kingdom*
- ⁹⁶*Department of Physics and Astronomy, University College London, London, United Kingdom*
⁹⁷*Louisiana Tech University, Ruston, Louisiana, USA*
⁹⁸*Fysiska institutionen, Lunds universitet, Lund, Sweden*
- ⁹⁹*Departamento de Física Teórica C-15 and CIAFF, Universidad Autónoma de Madrid, Madrid, Spain*
¹⁰⁰*Institut für Physik, Universität Mainz, Mainz, Germany*
- ¹⁰¹*School of Physics and Astronomy, University of Manchester, Manchester, United Kingdom*
¹⁰²*CPPM, Aix-Marseille Université, CNRS/IN2P3, Marseille, France*
- ¹⁰³*Department of Physics, University of Massachusetts, Amherst, Massachusetts, USA*
¹⁰⁴*Department of Physics, McGill University, Montreal, Quebec, Canada*
¹⁰⁵*School of Physics, University of Melbourne, Victoria, Australia*
- ¹⁰⁶*Department of Physics, University of Michigan, Ann Arbor, Michigan, USA*
- ¹⁰⁷*Department of Physics and Astronomy, Michigan State University, East Lansing, Michigan, USA*
¹⁰⁸*Group of Particle Physics, University of Montreal, Montreal, Quebec, Canada*
- ¹⁰⁹*Fakultät für Physik, Ludwig-Maximilians-Universität München, München, Germany*
¹¹⁰*Max-Planck-Institut für Physik (Werner-Heisenberg-Institut), München, Germany*
- ¹¹¹*Graduate School of Science and Kobayashi-Maskawa Institute, Nagoya University, Nagoya, Japan*

- ¹¹²*Department of Physics and Astronomy, University of New Mexico, Albuquerque, New Mexico, USA*
- ¹¹³*Institute for Mathematics, Astrophysics and Particle Physics, Radboud University/Nikhef, Nijmegen, Netherlands*
- ¹¹⁴*Nikhef National Institute for Subatomic Physics and University of Amsterdam, Amsterdam, Netherlands*
- ¹¹⁵*Department of Physics, Northern Illinois University, DeKalb, Illinois, USA*
- ^{116a}*New York University Abu Dhabi, Abu Dhabi, United Arab Emirates*
- ^{116b}*United Arab Emirates University, Al Ain, United Arab Emirates*
- ^{116c}*University of Sharjah, Sharjah, United Arab Emirates*
- ¹¹⁷*Department of Physics, New York University, New York, New York, USA*
- ¹¹⁸*Ochanomizu University, Otsuka, Bunkyo-ku, Tokyo, Japan*
- ¹¹⁹*The Ohio State University, Columbus, Ohio, USA*
- ¹²⁰*Homer L. Dodge Department of Physics and Astronomy, University of Oklahoma, Norman, Oklahoma, USA*
- ¹²¹*Department of Physics, Oklahoma State University, Stillwater, Oklahoma, USA*
- ¹²²*Palacký University, Joint Laboratory of Optics, Olomouc, Czech Republic*
- ¹²³*Institute for Fundamental Science, University of Oregon, Eugene, Oregon, USA*
- ¹²⁴*Graduate School of Science, Osaka University, Osaka, Japan*
- ¹²⁵*Department of Physics, University of Oslo, Oslo, Norway*
- ¹²⁶*Department of Physics, Oxford University, Oxford, United Kingdom*
- ¹²⁷*LPNHE, Sorbonne Université, Université Paris Cité, CNRS/IN2P3, Paris, France*
- ¹²⁸*Department of Physics, University of Pennsylvania, Philadelphia, Pennsylvania, USA*
- ¹²⁹*Department of Physics and Astronomy, University of Pittsburgh, Pittsburgh, Pennsylvania, USA*
- ^{130a}*Laboratório de Instrumentação e Física Experimental de Partículas—LIP, Lisboa, Portugal*
- ^{130b}*Departamento de Física, Faculdade de Ciências, Universidade de Lisboa, Lisboa, Portugal*
- ^{130c}*Departamento de Física, Universidade de Coimbra, Coimbra, Portugal*
- ^{130d}*Centro de Física Nuclear da Universidade de Lisboa, Lisboa, Portugal*
- ^{130e}*Departamento de Física, Universidade do Minho, Braga, Portugal*
- ^{130f}*Departamento de Física Teórica y del Cosmos, Universidad de Granada, Granada, Spain*
- ^{130g}*Instituto Superior Técnico, Universidade de Lisboa, Lisboa, Portugal*
- ¹³¹*Institute of Physics of the Czech Academy of Sciences, Prague, Czech Republic*
- ¹³²*Czech Technical University in Prague, Prague, Czech Republic*
- ¹³³*Charles University, Faculty of Mathematics and Physics, Prague, Czech Republic*
- ¹³⁴*Particle Physics Department, Rutherford Appleton Laboratory, Didcot, United Kingdom*
- ¹³⁵*IRFU, CEA, Université Paris-Saclay, Gif-sur-Yvette, France*
- ¹³⁶*Santa Cruz Institute for Particle Physics, University of California Santa Cruz, Santa Cruz, California, USA*
- ^{137a}*Departamento de Física, Pontificia Universidad Católica de Chile, Santiago, Chile*
- ^{137b}*Millennium Institute for Subatomic physics at high energy frontier (SAPHIR), Santiago, Chile*
- ^{137c}*Instituto de Investigación Multidisciplinario en Ciencia y Tecnología, y Departamento de Física, Universidad de La Serena, La Serena, Chile*
- ^{137d}*Universidad Andres Bello, Department of Physics, Santiago, Chile*
- ^{137e}*Instituto de Alta Investigación, Universidad de Tarapacá, Arica, Chile*
- ^{137f}*Departamento de Física, Universidad Técnica Federico Santa María, Valparaíso, Chile*
- ¹³⁸*Department of Physics, University of Washington, Seattle, Washington, USA*
- ¹³⁹*Department of Physics and Astronomy, University of Sheffield, Sheffield, United Kingdom*
- ¹⁴⁰*Department of Physics, Shinshu University, Nagano, Japan*
- ¹⁴¹*Department Physik, Universität Siegen, Siegen, Germany*
- ¹⁴²*Department of Physics, Simon Fraser University, Burnaby, British Columbia, Canada*
- ¹⁴³*SLAC National Accelerator Laboratory, Stanford, California, USA*
- ¹⁴⁴*Department of Physics, Royal Institute of Technology, Stockholm, Sweden*
- ¹⁴⁵*Departments of Physics and Astronomy, Stony Brook University, Stony Brook, New York, USA*
- ¹⁴⁶*Department of Physics and Astronomy, University of Sussex, Brighton, United Kingdom*
- ¹⁴⁷*School of Physics, University of Sydney, Sydney, Australia*
- ¹⁴⁸*Institute of Physics, Academia Sinica, Taipei, Taiwan*
- ^{149a}*E. Andronikashvili Institute of Physics, Iv. Javakhishvili Tbilisi State University, Tbilisi, Georgia*
- ^{149b}*High Energy Physics Institute, Tbilisi State University, Tbilisi, Georgia*
- ^{149c}*University of Georgia, Tbilisi, Georgia*
- ¹⁵⁰*Department of Physics, Technion, Israel Institute of Technology, Haifa, Israel*
- ¹⁵¹*Raymond and Beverly Sackler School of Physics and Astronomy, Tel Aviv University, Tel Aviv, Israel*
- ¹⁵²*Department of Physics, Aristotle University of Thessaloniki, Thessaloniki, Greece*

- ¹⁵³*International Center for Elementary Particle Physics and Department of Physics, University of Tokyo, Tokyo, Japan*
- ¹⁵⁴*Department of Physics, Tokyo Institute of Technology, Tokyo, Japan*
- ¹⁵⁵*Department of Physics, University of Toronto, Toronto, Ontario, Canada*
- ^{156a}*TRIUMF, Vancouver, British Columbia, Canada*
- ^{156b}*Department of Physics and Astronomy, York University, Toronto, Ontario, Canada*
- ¹⁵⁷*Division of Physics and Tomonaga Center for the History of the Universe, Faculty of Pure and Applied Sciences, University of Tsukuba, Tsukuba, Japan*
- ¹⁵⁸*Department of Physics and Astronomy, Tufts University, Medford, Massachusetts, USA*
- ¹⁵⁹*Department of Physics and Astronomy, University of California Irvine, Irvine, California, USA*
- ¹⁶⁰*Department of Physics and Astronomy, University of Uppsala, Uppsala, Sweden*
- ¹⁶¹*Department of Physics, University of Illinois, Urbana, Illinois, USA*
- ¹⁶²*Instituto de Física Corpuscular (IFIC), Centro Mixto Universidad de Valencia—CSIC, Valencia, Spain*
- ¹⁶³*Department of Physics, University of British Columbia, Vancouver, British Columbia, Canada*
- ¹⁶⁴*Department of Physics and Astronomy, University of Victoria, Victoria, British Columbia, Canada*
- ¹⁶⁵*Fakultät für Physik und Astronomie, Julius-Maximilians-Universität Würzburg, Würzburg, Germany*
- ¹⁶⁶*Department of Physics, University of Warwick, Coventry, United Kingdom*
- ¹⁶⁷*Waseda University, Tokyo, Japan*
- ¹⁶⁸*Department of Particle Physics and Astrophysics, Weizmann Institute of Science, Rehovot, Israel*
- ¹⁶⁹*Department of Physics, University of Wisconsin, Madison, Wisconsin, USA*
- ¹⁷⁰*Fakultät für Mathematik und Naturwissenschaften, Fachgruppe Physik, Bergische Universität Wuppertal, Wuppertal, Germany*
- ¹⁷¹*Department of Physics, Yale University, New Haven, Connecticut, USA*

^aDeceased.

^bAlso at Department of Physics, King's College London, London, United Kingdom.

^cAlso at Institute of Physics, Azerbaijan Academy of Sciences, Baku, Azerbaijan.

^dAlso at Lawrence Livermore National Laboratory, Livermore, USA.

^eAlso at TRIUMF, Vancouver, British Columbia, Canada.

^fAlso at Department of Physics, University of Thessaly, Greece.

^gAlso at Department of Physics, University of Fribourg, Fribourg, Switzerland.

^hAlso at University of Colorado Boulder, Department of Physics, Colorado, USA.

ⁱAlso at Department of Physics, Westmont College, Santa Barbara, USA.

^jAlso at Departament de Física de la Universitat Autònoma de Barcelona, Barcelona, Spain.

^kAlso at Affiliated with an institute covered by a cooperation agreement with CERN.

^lAlso at The Collaborative Innovation Center of Quantum Matter (CICQM), Beijing, China.

^mAlso at Università di Napoli Parthenope, Napoli, Italy.

ⁿAlso at Institute of Particle Physics (IPP), Canada.

^oAlso at Bruno Kessler Foundation, Trento, Italy.

^pAlso at Borough of Manhattan Community College, City University of New York, New York, New York, USA.

^qAlso at Department of Financial and Management Engineering, University of the Aegean, Chios, Greece.

^rAlso at Centro Studi e Ricerche Enrico Fermi, Italy.

^sAlso at Department of Physics, California State University, East Bay, USA.

^tAlso at Institutio Catalana de Recerca i Estudis Avancats, ICREA, Barcelona, Spain.

^uAlso at Institute of Theoretical Physics, Ilia State University, Tbilisi, Georgia.

^vAlso at CERN, Geneva, Switzerland.

^wAlso at Center for Interdisciplinary Research and Innovation (CIRI-AUTH), Thessaloniki, Greece.

^xAlso at Hellenic Open University, Patras, Greece.

^yAlso at Center for High Energy Physics, Peking University, China.

^zAlso at Department of Physics, California State University, Sacramento, USA.

^{aa}Also at Département de Physique Nucléaire et Corpusculaire, Université de Genève, Genève, Switzerland.

^{bb}Also at Washington College, Chestertown, Maryland, USA.

^{cc}Also at Institut für Experimentalphysik, Universität Hamburg, Hamburg, Germany.

^{dd}Also at Institute of Applied Physics, Mohammed VI Polytechnic University, Ben Guerir, Morocco.

^{ee}Also at Institute of Physics and Technology, Ulaanbaatar, Mongolia.

^{ff}Also at Department of Physics and Astronomy, Michigan State University, East Lansing, Michigan, USA.

^{gg}Also at Physics Department, An-Najah National University, Nablus, Palestine.

^{hh}Also at L2IT, Université de Toulouse, CNRS/IN2P3, UPS, Toulouse, France.

ⁱⁱAlso at National Institute of Physics, University of the Philippines Diliman (Philippines), Philippines.

^{jj}Also at Technical University of Munich, Munich, Germany.

^{kk}Also at Yeditepe University, Physics Department, Istanbul, Türkiye.

^{ll}Also at Department of Physics, Ben Gurion University of the Negev, Beer Sheva, Israel.

^{mm}Also at Department of Physics, Stanford University, Stanford, California, USA.

ⁿⁿAlso at Institute for Nuclear Research and Nuclear Energy (INRNE) of the Bulgarian Academy of Sciences, Sofia, Bulgaria.